



**Max-Planck-Institut für Festkörperforschung
Stuttgart**

**Tuning transport, magnetic and structural
properties of $\text{La}_{0.5}\text{Ca}_{0.5}\text{MnO}_3$ films by epitaxial
strain**

Gülgün Hamide Aydoğdu Kuru

Dissertation
an der
Universität Stuttgart

Juli 2009

Tuning transport, magnetic and structural properties of $\text{La}_{0.5}\text{Ca}_{0.5}\text{MnO}_3$ films by epitaxial strain

von der Fakultät Chemie der Universität Stuttgart
zur Erlangung der Würde eines Doktors der
Naturwissenschaften (Dr. rer. nat.) genehmigte Abhandlung

vorgelegt von

Gülgün Hamide Aydoğdu Kuru

aus Ankara/Türkei

Hauptberichter:	Prof. Dr. Joachim Maier
Mitberichter:	Prof. Dr. Joachim Bill
Mitprüfer:	Prof. Dr. Helmut Bertagnolli

Tag der Einreichung:	11.05.2009
Tag der mündlichen Prüfung:	15.07.2009

MAX-PLANCK-INSTITUT FÜR FESTKÖRPERFORSCHUNG, STUTTGART
UNIVERSITÄT STUTTGART

Stuttgart 2009

Dedicated to my Yener

Contents

Abstract	7
Kurzfassung	9
1 Introduction	11
1.1 Manganites in complex oxide research	11
1.2 The role of stoichiometry and structure in LCMO	12
1.3 Electronic and magnetic interactions in LCMO.....	14
1.4 Phase separation.....	18
1.5 Strain effect.....	19
1.6 Oxygen stoichiometry effect.....	20
1.7 Motivation and outline of thesis	21
2 Film Preparation	23
2.1 PLD technique.....	23
2.2 Film formation and epitaxial film growth	25
3 Methods for Film Analysis	31
3.1 Structural and microscopic analysis	31
3.1.1 Atomic force microscopy.....	31
3.1.2 X-ray diffraction.....	31
3.1.3 High-resolution transmission electron microscopy	34
3.2 Magnetic measurement	34
3.3 Transport measurement.....	35
3.4 Angle-resolved X-ray photoelectron spectroscopy	36
3.5 Raman spectroscopy	37
3.6 X-ray magnetic circular dichroism	37

4 Results.....	39
4.1 Characterization of the LCMO target.....	39
4.2 Characterization of the LCMO thin films.....	41
4.2.1 The LCMO films on (001) STO substrate	42
4.2.2 The LCMO films on (111) STO substrate	51
4.2.3 The LCMO films on (001) SLAO substrate	64
4.2.4 The LCMO films on (001) SLGO substrate	70
4.3 The oxygen stoichiometry of LCMO films and its effect on structural and magnetic properties ..	76
5 Discussion	83
5.1 The effect of strain on the properties of LCMO films.....	83
5.1.1 The LCMO films on (001) and (111) STO substrates	83
5.1.2 The LCMO films on (001) STO and (001) SLAO substrates.....	87
5.2 The effect of oxygen stoichiometry on the properties of LCMO films	91
6 Conclusions	93
7 Summary	95
7.1 The effect of epitaxial strain.....	96
7.2 The effect of oxygen stoichiometry.....	99
8 Zusammenfassung	103
8.1 Der Einfluss der epitaktischen Verspannungen.....	104
8.2 Der Einfluss der Sauerstoffstöchiometrie.....	108
References	113
Acknowledgements.....	121
Curriculum Vitae.....	123
List of Publications Relevant to This Study.....	125

Abstract

The perovskite-type doped rare earth manganites have a rich phase diagram due to a delicate balance between several ordering mechanisms such as charge-, orbital- as well as spin order superimposed to lattice effects caused by distortions of the oxygen octahedra surrounding the Jahn-Teller ion Mn^{3+} . Chemically homogeneous materials can appear as electrically inhomogeneous in locally separated electronic phases. This phase separation in manganites is very sensitive to external perturbations such as high magnetic fields and epitaxial strain. In this study, $La_{0.5}Ca_{0.5}MnO_3$ -LCMO- (at the boundary between ferromagnetic (FM) metallic and charge-ordered antiferromagnetic (AFM) insulator) thin films are chosen as an example to investigate the competition between these different phases. LCMO films of various thicknesses are deposited on (001), (111) $SrTiO_3$, (001) $SrLaGaO_4$ and $SrLaAlO_4$ substrates by the pulsed laser deposition method. Characterization of the structural, electrical and magnetic properties of the films is performed by X-ray diffraction, atomic force microscopy, transmission electron microscopy, X-ray photoelectron spectroscopy, Raman spectroscopy, resistivity and magnetization measurements.

The present study shows that it is possible to stabilize a wide range of the electronic phases from an insulator to metallic and vary the magnetization values more than an order of magnitude using the substrate material as a knob to modify the film properties. Furthermore, it is found out that the oxygen stoichiometry, changed by heat treatments in vacuum or under O_2 flow at a constant background pressure, has a strong effect on the structural, magnetic and electronic properties of LCMO thin films. In the as deposited state, the films have a certain density of oxygen vacancies determining the physical properties in addition to cation composition and epitaxial strain.

Kurzfassung

Werden Manganate, die in der Perowskitstruktur kristallisieren, mit Erdalkalielelementen dotiert, stellt sich ein komplexes elektronisches Phasendiagramm ein. Dies beruht auf einem empfindlichen Gleichgewicht unterschiedlicher Ordnungsmechanismen wie z.B. Ladungs-, Spin- und Orbitalordnung. Ihm überlagert sind Gitterwechselwirkungen, die wesentlich von der Verzerrung der die Jahn-Teller Ionen Mn^{3+} umgebenden Sauerstoffoktaeder herrühren. Chemisch homogene Materialien erscheinen so elektronisch inhomogen, auf mesoskopischer Skala stellt sich eine Phasenseparation ein. Die Phasenseparation in Manganaten reagiert deswegen sehr empfindlich auf äußerliche Störungen wie magnetische Felder oder epitaktische Verspannungen. In dieser Arbeit sollen die Einflüsse epitaktischer Spannungen und äusserer Magnetfelder auf die physikalischen Eigenschaften beispielhaft am System $La_{0.5}Ca_{0.5}MnO_3$ (LCMO) untersucht werden. Die Dotierung wurde so gewählt, dass sie an der Grenze zwischen einem ferromagnetischen Metall und einem durch Ladungsordnung generierten antiferromagnetischen Isolator liegt. Strukturell phasenreine dünne Schichten aus LCMO unterschiedlicher Schichtdicken wurden mittels gepulster Laserablation (PLD) auf verschiedenen Substraten ($SrTiO_3$ mit (001)- und (111)-Orientierung sowie auf $SrLaGaO_4$ und $SrLaAlO_4$ mit (001)-Orientierung) abgeschieden. Die strukturellen, elektrischen und magnetischen Eigenschaften dieser dünnen Schichten wurde mittels Röntgendiffraktometrie, Rasterkraft-(AFM) und Transmissionselektronenmikroskopie (TEM), Photoelektronenspektroskopie (XPS), Raman-Spektroskopie, Widerstandsmessungen und Magnetisierungsmessungen bestimmt.

Die Untersuchungen zeigen, dass es möglich ist, eine große Bandbreite von elektrischen Phasen, vom Isolator bis hin zum Metall, zu stabilisieren und dabei die Magnetisierung mehr als eine Größenordnung zu ändern, in dem man das Substrat als Stellschraube für die Modifikation der Schichteigenschaften nutzt. Darüber hinaus wurde festgestellt, dass die Sauerstoffstöchiometrie, geändert durch Wärmebehandlung im Vakuum oder im O_2 -Strom bei einem konstanten Partialdruck, einen starken Effekt auf die strukturellen, magnetischen und elektronischen Eigenschaften von dünnen LCMO-Schichten bewirkt. Ferner zeigte es sich, dass selbst unbehandelte epitaktisch gewachsenen Schichten eine gewisse Konzentration von Sauerstoffleerstellen besitzen, die neben der Zusammensetzung der Kationen und der epitaktischen Spannung, die physikalischen Eigenschaften wesentlich bestimmen.

Chapter 1

Introduction

1.1 Manganites in complex oxide research

The research in the field of complex oxides has been determined by the wealth of interesting properties suitable for applications including magnetic order, high temperature superconductivity (HTS), colossal magnetoresistance (CMR), metal to insulator transitions (T_{MI}), high electronic and/or ionic conductivity. They make them candidates for several application areas i.e. microelectronics, spintronics, nanotechnology and energy conversion and storage (e.g. fuel cells, batteries and thermoelectrics) [1, 2].

In the recent years, the manganese oxides with the general formula $RE_{(1-x)}A_xMnO_3$ (where RE is a rare earth element e.g. Pr, La, Y; A is a divalent alkaline earth element e.g. Ba, Ca, Sr), in the form of bulk or thin film, have especially been highlighted because of three main driving forces: (i) Manganites are a subgroup of strongly-correlated electron systems, for which interaction between electrons is pronounced and responsible for many peculiar properties of them. Therefore, understanding the new physics introduced by manganites is of cardinal importance as a fundamental research problem. It is clear that information obtained from manganites can be transferred to other subgroups of strongly-correlated electron systems by analogy and in turn will shed more light on hot topics like HTS. (ii) They also exhibit the CMR phenomenon [3-5] which is a large change in the electrical conductivity of the specimen caused by the application of a magnetic field. It should be noted that due to this property, they are regarded as promising candidates for switch and sensor applications [6]. One of these applications is tunnel magnetoresistance (TMR) sensors which consist of two layers of ferromagnetic materials separated by a thin tunnel barrier [7-9]. This is made of a multiferroic thin film. The multiferroic is defined as the combination of ferroelectric and magnetic order. With these materials, the magnetic state can be manipulated by electric field or vice versa. In such a device, the transport of spins through the barrier can be electrically tuned and magnetoresistance of the device can be controlled by the applied electric field. (iii) The electrical properties of some manganites (i.e. having high electronic and ionic conductivity) satisfy the requirements as a cathode material for solid oxide fuel cells (SOFC), based on the conversion of chemical energy to electrical energy with reasonable efficiency [10-11]. This technology is considered to be one of the most promising options for new and

environmentally friendly electrical energy sources; however the development and application of improved electrode materials involve to provide achievable electrochemical process at lower operating temperature (below 900°C). For this purpose, lanthanum strontium manganite oxide (LSMO) as a cathode electrode for oxide-ion SOFC has been the most systematically investigated and progressed by means of varying geometrical parameters and modifying dopant ion and/or concentration in the material [12-14].

1.2 The role of stoichiometry and structure in LCMO

ABO_3 compounds (e.g. $LaMnO_3$ -LMO-, an antiferromagnetic insulator), where A and B are large and small cations, respectively, are the parent compounds for the rare earth manganites. They have a nearly cubic perovskite-like crystal structure, shown in Fig.1.1. This structure can be regarded as a three-dimensional network of corner sharing MnO_6 octahedra, where the Mn ions are at the center. Each eight octahedra form a cube (see Fig. 1.1) with the A site, e.g. La^{3+} and Ca^{2+} , at its centre [15-16].

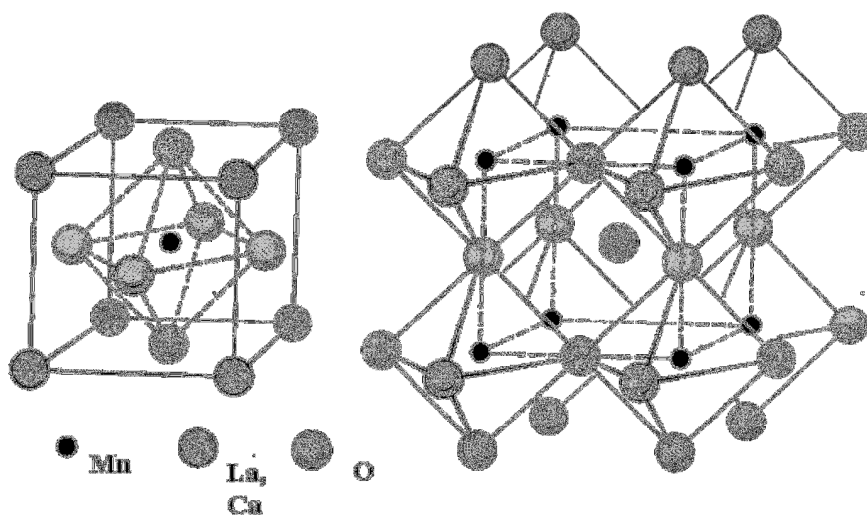


Fig. 1.1: The crystal structure of $LaMnO_3$ as a representative of perovskite family.

The properties of the perovskites are mainly determined by the band structure and filling, but also depend on the cation ordering, presence of vacancies and dopants. In the pure LMO compound, the partial substitution of the La^{3+} site by Ca^{2+} rising the possibility of phase changes with temperature (stated in the following section) produces charge compensation by

increasing the hole densities [17-23] which are responsible of higher electrical conductivity of manganese oxides.

Nonstoichiometry and lattice defects in lanthanum manganite influence the multivalent nature of Mn. Charge equilibrium is maintained by the oxidation of a corresponding fraction of Mn^{3+} ions to oxidation state Mn^{4+} [21]. The oxidation state of Mn also depends on the oxygen stoichiometry in $\text{LaMnO}_{3\pm\delta}$ and can be enhanced by the presence of transition metal vacancies or reduced by oxygen vacancies in the lattice.

Moreover, the cation-doping is strongly related with the ionic radii mismatch, which also influences the electronic structure of the material via the tolerance factor. The Goldschmidt tolerance factor, t , defined in Eq. (1), was proposed to describe the distortion and stability of any ABO_3 perovskite lattice [24]. The terms $r(\text{A})$, $r(\text{B})$ and $r(\text{O})$ stand for the ionic radii of A, B cations and O anion, respectively.

$$t = \frac{r(\text{A}) + r(\text{O})}{\sqrt{2}[r(\text{B}) + r(\text{O})]} \quad (1)$$

The structure is predicted to be cubic if t equals to 1. On the other hand, the distorted perovskite-like lattices exist approximately in the ranges of $0.89 < t < 1$ and $1 < t < 1.02$. For most of the manganites t is smaller than 1, i. e. the A cations are too small for a cubic lattice. As a result, a buckling of octahedra occurs, leading to orthorhombic crystal symmetry, as shown in Fig 1.2. Apart from structural reasons, some distortion can also have an electronic origin such as in the case of Jahn-Teller effect of Mn^{3+} cations, which will be discussed in the subsequent section of this chapter.

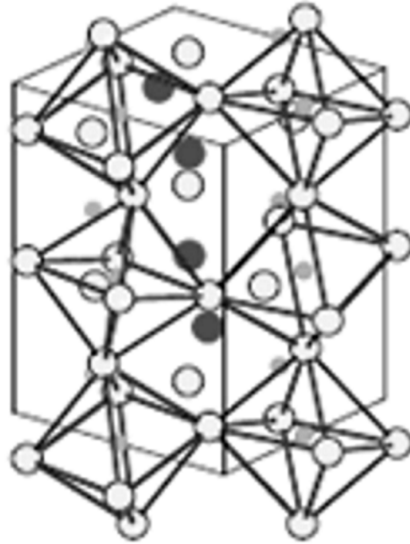


Fig. 1.2: The orthorhombic structure caused by distortion of the perovskite lattice.

1.3 Electronic and magnetic interactions in LCMO

Electrical and magnetic properties of manganites result from a competition between several mechanisms such as a charge, orbital and spin ordering [25-27] superimposed by lattice effects. The phase diagram of the $\text{La}_{(1-x)}\text{Ca}_x\text{MnO}_3$ system [28] shown in Fig. 1.3 as an example, can be considered as a consequence of this competition. In Fig. 1.3, it is seen that several different electronic phases (e.g. paramagnetic -PM-, antiferromagnetic-charge-ordered -AF-CO- and ferromagnetic -FM- phases) can exist according to the temperature and Ca^{2+} doping level of the specimen. At the boundaries of the phase diagram some of these electronic phases coexist (e.g. at 50 % Ca, there is region of high complexity due to the coexistence of three fundamental phases FM, AF-CO and PM). The equilibrium between these phases can be disturbed quite easily in favor of a certain phase by external perturbations such as magnetic field, electrical field, photon flux and strain. It should be here noted that even the structure of AF-CO phase is not simple and can be subdivided into various types as A, C and G (cf. Fig. 1.4) [29].

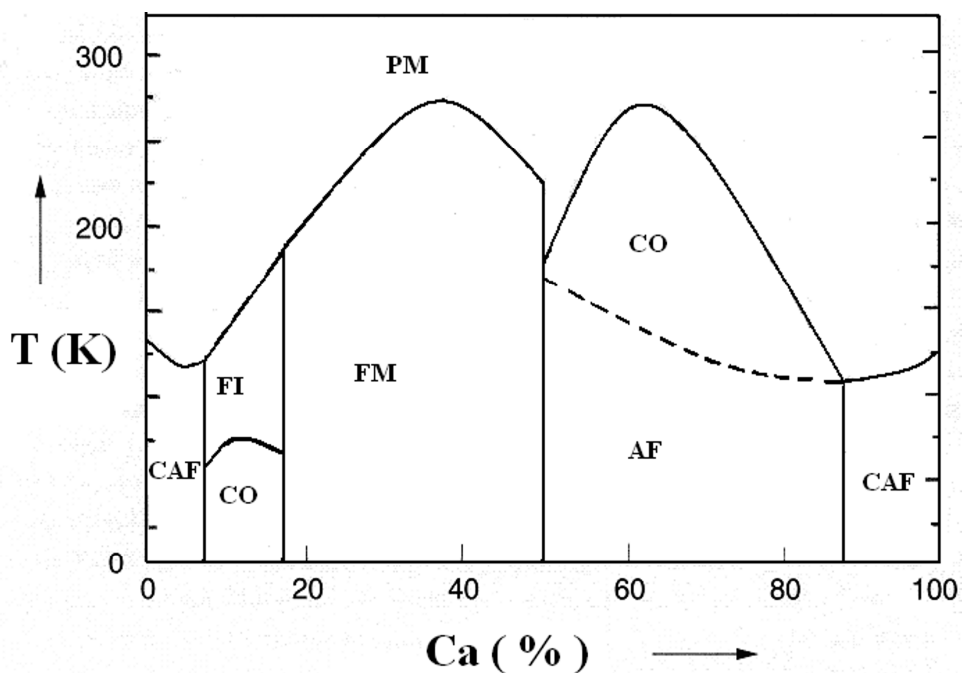


Fig. 1.3: Phase diagram of $\text{La}_{(1-x)}\text{Ca}_x\text{MnO}_3$.

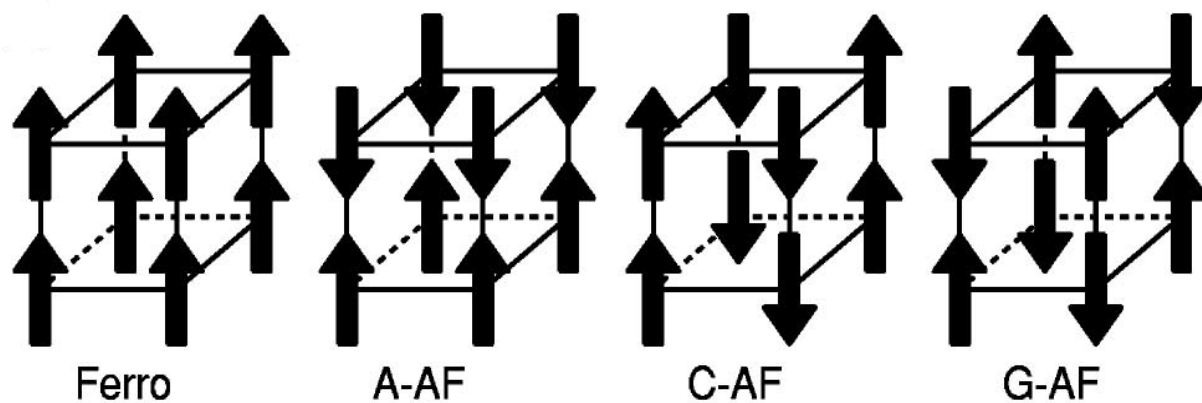


Fig. 1.4: Different types of spin ordering; ferromagnetic and antiferromagnetic (e.g. A, C and G-types) [29].

Despite the ideas proposed to explain the observations such as CMR, inhomogeneous character and strong correlation between ferromagnetic metallic phase and metal-insulator transition [30, 31], most of these points could not be clarified entirely. There are still many

open questions in addition to many clues obtained from both experiments and theoretical investigations. Some of the basic ideas mentioned above are double exchange, electron phonon interaction due to Jahn-Teller distortion, mesoscopic phase separation and percolation phenomena.

The double-exchange model, proposed first by Zener [32], is crucial to explain the electron transfer in the ferromagnetic-metallic phase, demonstrated by a simple sketch in Fig. 1.5. Whereas an e_g electron of Mn^{3+} is transferred to the O $2p$ orbital, an electron goes from O $2p$ orbital to Mn^{4+} simultaneously. Due to strong Hund coupling the probability of electron transfer is larger when spins of neighboring Mn^{3+} and Mn^{4+} ions are parallel. Consequently, strong ferromagnetic interaction is ensured. In a semiclassical treatment, the double exchange mechanism leads to a dependence of the electron transfer between Mn ions on the angle θ between their spins. Then, the effective hopping probability is proportional to $\cos(\theta/2)$, which varies from 0 to 1 as the relative orientation of the spins of neighbouring Mn ions varies from antiparallel to parallel [33]. Double exchange generally competes with the superexchange mechanism [33-35] representing the electron transfer between two Mn^{4+} ions, which favors antiferromagnetism.

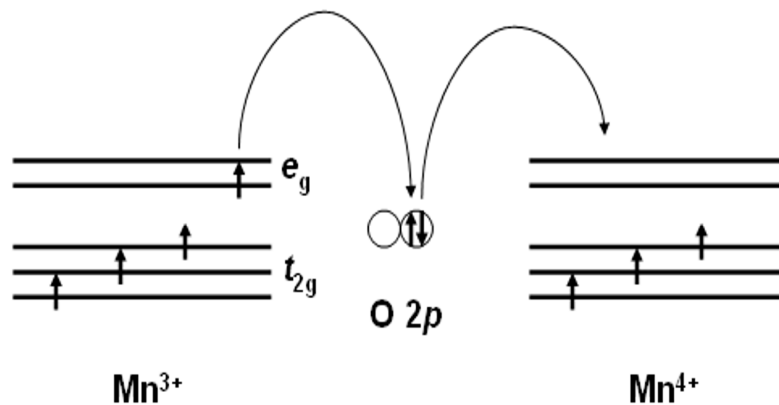


Fig. 1.5: Double-exchange mechanism.

Charge ordering is the periodic distribution of the Mn^{3+} and Mn^{4+} ions in the lattice. This rearrangement is thought to stem from strong Coulomb interaction. In addition to charge

ordering, there are two more degrees of freedom namely orbital and spin ordering [34]. These three mechanisms are shown in Fig. 1.6 in a simple sketch. For instance it is seen that a sublattice can be constructed from the ordered arrangement of d_{z^2} orbital of Mn^{3+} ions. Charge ordering leads to localization of the mobile electrons in certain positions in the lattice and reduction of the electrical conductivity whereas orbital and spin ordering give rise to anisotropic electron transfer.

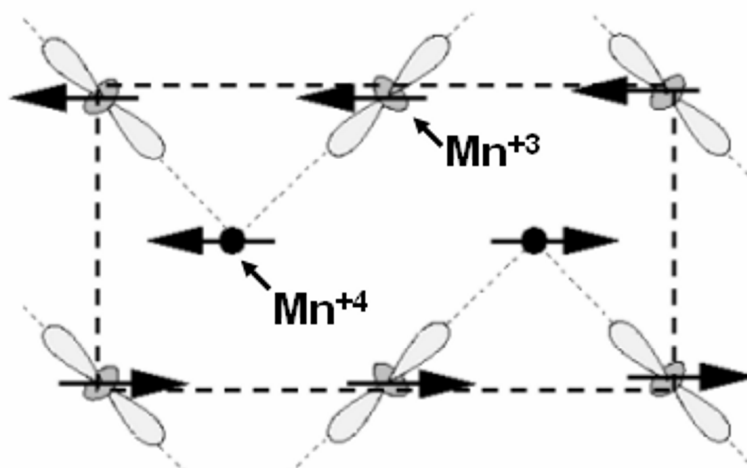


Fig. 1.6: Charge, spin and orbital ordering in manganites (reproduced from reference [36]).

The Jahn-Teller effect [37] is the distortion of a non-linear molecule with a degenerate electronic state to remove the degeneracy and to reduce the overall energy. In an octahedral environment, as in the case of Mn^{3+} and Mn^{4+} ions in manganites, two e_g orbitals have larger energy than the remaining t_{2g} orbitals (see Fig. 1.7). A large distortion is caused by the Mn^{3+} ion since the number of electrons in the e_g orbital is odd. However, no Jahn-Teller effect is expected for Mn^{4+} ion, which has only three electrons in the t_{2g} orbitals. Pronounced Jahn-Teller distortions are generally associated with the insulating behaviour because charge carriers are trapped and electron-lattice polarons are formed in the vicinity of these local distortions. It has also been demonstrated employing several manganite systems that Jahn-Teller distortion gradually decreases as the temperature is decreased. It has the lowest value at the insulator to metal transition and stays practically constant if temperature is reduced further [38].

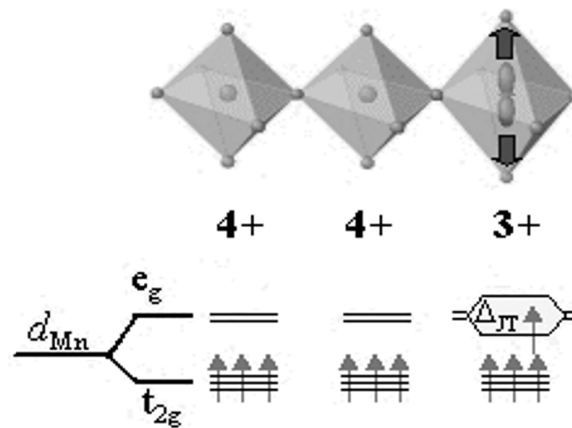


Fig. 1.7: Jahn-Teller distortion in manganites.

1.4 Phase separation

Another interesting finding related to manganites is the co-existence of different electronic phases in a nominally chemically homogeneous system. The transport properties of the specimen are determined by the evolution of percolation path. An insulator to metal transition can be monitored if metallic regions are connected to each other and constitute a continuous network.

Several experimental studies have pointed out the above mentioned co-existence. For instance, Uehara et al. identified both the AF-CO and FM phases in $\text{La}_{5/8-y}\text{Pr}_y\text{Ca}_{3/8}\text{MnO}_3$ employing transport and magnetic measurements as well as electron microscopy techniques [39]. In addition, Renner et al. studied the phase separation in $\text{Bi}_{1-x}\text{Ca}_x\text{MnO}_3$ single crystals by atomic resolution scanning tunneling microscopy and monitored two distinct regions: There was a surface region that had a band gap because of charge ordering (I-V curve of this region displayed insulating behaviour), whereas other regions were metallic [40]. Recently, Loudon et al. used Fresnel imaging and electron holography to monitor the ferromagnetic domains and electron diffraction and dark-field imaging to identify the charge-ordered regions in polycrystalline $\text{La}_{0.5}\text{Ca}_{0.5}\text{MnO}_3$ [41]. In Fig. 1.8, some images from this study are presented. It is clear that both a ferromagnetic and a nonferromagnetic phase are present in the specimen. In addition, it is interesting that some regions are both ferromagnetic and charge ordered although the charge-ordered phase is generally associated with antiferromagnetic character.

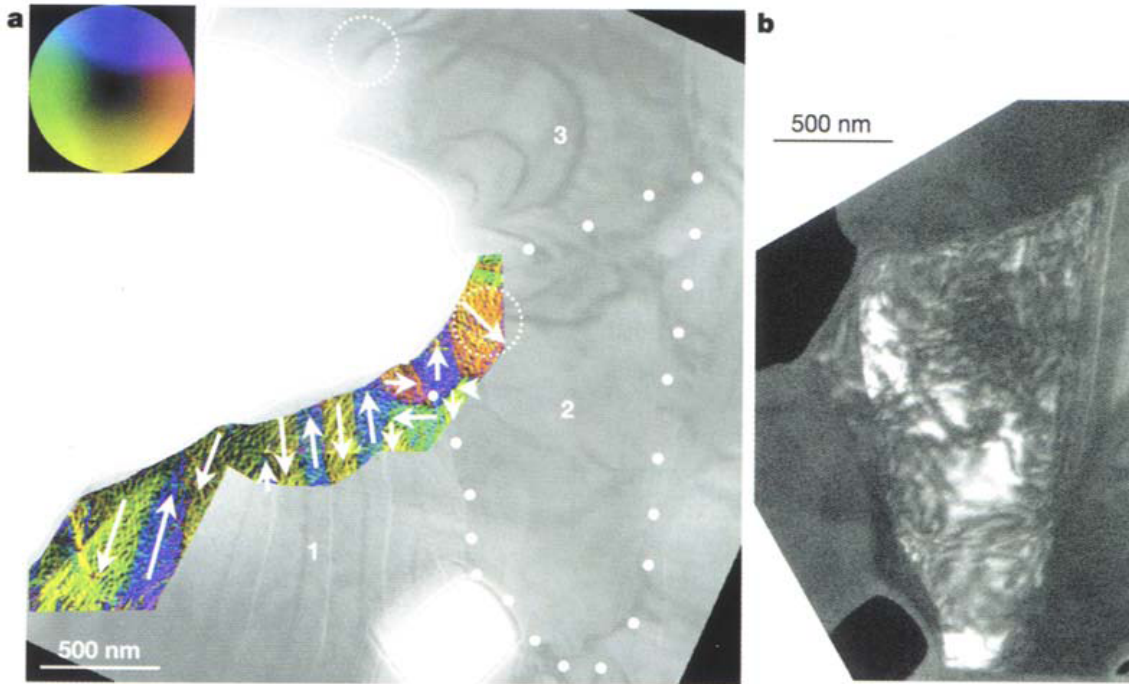


Fig. 1.8: Co-existence of ferromagnetic and charge-ordered phases. Three grains (labeled as 1, 2 and 3) are shown and the white dots are used to show the grain boundary between the grains.

It is possible to trigger the electronic phase separation, change the dominant phase and tune the electronic and magnetic properties via some external perturbations such as hydrostatic pressure [42-45], photon (e.g. X-ray [46, 47], laser [48] and visible light [49]) irradiation, electrical [50] and magnetic fields [51-53] and epitaxial strain imposed by the substrate [54-56]. The strain parameter is discussed in more detail in the following section since this effect is thoroughly studied in the present work using various substrates.

1.5 Strain effect

One of the main factors distinguishing manganite thin films from bulk ceramic specimens is their residual strain, which can be caused by epitaxial relationship between the film and the substrate, its deposition conditions and some possible temperature variations (if in-plane coefficients of thermal expansion are different for the film and the substrate). It is obvious that the above mentioned strain modifies the Mn-O-Mn bond angle and the Mn-O distances. These variations can have drastic influences on the resulting electrical and magnetic properties due

to the fact that Mn d orbitals and O p orbitals, determining most of these electrical and magnetic properties of the film, are strongly coupled to the lattice degree of freedom. Consequently, it is possible to use strain parameter to deliberately tailor the properties of manganite thin films.

Three basic routes can be followed to vary the residual strain in thin films: (i) Deposition conditions (e.g. energy of the atoms separated from the target, temperature of the deposition and pressure inside the chamber) can be altered. However, some other parameters such as grain size and defect concentration are also modified by this approach, making a systematic investigation tedious. (ii) Films can be grown on various substrates having different lattice constants and, in turn, applying epitaxial strains of different extent [57-61]. (iii) The strain in the film can be altered by depositing layers with different thicknesses (e.g. see Refs. [62-68]). The thinner films are more strained than the thicker ones since a certain amount of epitaxial strain is relaxed by defects like misfit dislocations in the latter. In the present study, the strategies (ii) and (iii) are applied to the case of $\text{La}_{0.5}\text{Ca}_{0.5}\text{MnO}_3$ thin films.

It should be here noted that, apart from the residual strain, there are also additional factors that can influence the bond lengths and angles in the film lattice as externally applied strain (e.g. hydrostatic strain and strain imposed by a piezoelectric substrate) and several types of defects (e.g. dislocations, vacancies and self-interstitials; for the effect of O vacancies see the following section).

1.6 Oxygen stoichiometry effect

Oxygen stoichiometry, which can be varied by heat treatments in vacuum and different O_2 environments, has been shown to have a crucial role in determining the structural and electronic states of several oxide thin films [69-82].

The response of the oxide to the heat treatments mentioned above can be considerably different. For instance, the resistance of $\text{Sr}_2\text{FeMoO}_6$ films deposited on (100) SrTiO_3 (STO) substrate increases during O_2 annealing, explained by the formation of high resistance regions in grain boundaries, whereas $\text{La}_{0.67}\text{Ca}_{0.33}\text{MnO}_3$, in the ferromagnetic (FM) phase, deposited on (100) NdGaO_3 (NGO), becomes more metallic, conceivable recognizing the inverse relation between the hole concentration and the oxygen vacancies. Out of plane lattice parameter and resistivity of $\text{La}_{0.67}\text{Ca}_{0.33}\text{MnO}_3$ films increase with vacuum annealing [69]. Additionally, it is observed also by Prellier [82] that for oxygen annealing leads to an enhancement of T_{MI} and T_{C} .

It should be noted here that a great majority of the data reported for $\text{La}_{(1-x)}\text{Ca}_x\text{MnO}_3$ system are for the composition around $x=0.3$ [69-71]. Consequently, the response of different compositions of this family to heat treatments in both vacuum and O_2 atmosphere is of particular interest to understand whether some additional mechanisms are at work for the compositions having other electronic phases (e.g. the CO-AFM phase) or not. Furthermore, data concerning the relative extent of oxygen stoichiometry and epitaxial strain effects are lacking in literature. In this study, presented results (see Chapter 4) regarding the effect of vacuum and O_2 annealing on structural and magnetic properties of $\text{La}_{0.5}\text{Ca}_{0.5}\text{MnO}_3$ (at the boundary between CO-AFM and FM phases according to the bulk phase diagram) thin films are expected to shed more light on the topic.

1.7 Motivation and outline of thesis

The need to understand fundamental aspects of manganite oxides has carried the development of model systems (i.e. thin films). Pulsed Laser Deposition technique (PLD) has the potential to be a very useful tool for this research while systematically investigating the special features of manganite oxides which are highly sensitive to the strain and oxygen stoichiometry effect.

The aim of this work is to show the possibility of tuning the dominant electronic phase between an antiferromagnetic insulator and a ferromagnetic metal via the epitaxial strain imposed by the substrate acting as a functional element and demonstrating the significance of oxygen stoichiometry, varied by vacuum or O_2 annealings, in terms of the eventual electronic and magnetic state.

The structure of the thesis is as follows: Chapter 2 and Chapter 3 describe the experimental method to prepare the high quality $\text{La}_{0.5}\text{Ca}_{0.5}\text{MnO}_3$ films (i.e. the pulsed laser deposition technique), and details of the characterization tool employed (e.g. X-ray diffraction and atomic force microscopy for structural, four-point probe for electrical and magnetization measurement for magnetic properties), respectively. Chapter 4 and Chapter 5 consist of the results of the experimental work, related to the influences of epitaxial strain as well as oxygen stoichiometry, and their interpretation, respectively. The study is concluded in the Chapter 6. In the Chapters 7 and 8, the work is summarized and the remaining questions, which can be regarded as possible topics of a future study, are stated in English and German languages, respectively.

Chapter 2

Film Preparation

2.1 PLD technique

Pulsed laser deposition (PLD) is one of the most convenient and unique methods to produce epitaxial multi-component oxide thin films with very low defect density. The historical development of PLD technique starts in 1963 when Ready and White used a ruby laser to vaporize a solid surface [83, 84]; thereafter, Smith and Turner [85] suggested using this effect as a thin film deposition technique. In 1987, Dijkkamp and Venkatesan [86] fabricated $\text{YBa}_2\text{Cu}_3\text{O}_7$, a high critical temperature superconductor, thin films employing PLD. With the increase of the number of research groups and the development of new laser technology, PLD became an indispensable tool for the growth of thin films with complex stoichiometry in 1990's.

In the PLD process, the dynamic plasma created by the pulsed laser (heating rate of the target surface is of the order of 100 K/s) condensates on the heated substrate under oxygen atmosphere [87-89]. Although the working principle seems straightforward, its application and control are rather complex due to the large number of variables affecting the film properties. The distance between target and substrate, oxygen pressure, wavelength of the excimer laser, laser fluence, pulse frequency, substrate temperature and annealing time are some of the important parameters optimized to produce high-quality thin films. In addition to the ability of producing a film with the same composition as the target, PLD technique provides the flexibility of using various deposition atmospheres (e.g. inert and/or reactive gases and at different gas pressures). Moreover, it is cost effective (since many vacuum systems can easily be combined with a laser), fast (e.g. deposition rates are typically ~ 100 Å/min.), clean and the thickness can be controlled in real time by the number of pulses. However, as a disadvantage, only samples having a limited surface area can be prepared by this method since the cross section of the ablation plume is normally a few cm^2 due to small laser spot size and the highly focused directed laser plume. Additionally, the in-situ monitoring of growth by characterization techniques such as atomic force microscopy, scanning tunneling microscopy, scanning electron microscopy and transmission electron microscopy is difficult due to high operation pressure. Fortunately, reflection high-energy

electron diffraction (RHEED) makes in-situ observation of growth of surfaces and interfaces on the atomic scale feasible [90].

The main components and working principle of the PLD system used in the present study are described in Fig. 2.1. The laser beam enters to the vacuum chamber and is focused on the rotating target, a pellet with a diameter of 15 mm. The angle between the laser beam and the target surface is adjusted to 45° . The surface of the target material vaporizes and the atoms separated from the target are condensed on the surface of the substrate (the distance between the target and the substrate is 4 cm), with the required structure and composition. For the deposition of LCMO films an excimer laser with KrF gas mixture emitting ultra-violet radiation having a wavelength of 248 nm was employed in the PLD system. Laser fluence and pulse frequency were fixed to 1.6 J/cm^2 and 5 Hz, respectively. The films were deposited on single crystal substrates, cleaned in ultrasonic baths of acetone and ethanol, at 1073 K (substrates mounted on a sapphire holder were heated radiatively) and with an oxygen pressure of 0.4 mbar in order to assist the formation of the desired phase and composition. After deposition, films were annealed at 1173 K for 30 min. in ambient oxygen pressure. During the deposition, temperature was controlled with a few K precision. The nominal thicknesses of the films were adjusted by counting the pulses after several calibration runs to determine the growth rate. The error in film thickness was around 10 % mainly arising from intensity fluctuations of the laser beam.

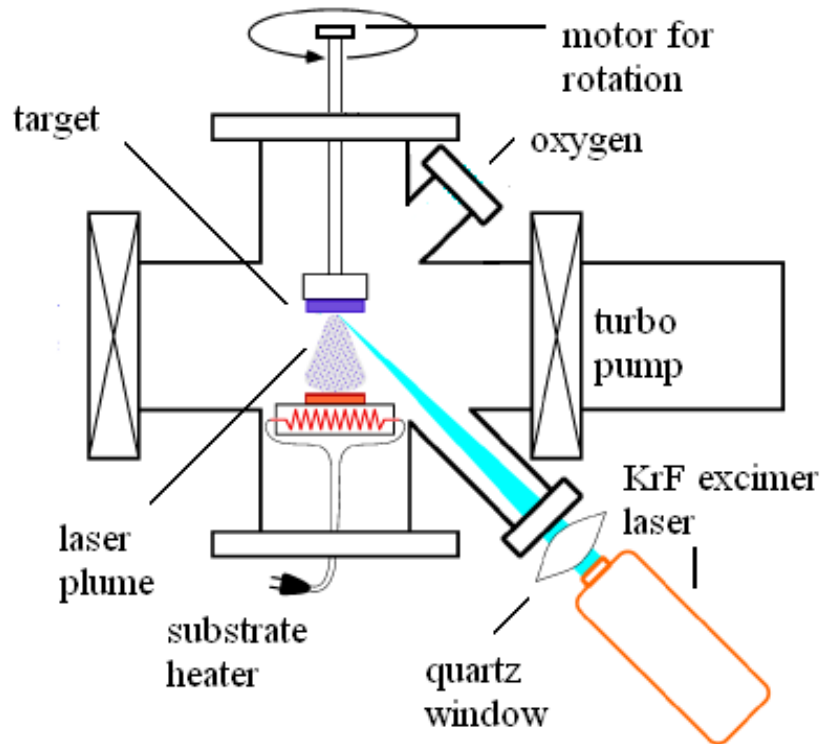


Fig. 2.1: The basic components of the PLD system.

2.2 Film formation and epitaxial film growth

In the PLD technique, the eventual thin film morphology is determined by the thermodynamics and kinetics as a result of the superposition of many individual processes such as adsorption, desorption, diffusion, nucleation and coarsening (see Fig. 2.2). The energy of the impinging atoms, their surface mobility, deposition rate and atomic structure of the substrate surface (e.g. the terraces on the substrate surface may act as additional nucleation sites) are some of the fundamental parameters controlling the above mentioned mechanisms.

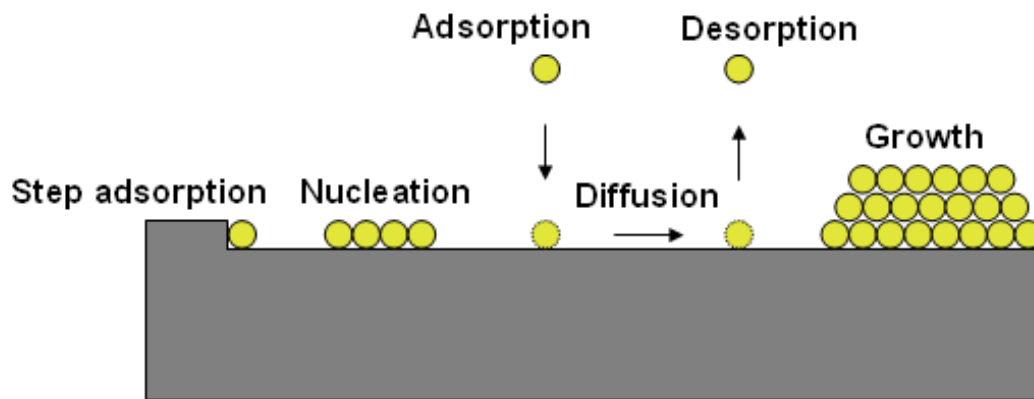


Fig. 2.2: Schematic representation of atomic processes.

Deposition starts with the condensation of a sufficient number of vapor atoms and creation of a stable residence on the substrate. The following stage is the observation of small clusters or islands, distributed more or less homogeneously on the surface of the substrate. Thereafter, the islands grow in size and merge together which is called the coalescence step. Coalescence continues until a connected network with vacant channels is developed. Lastly, the continuous film is formed after the porous channels and, even, the isolated voids are filled in completely [91].

As shown in Fig. 2.3, there are three main modes [92, 93] for growth of thin films on planar substrates: (i) The Volmer-Weber (or island growth) mode, where clusters grow to form islands because of the stronger binding between the depositing atoms than the interaction between the depositing and the substrate atoms. (ii) The Frank-van der Merwe (or layer-by-layer growth) mode has the opposite characteristics of island growth mode (i.e. the strength of the binding between the adatoms and the substrate atoms is stronger). (iii) The Stranski-Krastanov (SK) growth mode where islands become favorable after forming layers of a certain thickness. Although, the reason behind the change from layer growth to three-dimensional growth is not completely clear, it is thought that transition to island growth mode may be favorable as a relaxation mechanism for the strain energy created by film-substrate lattice mismatch. It should be here noted that in addition to these main three growth modes, a

fourth one is proposed, called the step-flow growth, where the film pursues step-terrace structures on the substrate. In addition to the atomic steps on the substrate other conditions such as high temperature and high deposition rate should also be satisfied to suppress the island growth and make the step-flow mode active. However, this growth mode usually transforms to the three-dimensional growth mode for the thicker films.

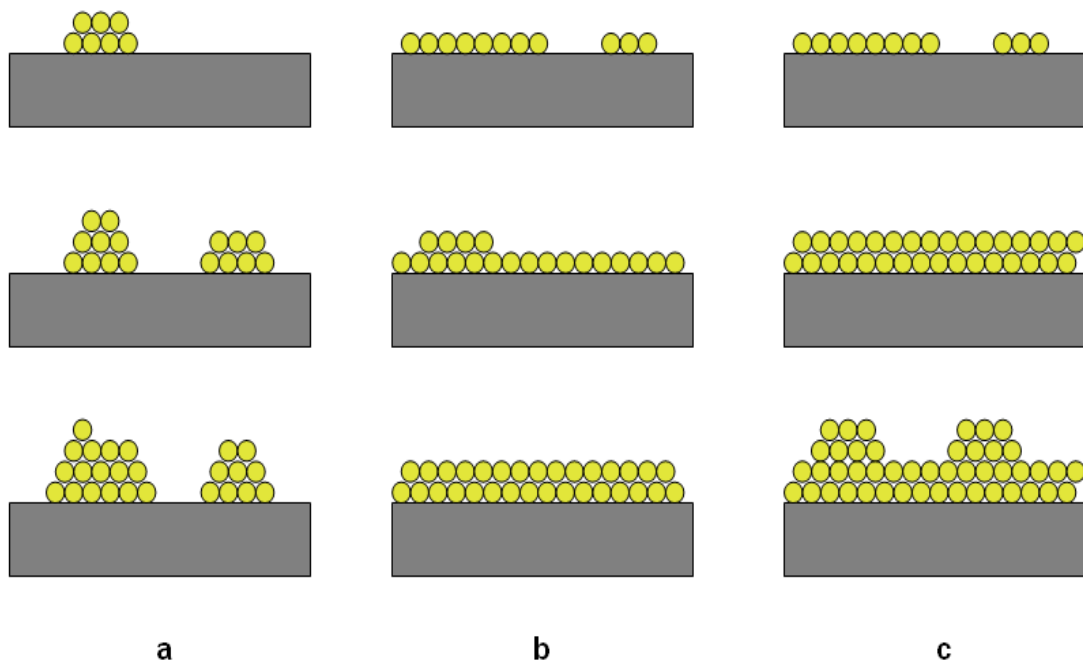


Fig. 2.3: Schematic representation of the three crystal growth modes: (a) island or Volmer-Weber, (b) layer or Frank-van der Merwe, (c) layer plus island or Stranski-Krastanov.

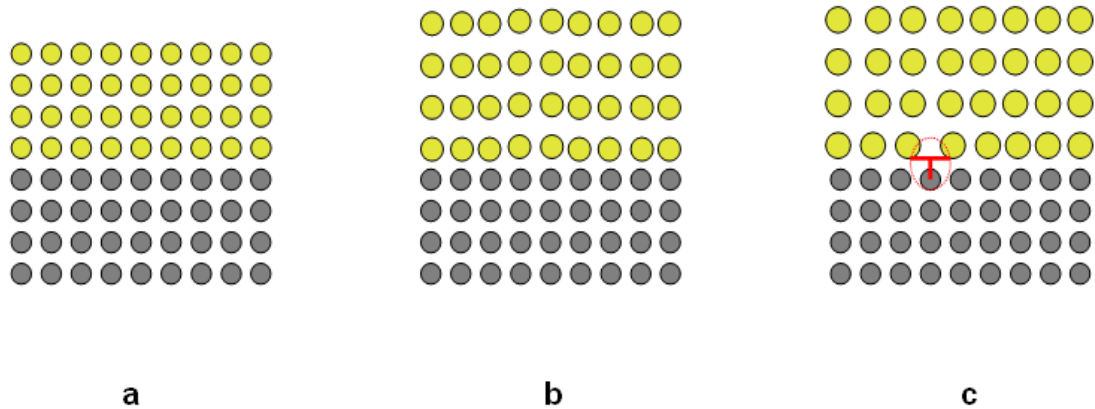


Fig. 2.4: Schematic illustration of (a) lattice-matched, (b) strained and (c) partially-relaxed epitaxial layers (the misfit dislocation in the partially-relaxed case is shown by a red circle).

If the orientation of the film is strictly defined by a certain relationship with the orientation of a single-crystal substrate, the film is called epitaxial. In this case, the crystal structure of the substrate provides a template for the formation of the film lattice (or in other words the structure of the film imitates the structure of the substrate material) and certain planes and directions in the film correspond to some certain planes and directions in the substrate lattice. There are two main classes of epitaxial thin films namely homoepitaxial and heteroepitaxial films, referring to the cases where the film and the substrate are the same material or composed of different materials, respectively.

The substrate should satisfy some conditions to be suitable for epitaxial growth. (i) It should be single crystalline and stable, chemically and mechanically. (ii) The in-plane lattice mismatch between the film and the substrate should be small. (iii) Coefficients of thermal expansion of the layer and the substrate should be similar in the range between the deposition and the ambient temperatures. (iv) It should have no phase transition increasing the mismatch between the lattice parameters or coefficients of thermal expansion [94]. The four single-crystalline substrates employed in this study are (001) SrTiO₃ (STO), (111) STO, (001) SrLaGaO₄ (SLGO) and SrLaAlO₄ (SLAO). The lattice parameters of these substrates and their corresponding lattice mismatch values (it is noted that the mismatch values are

calculated using the relation, $\zeta = (a_s - a_b)/a_b$, where a_b and a_s refer to lattice parameter of bulk and lattice parameter of substrate, respectively) for two in-plane directions (i.e. ζ_1 and ζ_2) are summarized in Table 2.1. It is seen from the table that STO and SLGO substrates impose tensile epitaxial strain while the in-plane lattice parameter of SLAO is smaller than the in-plane lattice parameter of LCMO leading to a compressive epitaxial strain.

Table 2.1: The list of the substrates employed in the present study. The match strain values imposed by them are also presented.

Substrate	Crystal Structure	Lattice Parameter (nm)	ζ_1 (%)	ζ_2 (%)
(001)STO	Cubic	$a=0.3905$ [95]	1.92	1.86
(111)STO	Cubic	$a=0.3905$	1.92	2.12
(001)SLAO	Tetragonal	$a=0.3756$ $c=1.2636$ [96]	-1.79	-1.80
(001)SLGO	Tetragonal	$a=0.3844$ $c=1.2688$ [97]	0.490	0.475

Chapter 3

Methods for Film Analysis

3.1 Structural and microscopic analysis

3.1.1 Atomic force microscopy

The surface morphology was examined by atomic force microscopy (AFM) by a Digital Instruments Nanoscope II in tapping mode. This technique is widely used in order to observe the surface topology and to obtain the surface roughness, illustrated in Fig. 3.1. An extremely sharp tip, mounted on the end of silicon or a silicon nitride cantilever, is oscillated up and down (with a frequency close to its resonance frequency) by the force related to the distance between the sample and the tip during scanning a selected part of the specimen surface [98]. The vertical resolution is less than 0.1 nm whereas the lateral resolution is approximately 10 nm.

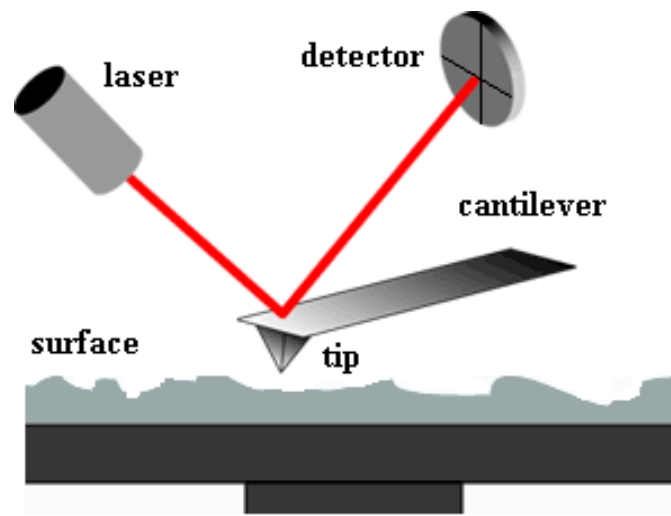


Fig. 3.1: An illustration of the basic components of AFM.

3.1.2 X-ray diffraction

The determination of the epitaxial relationship between the film and the substrate and phase analysis were carried out by X-ray diffraction (XRD). The $2\theta-\omega$ (where 2θ is the angle

between the incident and the diffracted X-ray beams and ω is the angle between the incident X-ray beam and the sample surface, see Fig. 3.2) scans between 10° and 120° , the rocking curves (or so-called ω scans) [99], reciprocal space mapping (RSM; i.e. combination of several rocking curves at different diffraction angles, 2θ , see Fig. 3.3 for the basic features of RSMs of epitaxial thin films) and φ scans between 0° and 360° were performed using a four-circle Bruker D8 Discover diffractometer, equipped with a Cu X-ray tube, Göbel mirror, 4-bounce 022 Ge channel-cut monochromator (to select only the Cu $K\alpha_1$ radiation), Eulerian cradle and a scintillation counter. The pole figures of the specimens were measured using Cu $K\alpha$ radiation in a Philips X'Pert MRD diffractometer equipped with an Eulerian cradle and operating in parallel beam geometry.

For calculating the lattice parameters accurately, position of the substrate peak was employed as internal reference. Afterwards, lattice spacings were plotted against the Nelson-Riley function [100], $\cos^2 \theta^* \left(\frac{1}{\theta} + \frac{1}{\sin \theta} \right)$, and the corrected values were obtained from the intercept of the linear fit applied to the data. This method is widely used to eliminate instrumental errors as well as errors from absorption in the specimen and sample displacement.

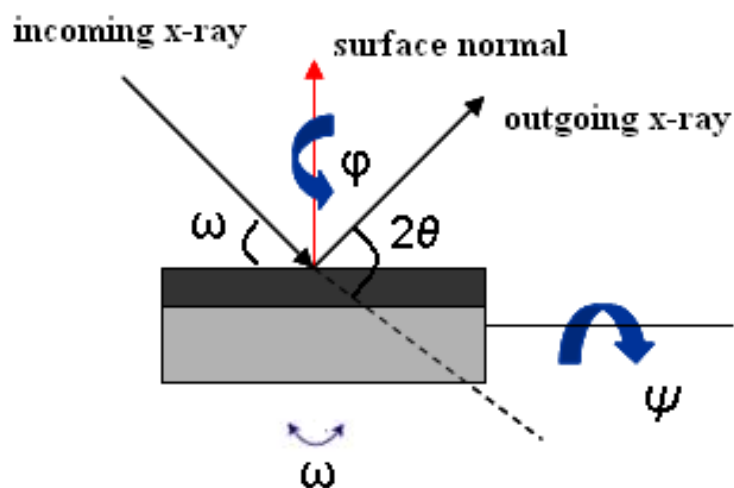


Fig. 3.2: A systematic view of different angles in the XRD.

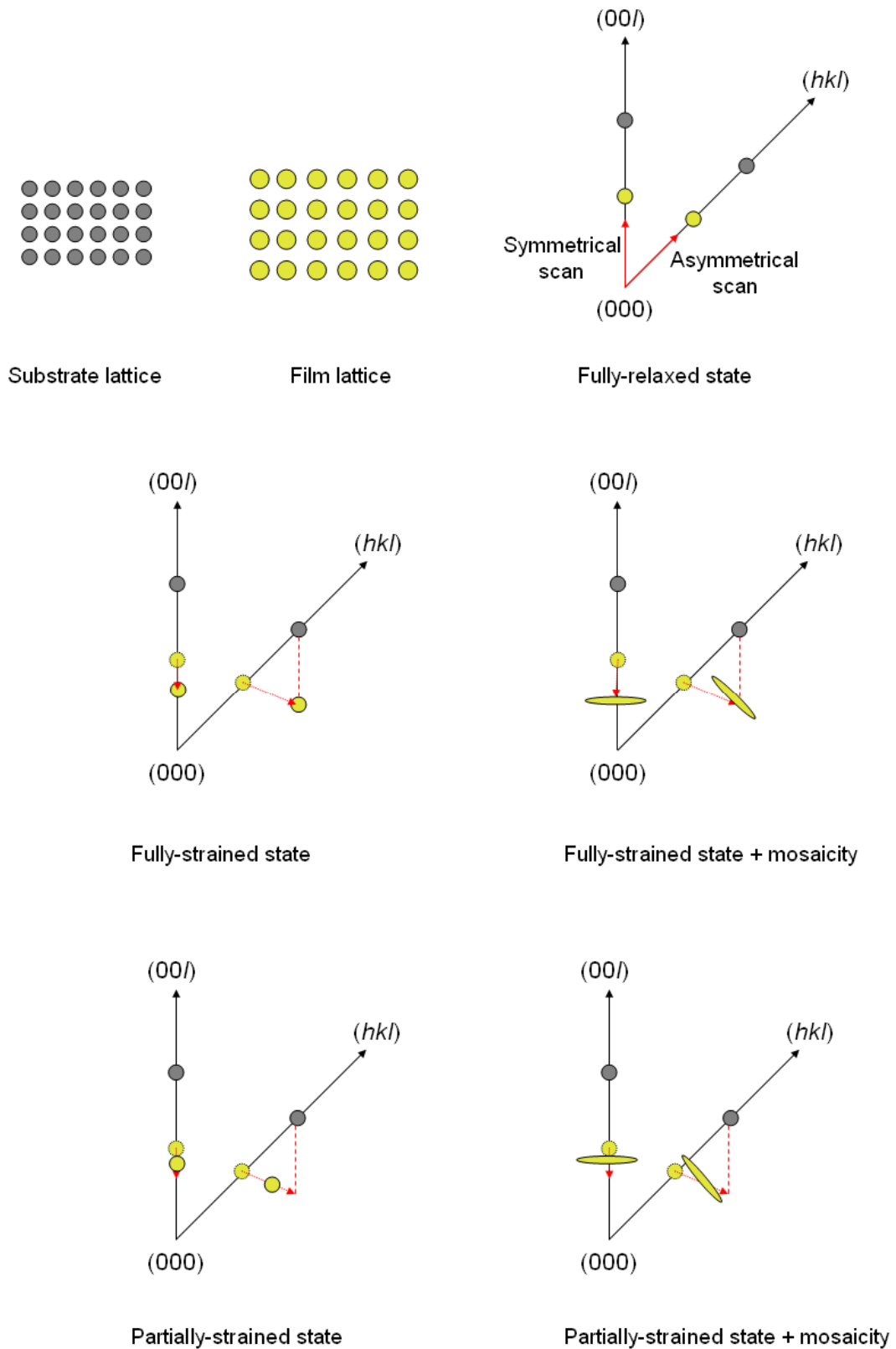


Fig. 3.3: Basic features in reciprocal space maps of epitaxial thin films.

3.1.3 High-resolution transmission electron microscopy

High-resolution transmission electron microscopy (HR-TEM) was performed on a JEOL 4000 FX operating at 400 keV and having a point resolution of 0.17 nm in the Stuttgart Center for Electron Microscopy.

The cross-sectional TEM specimens were prepared by ion-beam thinning as follows. A thin slice consisting of a single piece of material was cut from the sample. Thereafter, samples were embedded into a cylindrical polycrystalline Al_2O_3 tube of 3 mm diameter. Then, the tube was cut into slices having an approximate thickness of 350 μm . The slices were thinned by mechanical grinding, dimpling from both sides and ion milling (using a GATAN PIPS with 3.5 kV Ar ions at an incidence angle of 8° with liquid nitrogen cooling) for several hours to obtain electron transparency. Afterwards, the thin specimen was cleaned at a low-voltage of 1.5 kV in a Fischione 1010 (low-angle ion milling and polishing system) to remove any amorphous material deposited during ion milling. Details of the cross-sectional specimen preparation can be found in Ref. [101].

3.2 Magnetic measurement

The temperature dependence of magnetization was investigated by a Quantum Design Magnetic Property Measurement System (MPMS) and a Quantum Design Vibrating SQUID (superconducting quantum interference device) Magnetometer (VSM). It consists of superconducting magnetic shield and superconducting pickup coils in the vacuum flask. The working principle is the measurement of the flux change through a pick-up coil system.

The magnetic field (0.01 and 1 T) was oriented parallel and perpendicular to the film surface during field cooling (FC) and zero field cooling (ZFC). During ZFC, samples first were cooled to 5 K then field was applied to sample. Afterwards, magnetization was measured in the heating process up to 300 K. During FC, samples were cooled from 300 K down to 5 K in the same field. It is noted that magnetization measurements were also performed for substrates without film, because the data can be subtracted from the results obtained for particularly thinner films in order to eliminate the possible contribution –at high applied magnetic field- to the magnetization from the substrate (diamagnetic character), the holder and the glue employed to fix the specimens.

3.3 Transport measurement

Resistivities of the films were measured within the temperature range between 5 K and 300 K by four-point probe method. A constant DC current (varied between 10^{-7} and 10^{-4} A) is passed through the two outer leads while the potential drop across the sample is measured from the two inner leads. Evaporated chromium/gold pads (20 nm/200 nm) prepared by photolithography in Technology Service Group, Max Planck Institute, described in Fig. 3.4. First, a layer of photoresist with a constant thickness of about 1.2-1.5 μm was applied on top of the film by spin coating. Before and after spin coating, samples were backed at around 100°C for removing any traces of contamination on the surface and hardening the resist, respectively. In the next step, after the mask alignment, the light-sensitive resist was illuminated through a photomask with UV light. The photoresist was then developed using an appropriate alkaline solvent, removing those parts of the resisting material that were previously exposed to UV light. Finally, samples were post-baked to improve adhesion and if it is necessary, any residue of the resist can be carefully removed with Ar plasma. While preparing the contact, silver epoxy were used to attach the gold wires having a diameter of 100 μm to the film surface, as shown in Fig. 3.5. The current source was a programmable Keithley-220 and the voltage was recorded by an HP-8440. Afterwards, the resistivity values were determined from the measured resistance, R , and the parameters related to the sample and the measurement geometry such as the film thickness, t , the mask length, w , and the distance between the voltage contacts, l , according to the relation, $\rho = \frac{R * t * w}{l}$.

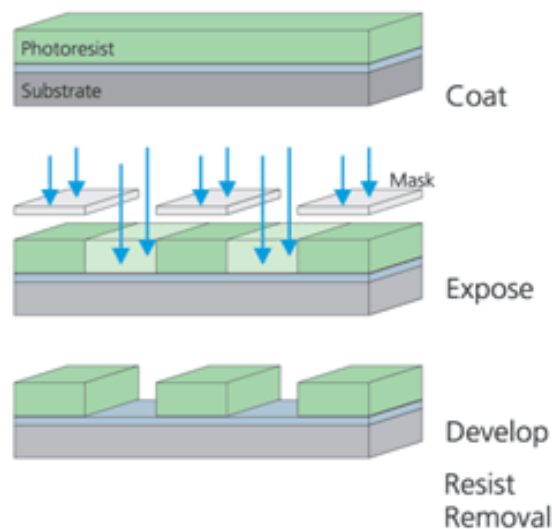


Fig. 3.4: The main steps photolithography for sample preparation.

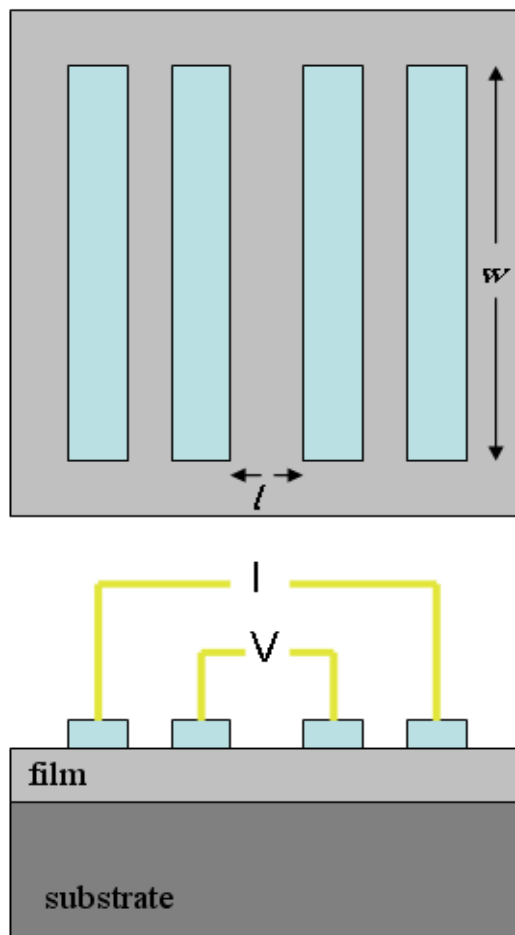


Fig. 3.5: The sample geometry for four-point probe measurements.

The effect of magnetic field on resistivity of the LCMO films on various substrates was investigated employing a Quantum Design Physical Property Measurement System (PPMS) applying magnetic fields of 0.01, 1, 4, 7 T with the same measurement geometry explained above.

3.4 Angle-resolved X-ray photoelectron spectroscopy

X-ray photoelectron spectroscopy (XPS) uses the uniqueness of the kinetic energy of the photoelectrons emitted from certain orbital of a material to determine the chemical state of the

atoms or the ions. It is a surface-sensitive technique due to the relatively short attenuation length of the photoelectrons (i.e. about 5 nm).

In the present study, experiments were performed with collaboration Dr. Ir. Lars P.H. Jeurgens by a Thermo VG Thetaprobe angle-resolved XPS (AR-XPS) system, which can detect photoelectrons from a wide angular range (i.e. between 23° and 83°) without tilting the sample, under ultra-high vacuum conditions (base pressure was lower than 5×10^{-8} mbar). The above-mentioned feature of the setup gives the opportunity to have depth dependent information. The Al K α X-ray beam is focused down to a spot size of 15 μm . The instrument is combined with a floodgun to avoid charging effects on insulating surfaces [102].

3.5 Raman spectroscopy

In Raman scattering experiment, light of a known frequency and polarization is scattered from the specimen. The frequency of the inelastically scattered light is shifted up or down due to vibrational, rotational and other low frequency transitions specific to the sample under investigation. Consequently, Raman spectroscopy is regarded as a powerful tool providing information about the internal structure of molecules and crystals.

The Raman spectra were measured employing a T64000 Jobin-Yvon triple spectrometer, equipped with a liquid nitrogen cooled charge coupled device and a microscope in the department of Prof. Dr. Efthymios Liarokapis. The low temperature measurements were performed in an Oxford cryostat. The 514.5 nm line of an Ar⁺ laser was used for excitation at low power (power was kept constant at ~0.2 mW during the measurements [103-105]).

3.6 X-ray magnetic circular dichroism

X-ray magnetic circular dichroism (XMCD) is a difference spectrum of two X-ray absorption spectra, one taken with left circular polarization and one with right circular polarization (Fig. 3.6). Information about magnetic properties of the atom (e.g. its spin and orbital magnetic moment) can be obtained by analyzing the XMCD spectrum in detail.

The experiments were performed on the WERA beam line of ANKA by collaboration with PD Dr. Eberhard Goering. A custom made XMCD system, having a fast switching superconducting magnet to flip the magnetization of the specimens in an applied magnetic field of 2 T, has been used. The element specific XMCD measurements were carried out at the Mn $L_{2,3}$ edge to obtain the projected magnetic moments stemming from Mn. The

applied magnetic field was systematically flipped at each data point to eliminate drift phenomena and to enhance the sensitivity of the system. Liquid helium and nitrogen were employed to cool the LCMO films below ambient temperature. All measurements were performed in the surface sensitive total electron yield (TEY) mode. Following the measurements, spin and orbital magnetic moments were extracted via the application of sum rules [106, 107] and assuming that the effective number of Mn 3d holes was 6.5 [108, 109].

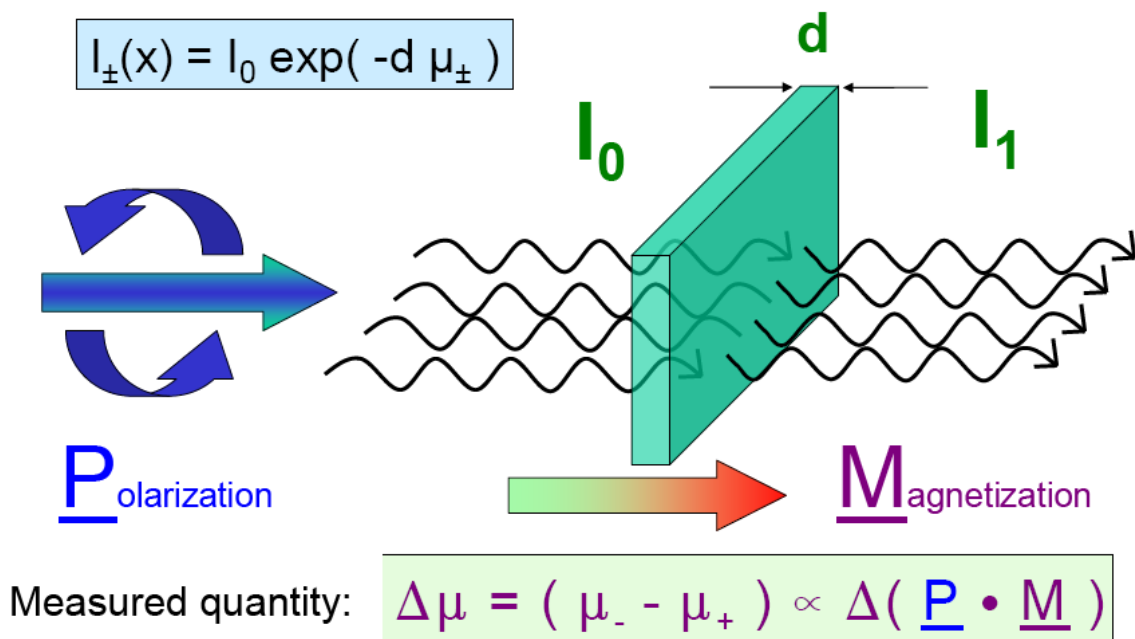


Fig. 3.6: The principle of XMCD measurements [110].

Chapter 4

Results

4.1 Characterization of the LCMO target

As mentioned in Section 1.7, the aim of the present work is to explore the possibility of modifying the properties of LCMO films by mismatch strain, without changing the chemical composition, and by varying the amount of oxygen vacancies in the lattice via heat treatments in vacuum and O₂ environments. The La_{0.5}Ca_{0.5}MnO₃ composition was chosen since it is at the boundary between the CO-AFM and the FM phase fields according to bulk phase diagram. Hence, small external perturbations are expected to change the relative amounts of these phases and cause significant variations in the measured transport and magnetic properties of the specimens.

Prior to thin film growth, the target composition was analysed by inductively coupled plasma optical emission spectrometry (ICP-OES) [111] which indicate the quantitative concentration of elements via the intensity of emitted characteristic electromagnetic radiation from excited atoms produced by inductively coupled plasma. It is confirmed that target contains La, Ca and Mn in a 1:1:2 ratio.

The target material was also characterized by XRD. The 2θ - ω scan pertaining to the LCMO target is shown in Fig. 4.1. According to the refinement performed by DASH software [112], target material has FeGdO₃ type structure, which belongs to the *Pnma* space group. The refined lattice parameters for the orthorhombic cell are $\alpha=\beta=\gamma=90^\circ$, $a=0.5409$ nm, $b=0.7649$ nm and $c=0.5410$ nm. It is noted that the lattice parameters obtained from the refinement match nicely to the literature data reported for La_{0.5}Ca_{0.5}MnO₃ composition [113].

Magnetization of the bulk target was measured during cooling from 300 K to 5 K under an applied field of 0.01 T. It is evident from Fig. 4.2 that there are two magnetic transitions, which are consistent with the expected behaviour of this composition. The first one is a paramagnetic to ferromagnetic transition with a Curie temperature (T_C) around 270 K and the second is a ferromagnetic to antiferromagnetic transition when 150 K (i.e. the Neel temperature, denoted by T_N) is reached [114]. The saturation magnetization is approximately $0.18 \mu_B/\text{Mn}$ ion which is less than the theoretical saturated magnetic moment of $3.4 \mu_B/\text{Mn}$ ion [115].

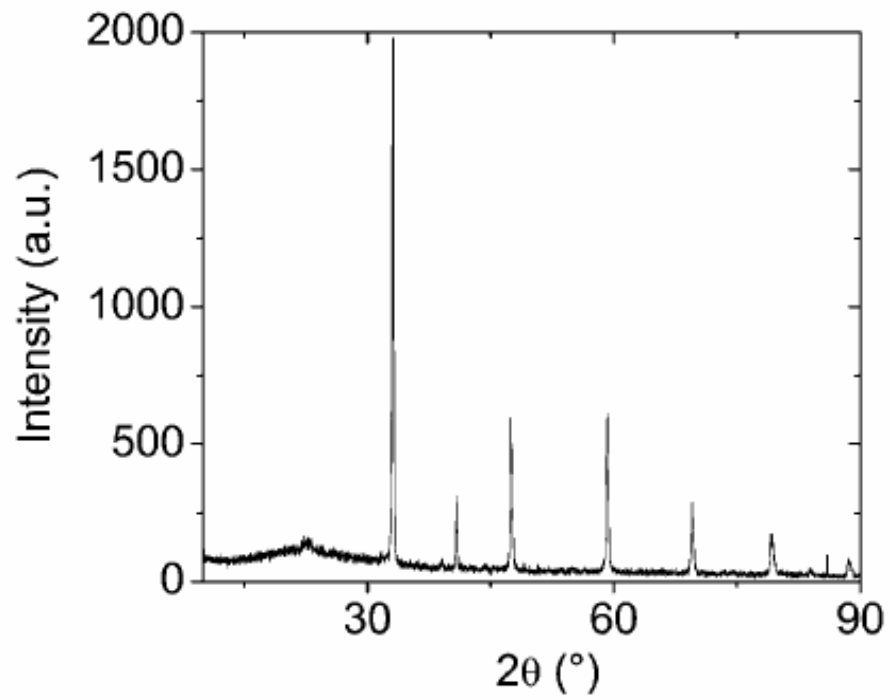


Fig. 4.1: The 2θ - ω scan of the LCMO target.

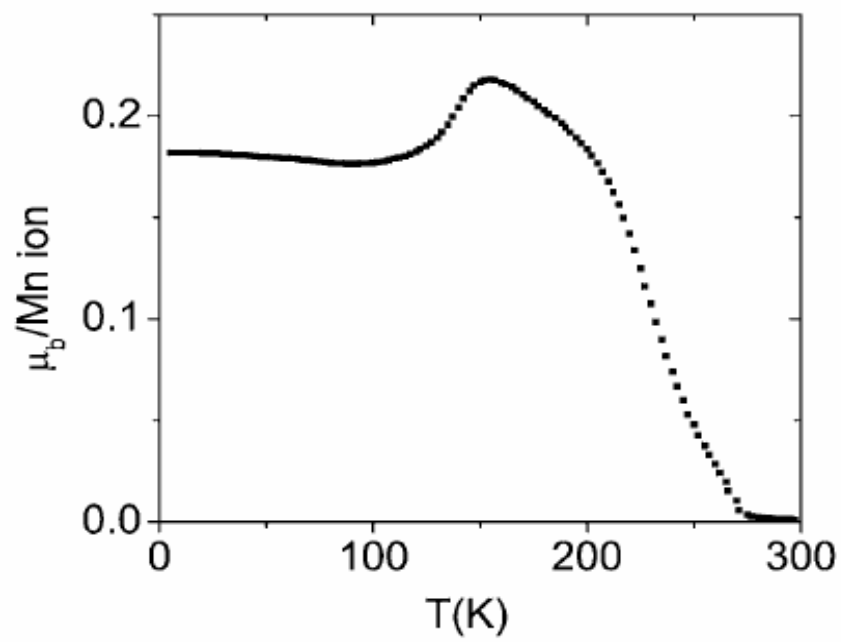


Fig. 4.2: Magnetization versus temperature graph of bulk.

4.2 Characterization of the LCMO thin films

The surface of the substrate is of cardinal importance for the deposition of highly epitaxial thin films of manganites. For the polished single crystalline substrates, the plane that should be parallel to the surface may be slightly misoriented due to inevitable limitations of the fabrication process. The AFM image of an (001) STO substrate after the heat treatment in constant O₂ flow at 1223 K for 1 h is shown in Fig. 4.3. The steps of about 120 nm long are clearly seen and the angle of misorientation is approximately 0.2° (cf. Fig. 4.3(b)).

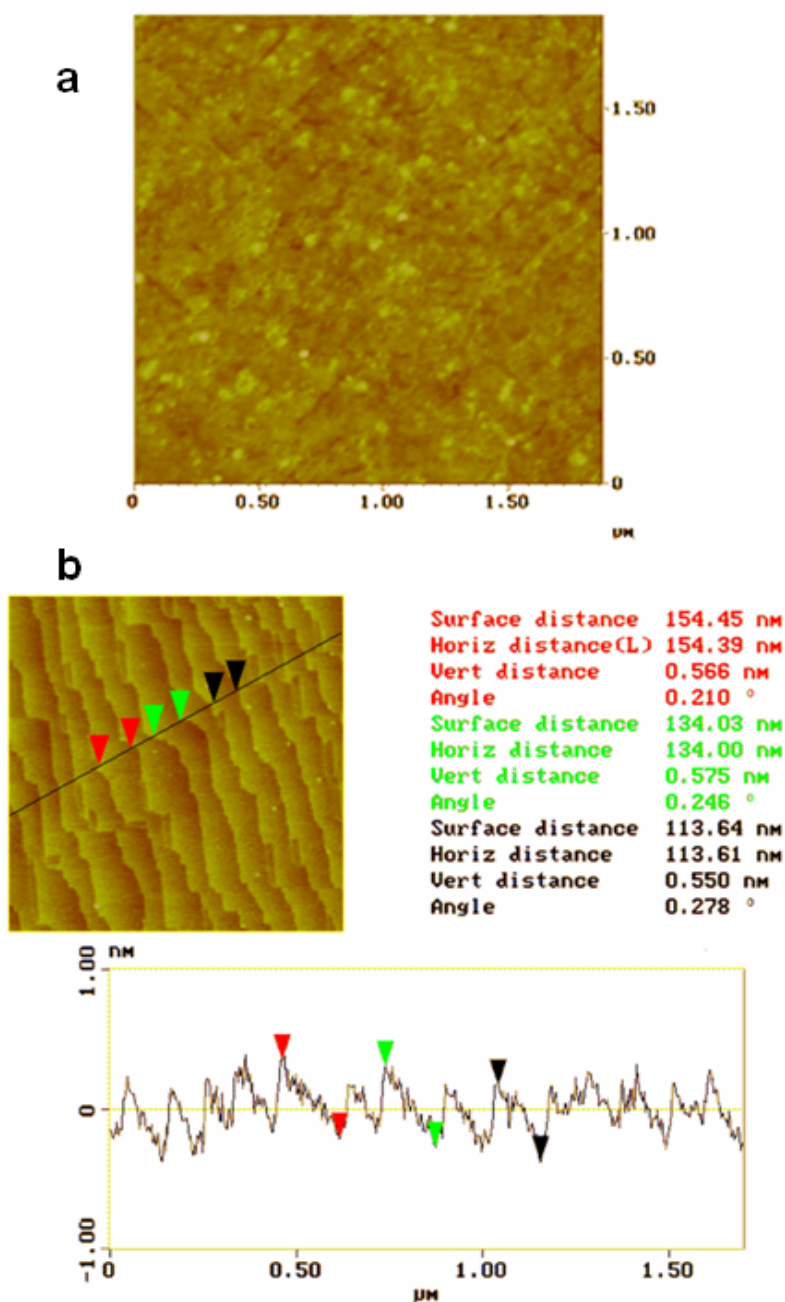


Fig. 4.3: AFM image of (a) as-received and (b) annealed STO substrate.

4.2.1 The LCMO films on (001) STO substrate

The AFM images of the LCMO thin films on (001) STO substrate are presented in Fig. 4.4. The surface morphologies of all films have similar features, pertaining to island-growth mode. However, some differences exist in the mean grain sizes and the root mean square (RMS) roughness values. Thinner films are considerably smoother than the thicker ones. For instance, RMS roughness (over $4 \mu\text{m}^2$ area) and mean grain size area values increase systematically from 0.8 nm to 4.8 nm and from 6305 nm^2 to 15557 nm^2 , respectively while the film thickness is increased from 40 nm to 290 nm.

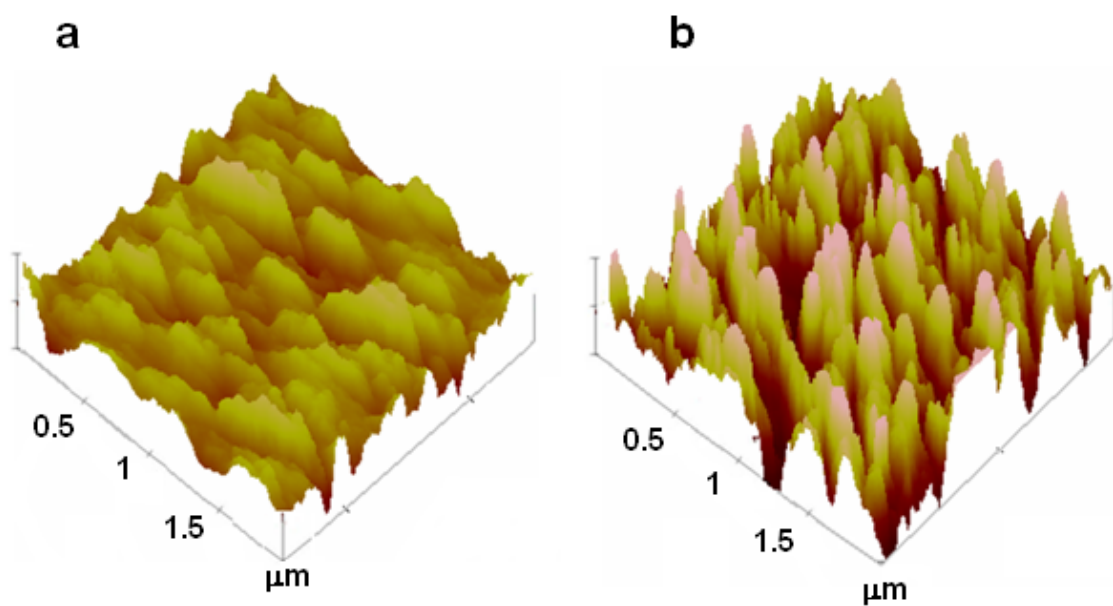


Fig. 4.4: AFM images of the (a) 40 nm and (b) 290 nm thick films on (001) STO.

The 2θ - ω scans show that all samples are single phase and have orthorhombic crystal structure. A 2θ - ω scan, representative for the LCMO films on (001) STO is shown in Fig. 4.5; only $0k0$ reflections can be identified in the diffractogram. The lattice parameters of the LCMO films with different thicknesses are summarized in Table 4.1; a clear trend is not observed in the lattice parameters with changing film thickness. The $\{121\}$ pole figure of the films on (001) STO is presented in Fig. 4.6(a). There are only four peaks at $\psi=43.9^\circ$ which is consistent with the angle between (121) and (020) planes of LCMO. Epitaxial notation of the

films on (001) STO can be described by (100) STO // (020) LCMO: [110] STO // [100] LCMO and [-110] STO // [001] LCMO relations. The b lattice parameter of LCMO films is oriented perpendicular to the substrate surface; the a and c edges of the LCMO unit cell correspond to the face diagonals of the cubic STO unit cell (cf. Fig. 4.6(b)). Rocking curve measurements reveal that full width at half of the maximum (FWHM) intensity, inversely proportional to the degree of crystallinity, of these films does not show a monotonous trend as a function of thickness (see Fig. 4.7).

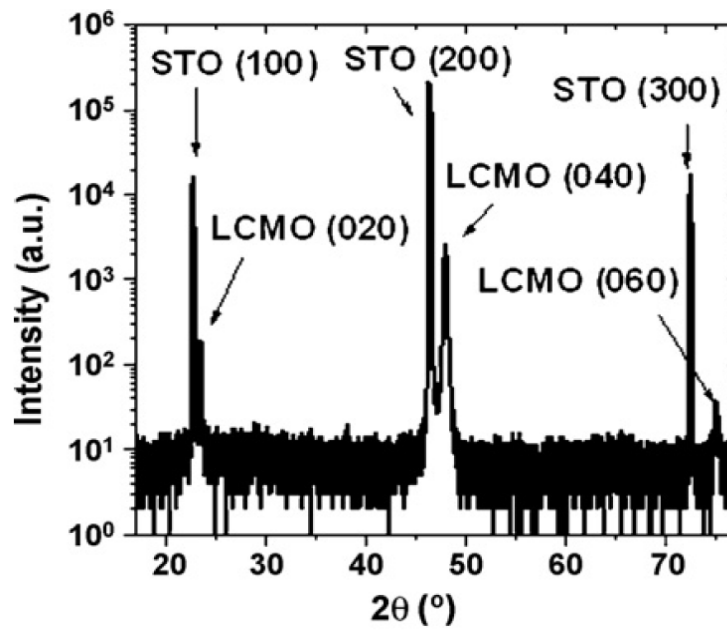


Fig. 4.5: Representative 2θ - ω scan of the LCMO films on (001) STO.

Table 4.1: Lattice parameters of the LCMO films having various thicknesses and deposited on (001) STO.

Film Thickness (nm)	Lattice Parameter a (Å)	Lattice Parameter b (Å)	Lattice Parameter c (Å)
20	5.4014	7.5758	5.4938
40	5.3624	7.5471	5.6227
60	5.4175	7.5622	5.5666
80	5.4114	7.5374	5.5843
100	5.4237	7.5460	5.6131
120	5.4009	7.5240	5.5730
145	5.4056	7.5386	5.5597
220	5.4107	7.5578	5.5516
290	5.4151	7.5816	5.5287

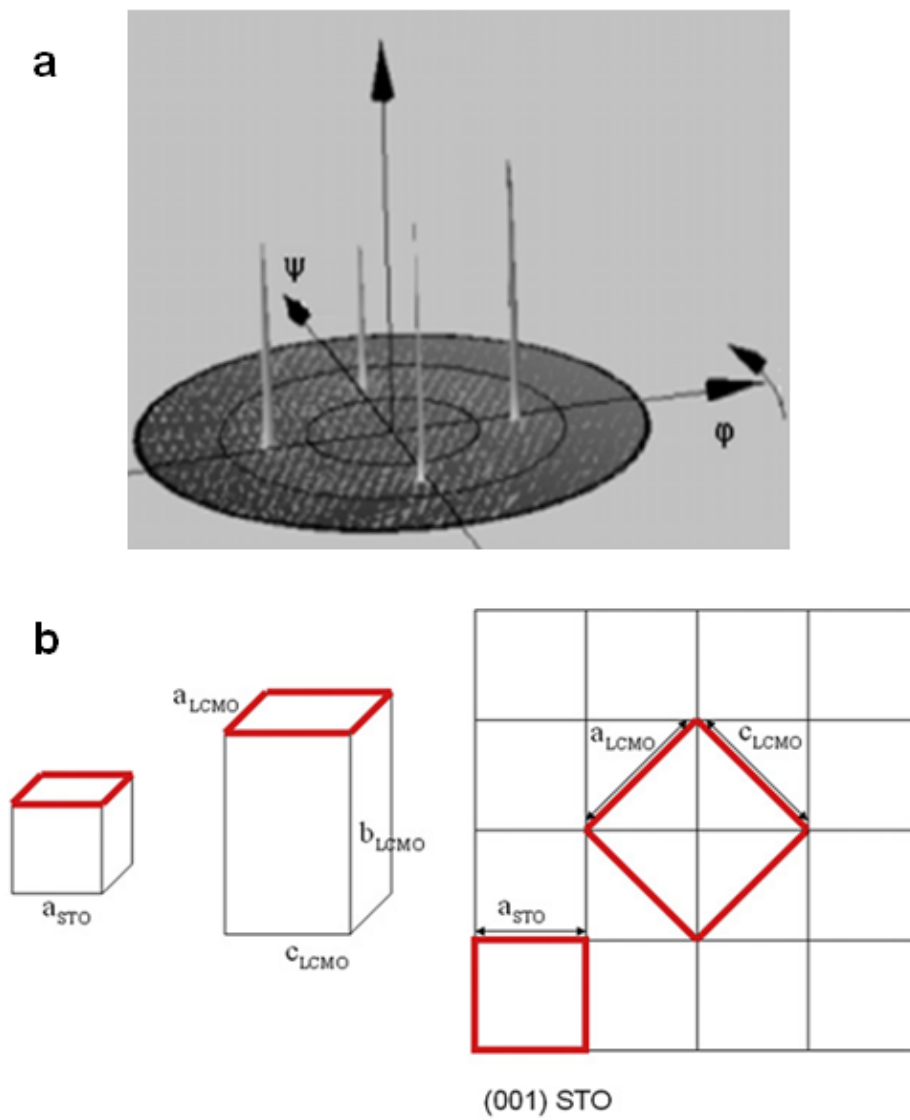


Fig. 4.6: (a) Pole figures of LCMO films on (001) STO and (b) their epitaxial orientation.

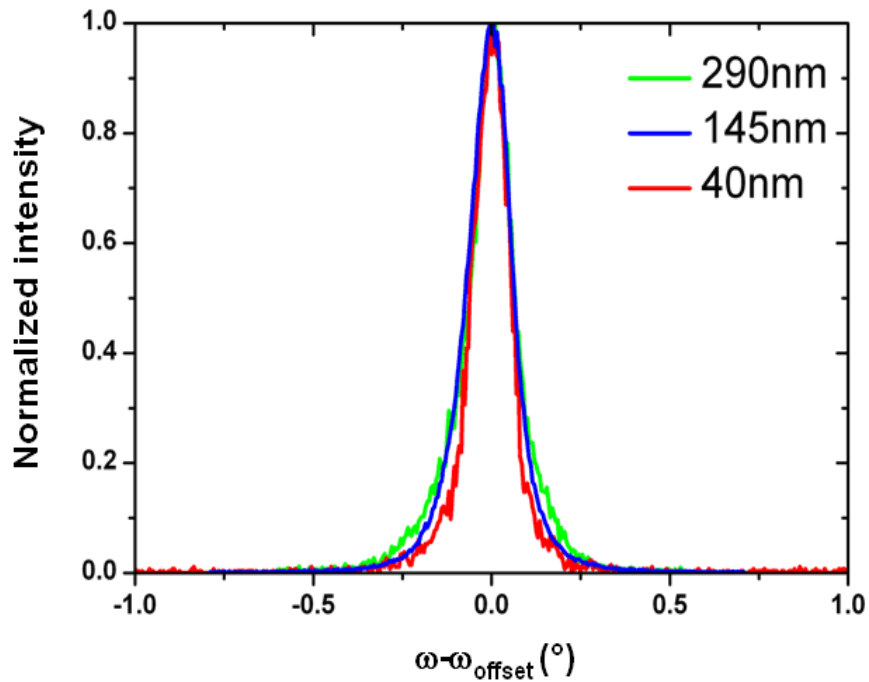


Fig. 4.7: The rocking curves measured around the 040 reflection of LCMO; the films are deposited on (001) STO.

The variation of magnetization with temperature is measured between 5 K and 300 K at 0.01 T magnetic field (cf. Fig. 4.8). Determination of the Curie temperature (T_C) is difficult due to the absence of a sharp ferromagnetic transition and magnetization increases almost linear with temperature in the entire range. The saturation magnetization values are considerably smaller than the value of theoretical saturated magnetic moment (i.e. $3.4 \mu_B/\text{Mn}$ ion). The thermo-magnetic irreversibility, ΔM [116], related to the degree of magnetic inhomogeneity in the films, is expressed by $\Delta M = (M_{FC} - M_{ZFC}) / M_{FC}$ where M_{FC} and M_{ZFC} are the magnetization values at a certain temperature during FC and ZFC, respectively. Large thermo-magnetic irreversibility (i.e. around 90 % under 0.01 T applied field) between the ZFC and FC magnetization curves at low magnetic fields and the cusps appearing on the ZFC curves close to T_C are clearly seen and indicate the existence of spin glass like behaviour [117] since there is a magnetic randomness (short range spin ordering) and the application of low magnetic field is not sufficient to rotate the spins in the direction of the field. It was previously proposed that the spin-glass-like behavior in LSMO epitaxial films [118] presents

the disordered distribution of Mn^{3+} and Mn^{4+} ions and the competition between FM and antiferromagnetic interactions.

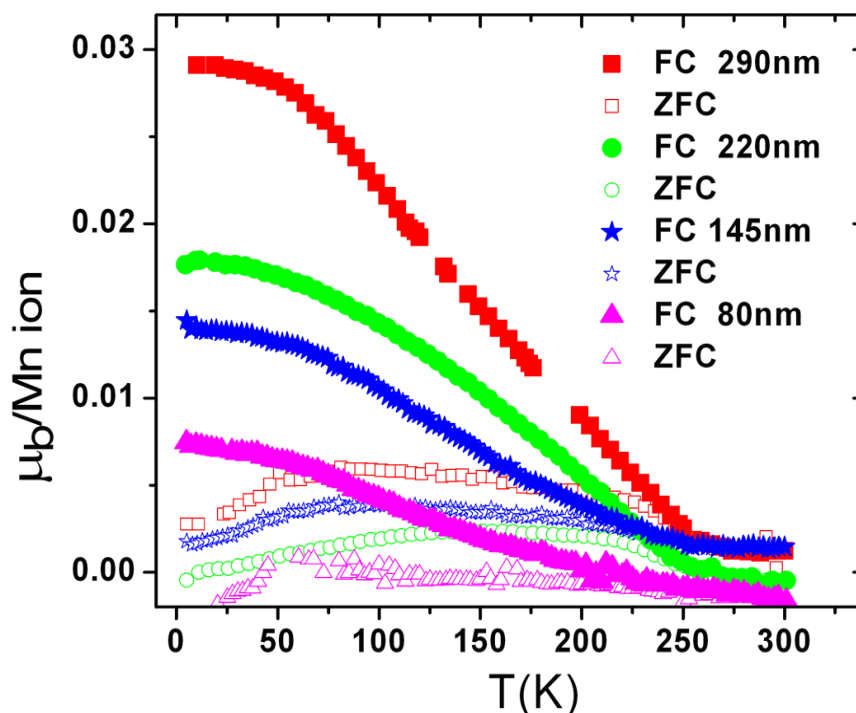


Fig. 4.8: Magnetization versus temperature graphs of LCMO films on (001) STO. Open symbols denote ZFC and closed symbols represent FC.

In order to have more information about the magnetic properties of LCMO films, the element specific XMCD method is applied in surface sensitive TEY mode (sampling depth is approximately 5 nm). The XMCD curve obtained from the difference between the X-ray absorption spectra at the Mn $L_{2,3}$ edge with in-plane magnetization parallel and anti-parallel to the helicity of the circularly polarised light is shown in Fig. 4.9 for the 40 and 145 nm thick films. The magnetic field applied during the measurement is 2 T. It is seen that XMCD signal and magnetization are very weak, which is consistent with the bulk magnetization results presented in Fig. 4.8; spin magnetic moments obtained from XMCD are 0.1 and 0.15 μ_b/Mn for 40 and 145 nm thick films, respectively. The XMCD measurements of 40 and 145 nm thick LCMO films are carried out at 80 and 20 K, respectively.

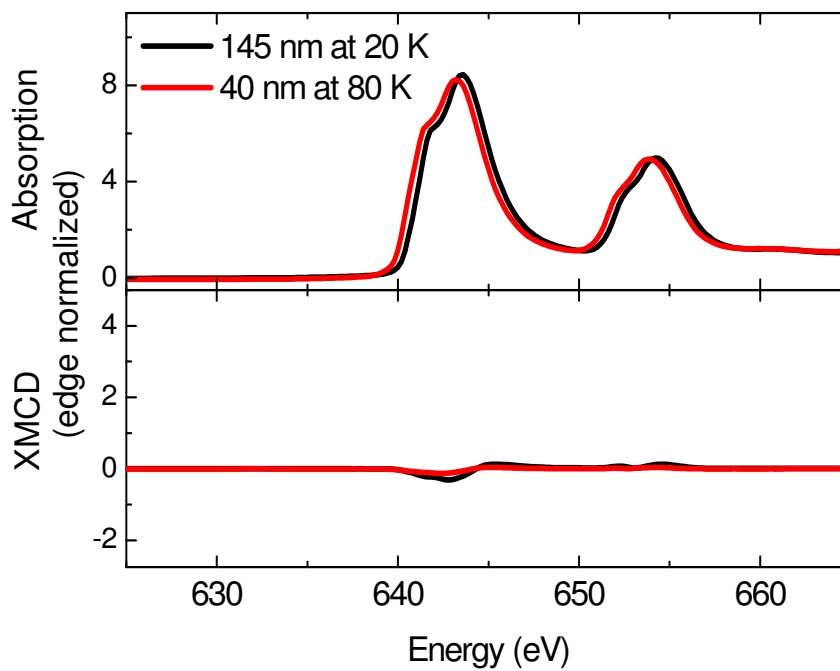


Fig. 4.9: The nonmagnetic XAS spectra and the related XMCD spectra for the films on (001) STO. The spectra have been measured in normal incidence condition.

Transport measurements (cf. Fig. 4.10) show that electrical resistivities of the LCMO films on (001) STO substrate increase with decreasing temperature and only insulator behavior can be observed in the temperature range between 5 and 300 K. It is clearly seen in Fig. 4.11 that the film resistance decreases if a magnetic field is applied. In addition, an insulator to metal transition is observed with decreasing temperature under 7 T magnetic field. These results can be explained via the double-exchange mechanism, describing the coupling between conductivity and ferromagnetism. By the applied field, the volume fraction of FM islands becomes large enough to provide a connection between each other. Therefore a transition from CO/AF insulator state to FM metallic regime occurs.

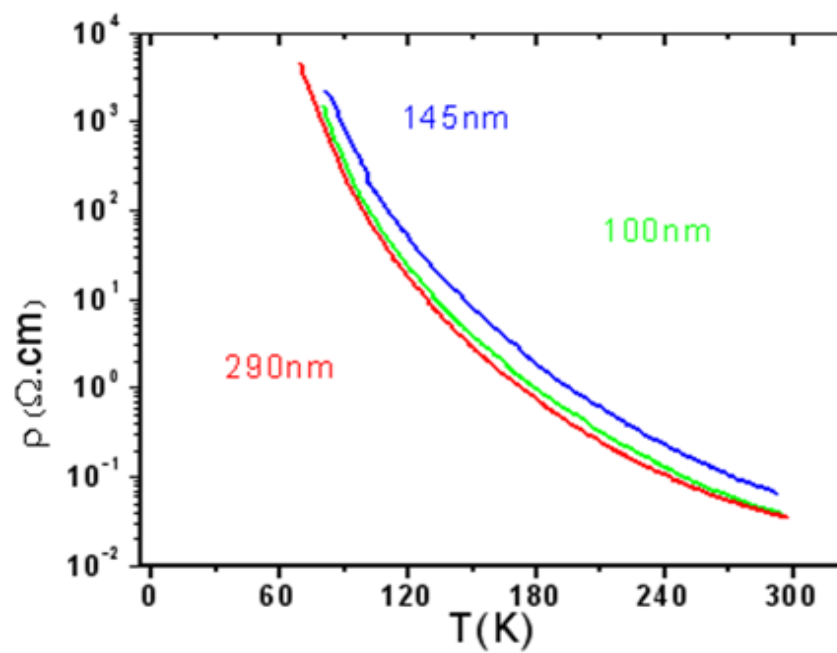


Fig. 4.10: Resistivity versus temperature plots of the LCMO films on (001) STO.

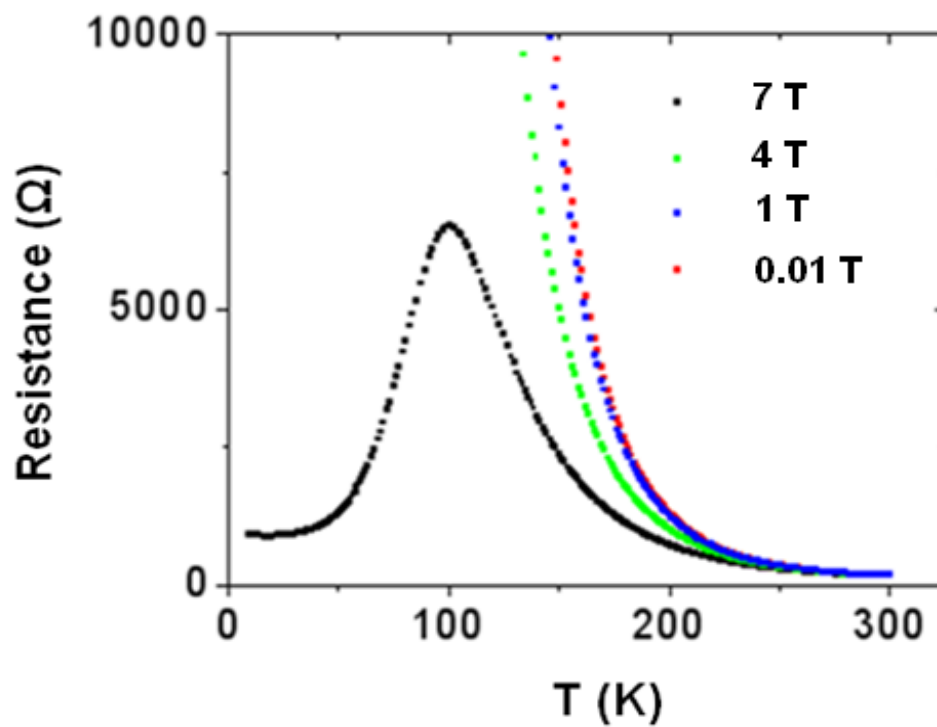


Fig. 4.11: Magnetoresistance behaviour of the LCMO films on (001) STO.

Raman spectroscopy measurements provide valuable information about the lattice distortions and magnetic phase transitions in manganites which have direct influence on the phonon characteristics (e.g. energy, width and intensity of the phonon modes) [119-121]. The orthorhombic RMnO_3 is structurally distorted with respect to the cubic perovskite in two ways: the MnO_6 octahedra present a strong Jahn-Teller (JT) distortion and the octahedra are tilted in order to optimize the R-O bond lengths, where R is the rare-earth ion [122]. The $Pnma$ structure of the films gives $7A_g+5B_{1g}+7B_{2g}+5B_{3g}$ Raman active zone-center optical phonons, which are activated exclusively due to the deviations from the ideal perovskite structure. The Raman spectra of 290 nm thick LCMO film on (001) STO at different temperatures are shown in Fig. 4.12 as a representative of all films on this substrate. It is generally accepted that the low-frequency bands (i.e. the band at around 80 cm^{-1} ; ω_1) are attributed to R-O modes which correspond to mixed vibrations around the xz plane (A_g and B_{2g} symmetry modes) or the y axes (B_{1g} and B_{3g} modes). It gains intensity with decreasing temperature. In addition, in this region a broad feature appear at $\sim 130 \text{ cm}^{-1}$ due to B_{2g} symmetry [123].

The modes related to the tilting of the octahedra with A_g symmetry are seen at 200-300 cm^{-1} (denoted by ω_2). This mode softens close to the expected transition temperature (T_C) which has been reported also by others [124]. Below 150 K, three modes of same symmetry appear in the ω_2 region. This temperature is very close to the reported T_N of the bulk $\text{La}_{0.5}\text{Ca}_{0.5}\text{MnO}_3$ compound, where a similar appearance of new bands has been observed [125, 126]. This has been attributed by Radaelli et al. [127], where orbital and charge ordering takes place below T_N . There is also an alternative case of two co-existing FM and AFM phases [128] with different quantity while altering temperature. Therefore, the change of the ω_2 mode can be correlated with the FM transition and the appearance of the new bands with the AFM transition.

In the region (i.e. ω_3) associated with bending modes, peaks appear at 420 cm^{-1} and 468 cm^{-1} (B_{2g} symmetry) and at 445 cm^{-1} (B_{1g} or the B_{3g} symmetry). The peak at 420 cm^{-1} loses intensity with decreasing temperature below FM, contrary to the peak at 400 cm^{-1} which gains intensity and it attributed to the same B_{2g} bending mode. From their behaviour, it is reasonable to compare the 400 cm^{-1} and 420 cm^{-1} bands with the AFM and FM phase, respectively. These modes have similar intensity at the 210–150K region (FM to AFM/CO) in favour of the two phase coexistence scenario. However, with further decreasing of temperature the 400 cm^{-1} band dominates over the $\sim 420 \text{ cm}^{-1}$ band, which is very weak or absent implying that the FM phase disappear. This is supported by the magnetization data.

The JT stretching modes, approximately at 490 cm^{-1} (i.e. antisymmetric stretching) and 605 cm^{-1} (i.e. symmetric stretching) [122], are clearly visible in Fig. 4.12 and they become more apparent when the temperature is decreased below T_N , implying that the JT distortion is increased [129, 130].

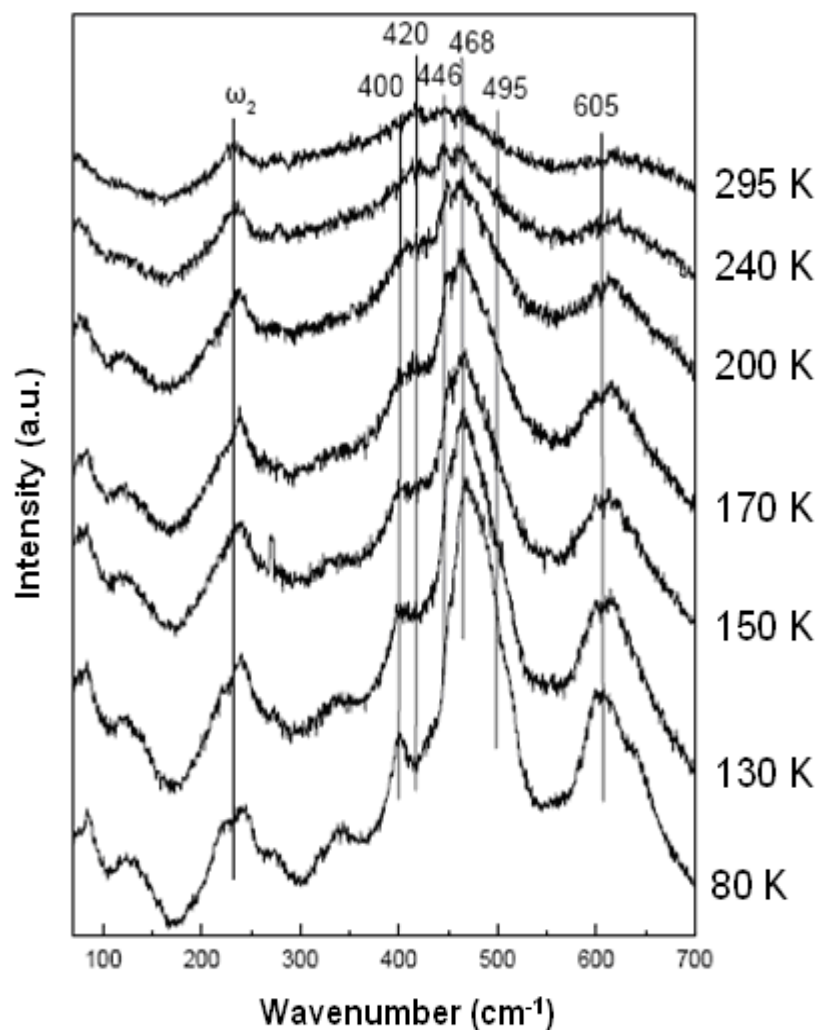


Fig. 4.12: Raman spectra of the LCMO film on (001) STO measured below room temperature. Note that the data are corrected by the thermal factor.

4.2.2 The LCMO films on (111) STO substrate

Representative AFM images for films deposited on (111) STO substrate are shown in Fig. 4.13 according to film thickness between 5-290 nm. The films are considerably smoother than the films on (001) STO (see Section 4.2.1); the RMS roughness values (over $25\ \mu\text{m}^2$ area) of

all films are between 0.5 and 1 nm. The atoms separated from the target form long rods on the substrate surface. With increasing film thickness, these rods accumulate more and more and create a compact web whereas island growth mode dominates and grains become apparent on the surface of the films thicker than 100 nm.

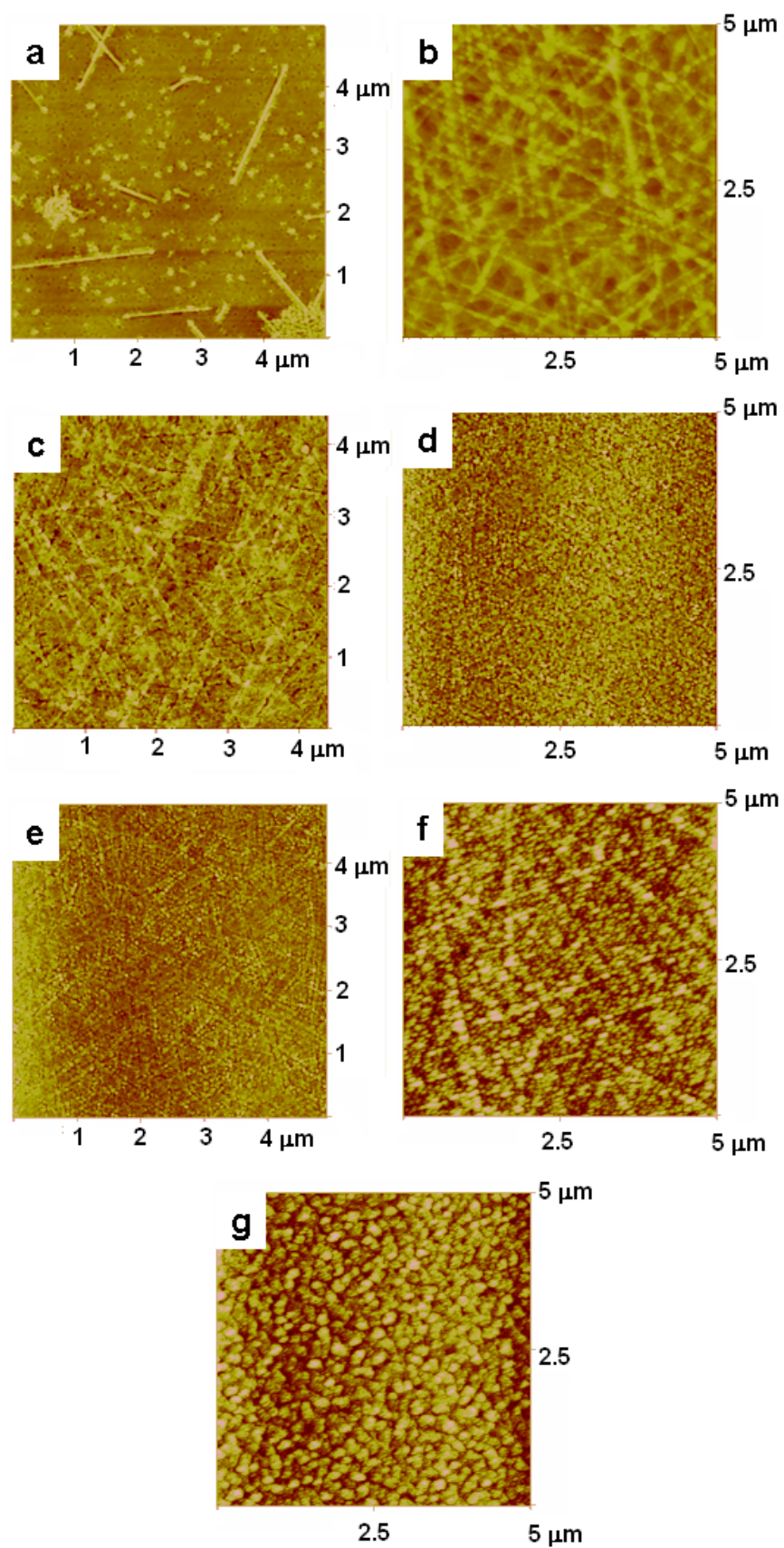


Fig. 4.13: AFM images of films with thickness (a) 5 nm, (b) 20 nm, (c) 40 nm, (d) 120 nm, (e) 145 nm, (f) 220 nm and (g) 290 nm on (111) STO substrate.

The 2θ - ω scans indicate that all LCMO films on (111) STO are single phase and have orthorhombic crystal structure. An exemplary 2θ - ω scan is presented in Fig. 4.14; it is seen that $0kl$ planes of the films are parallel to substrate surface. The measured lattice parameters of the LCMO films of various thicknesses are collected in Table 4.2. With increasing film thickness, the a and c lattice parameters seem to increase whereas the variation in b lattice parameter is sporadic. In order to have a better understanding on the relation of structural modifications with electronic and magnetic properties bond lengths and angles controlling the electron transfer between atoms should be estimated. This estimation and its detailed discussion are given in Chapter 5.

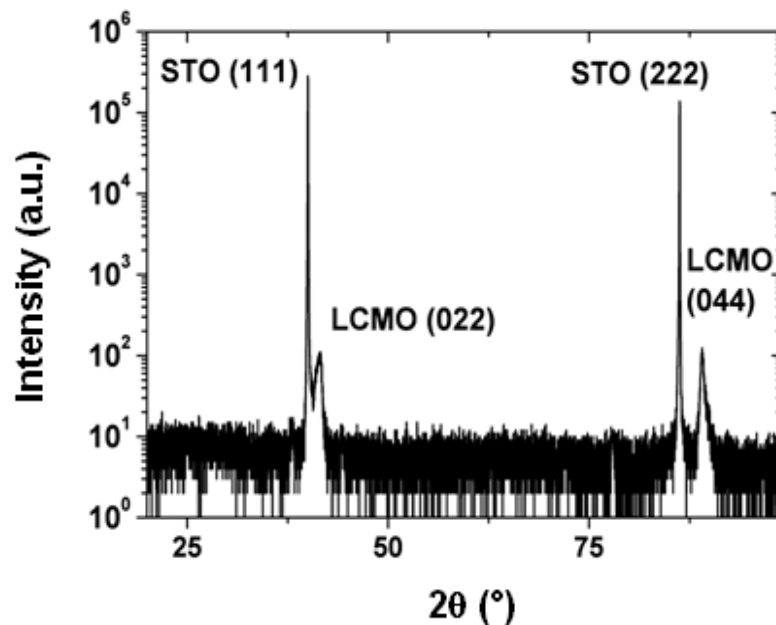


Fig. 4.14: Representative 2θ - ω scan of the LCMO films on (111) STO.

Table 4.2: Lattice parameters of the LCMO films having various thicknesses and deposited on (111) STO.

Film Thickness (nm)	Lattice Parameter a (Å)	Lattice Parameter b (Å)	Lattice Parameter c (Å)
20	5.3898	7.6997	5.2851
40	5.3917	7.6373	5.3742
60	5.4206	7.6912	5.3857
80	5.4124	7.6706	5.3902
100	5.4076	7.7011	5.3949
120	5.4258	7.7057	5.3808
145	5.4295	7.7261	5.3718
220	5.4384	7.7342	5.3791
290	5.4270	7.6775	5.4238

The pole figure of the LCMO films on (111) STO is presented in Fig. 4.15; three-fold symmetry is observed and the inclination angles of the peaks ($\psi=34.7^\circ$) are matching with the angle between (121) and (022) planes of LCMO. The epitaxial relationship between the film and the substrate is described by (111) STO // (022) LCMO: [1-10] STO // [100] LCMO and [11-2] STO // [011] LCMO relations. Therefore, the lattice parameter a and the diagonal of the b - c plane of the LCMO unit cell define a rectangular plane parallel to the (111) STO substrate surface (see Fig. 4.15). It should be noted here that all three lattice parameters are directly affected by the adherence of the film to the substrate.

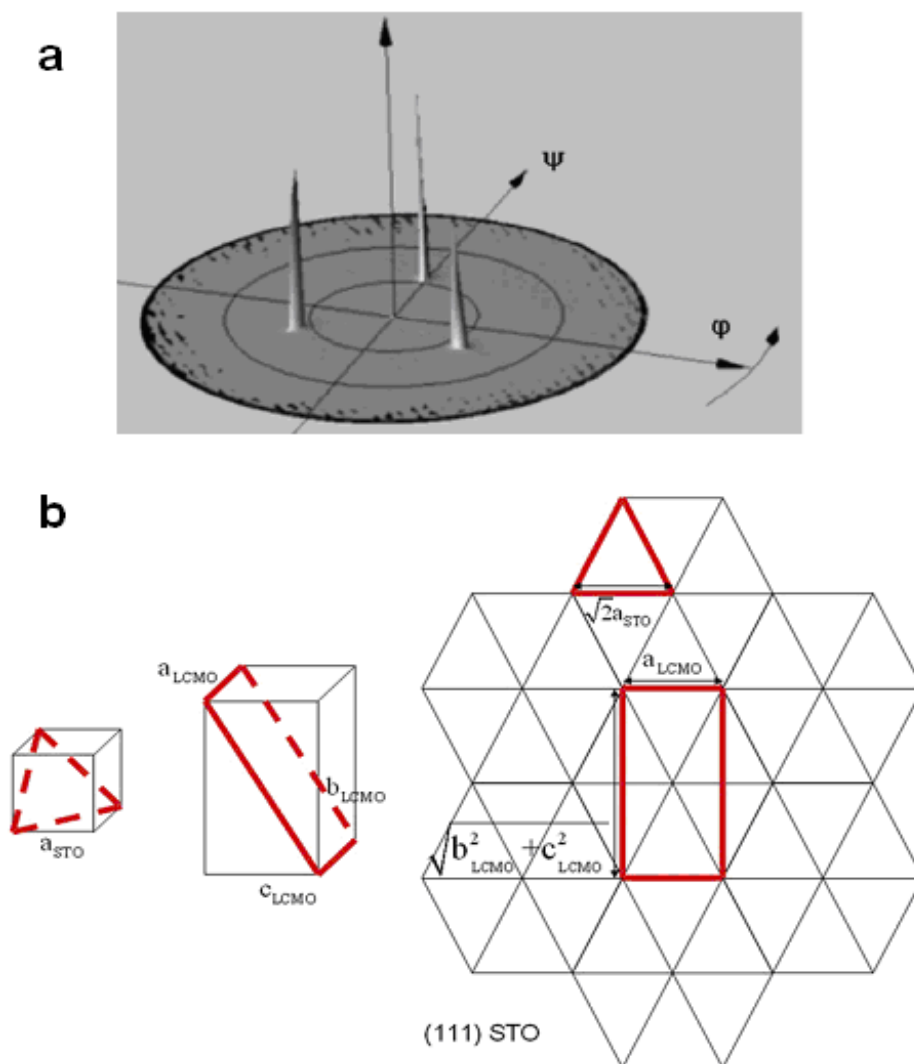


Fig. 4.15: (a) Pole figures of LCMO films on (111) STO and (b) their epitaxial orientation.

The rocking curves of the LCMO films deposited on (111) STO substrates with different thicknesses are compared in Fig. 4.16. Two shoulders are identified to develop on both sides of the main peak for the thicker films (cf. Fig. 4.16). This observation means that the mosaic spread increases and the orientation of the (044) planes deviates more from their initial orientation, parallel to the substrate [131, 132]. The reciprocal space mapping technique is also useful to identify the mosaicity in the films. In this case, the magnitude of the diffraction vector remains unchanged but it is rotated as in Fig. 4.17(b). The apsis and the ordinate of the film reciprocal lattice point give information about the in-plane and out-of-plane lattice parameters, respectively. It should be mentioned that HR-TEM investigations also

reveal the above mentioned peculiar microstructural evolution [133]. Fig 4.18 presents a HR-TEM image of an LCMO film on (111) STO. Starting from a certain distance from the film substrate interface, a defective structure composed of slightly tilted rectangular blocks appears. The formation of this structure may act as a mechanism for the relaxation of strain and local distortions in the LCMO films on (111) STO.

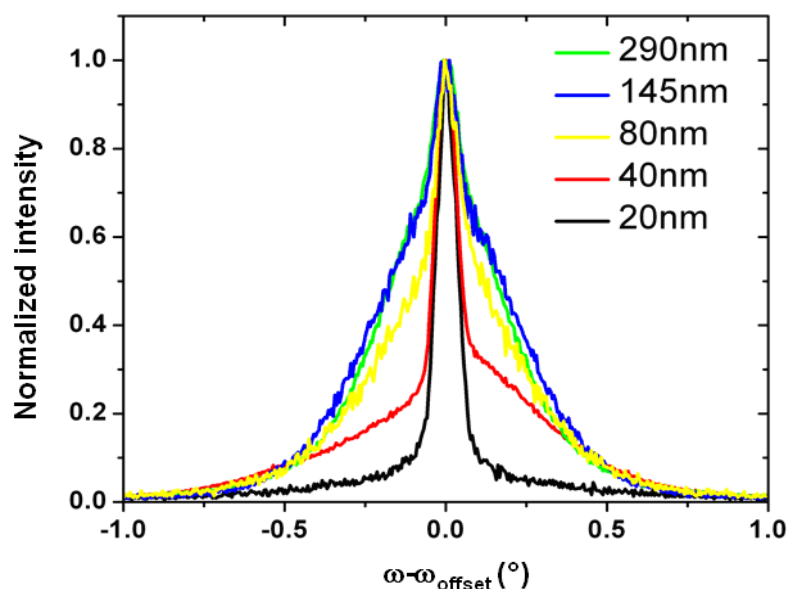


Fig. 4.16: The rocking curves measured around the 044 reflection of LCMO; the films are deposited on (111) STO.

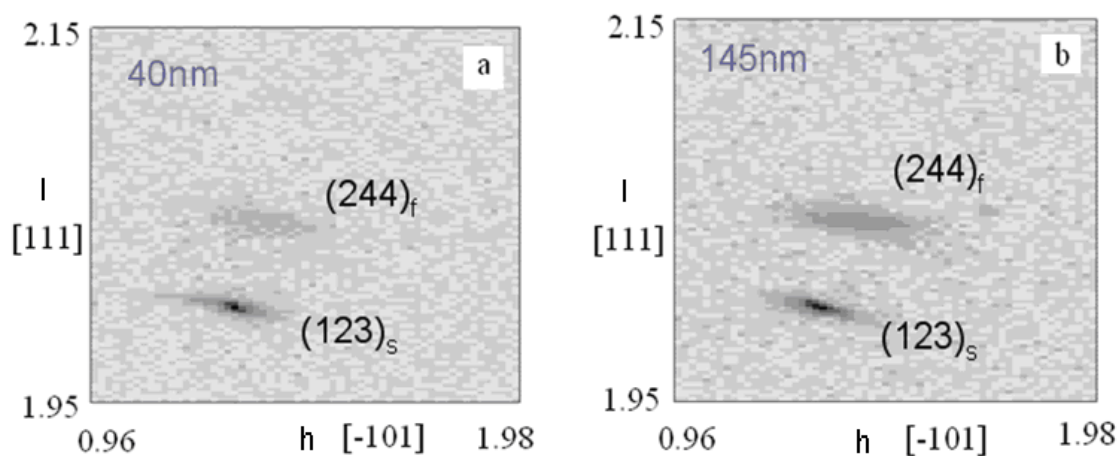


Fig. 4.17: Reciprocal space maps of (a) 40 nm and (b) 145 nm LCMO films on (111) STO.

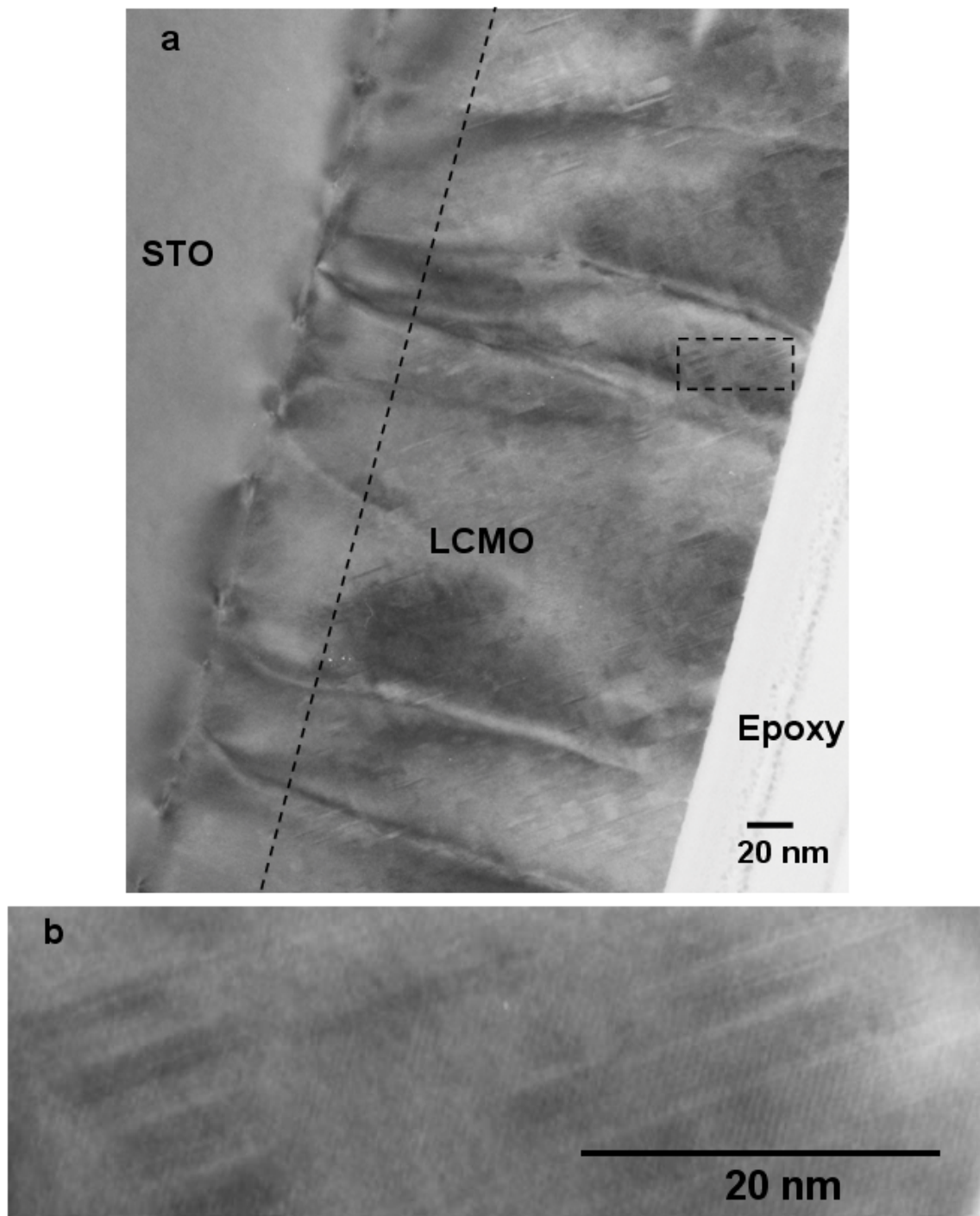


Fig. 4.18: (a) HRTEM image of a representative LCMO film on (111) STO and (b) an enlarged view of the defects. Note that the dashed line and the rectangle show the thickness after which the mosaic structure appears and the enlarged region, respectively.

The variation of magnetization with temperature in LCMO films having various thicknesses deposited on (111) STO is presented in Fig. 4.19. Strong ferromagnetic behaviour is observed; the saturation magnetizations are approximately 50 times larger than the values measured for the films on (001) STO. The T_C increases with thickness and reaches 230 K for 290 nm thick film. This value is still lower than the T_C of the bulk material (i.e. ~ 270 K). In Fig. 4.20 magnetization in 290 nm thick LCMO film is shown as a function of temperature for two orientations (in the first orientation the applied magnetic field is parallel to the film surface whereas the applied field is perpendicular to the film surface in the second one) under two applied fields (i.e. 0.01 T and 1 T). It is seen that there is a remarkable disparity between the magnetization curves pertaining to two orientations under 0.01 T magnetic field although intrinsic magnetoanisotropy of LCMO with a distorted cubic structure is negligible [134]. When the magnetic field is increased to 1 T the thermomagnetic irreversibility (i.e. the difference between the ZFC and FC curves; see Section 4.2.1) decreases since the directions of spin clusters in the spin glass state change more easily from a random state to the direction of the applied field. Moreover, the above mentioned magnetoanisotropy disappears under 1 T magnetic field.

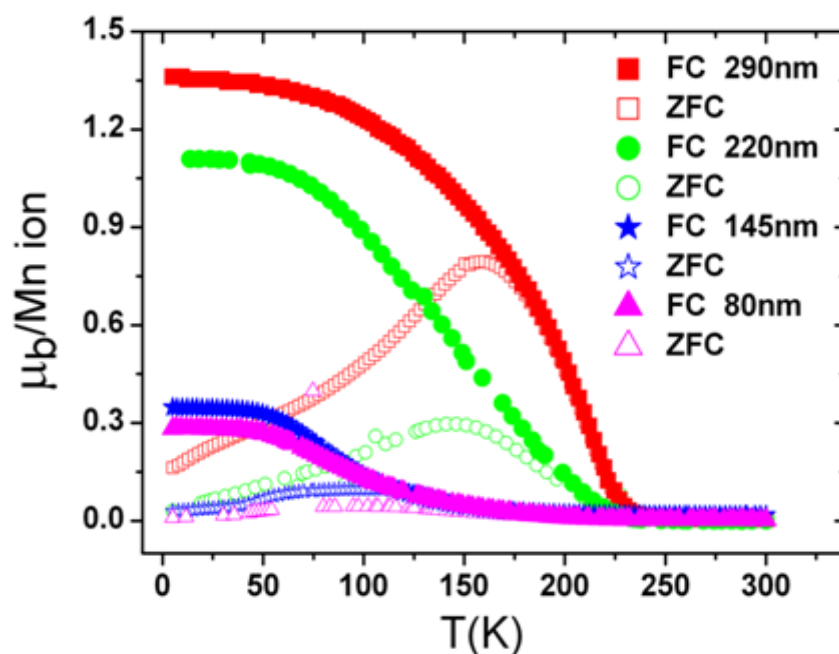


Fig. 4.19: Magnetization versus temperature graphs of LCMO films on (111) STO. Open symbols denote ZFC and closed symbols represent FC.

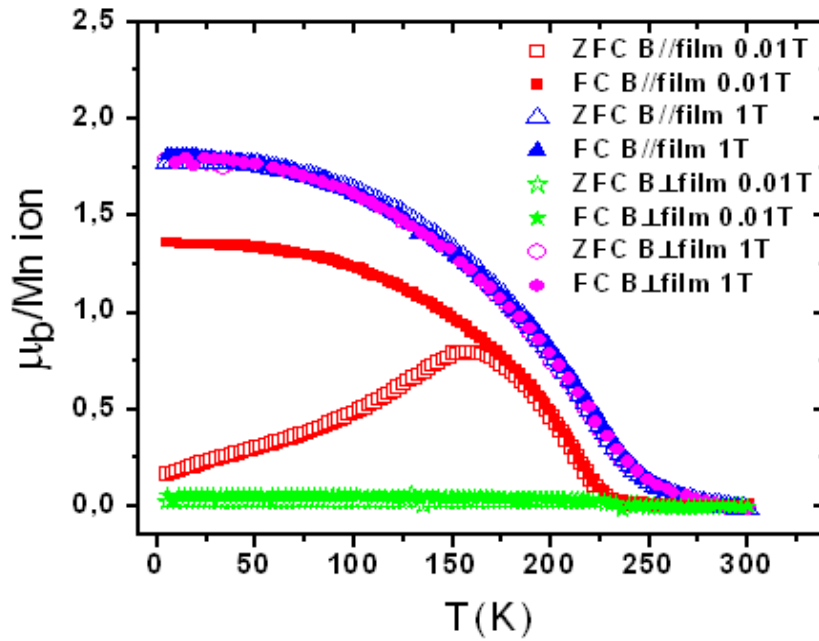


Fig. 4.20: Magnetization versus temperature graphs of 290 nm thick film on (111) STO. Open symbols show zero field cooling (ZFC) and closed symbols represent field cooling (FC).

XMCD measurements are also performed to gain additional information on magnetic properties of LCMO films on (111) STO at 2 T applied field. The measurements at the Mn $L_{2,3}$ edge show strong ferromagnetism with $1.7 \mu_B/\text{Mn}$ spin magnetic moment for 40 nm thick film on (111) STO. This result is qualitatively in line with the SQUID results presented in Fig. 4.19. It should be noted here that the magnetization values obtained from SQUID and XMCD are not directly comparable since SQUID gives information from the whole film thickness and all different atoms contribute to the signal whereas XMCD is element specific and surface sensitive. The same measurement is repeated for 40 nm thick film with an off-normal incidence angle of 60° to monitor a possible anisotropic behaviour. It is seen that only a small variation is observed in the XAS and XMCD spectra after tilted. The 145 nm thick LCMO film exhibits a much weaker XMCD signal and a smaller spin magnetic moment (i.e. $0.35 \mu_B/\text{Mn}$). This result may stem from a reduction in surface magnetization due to relaxation of strain in the surface region.

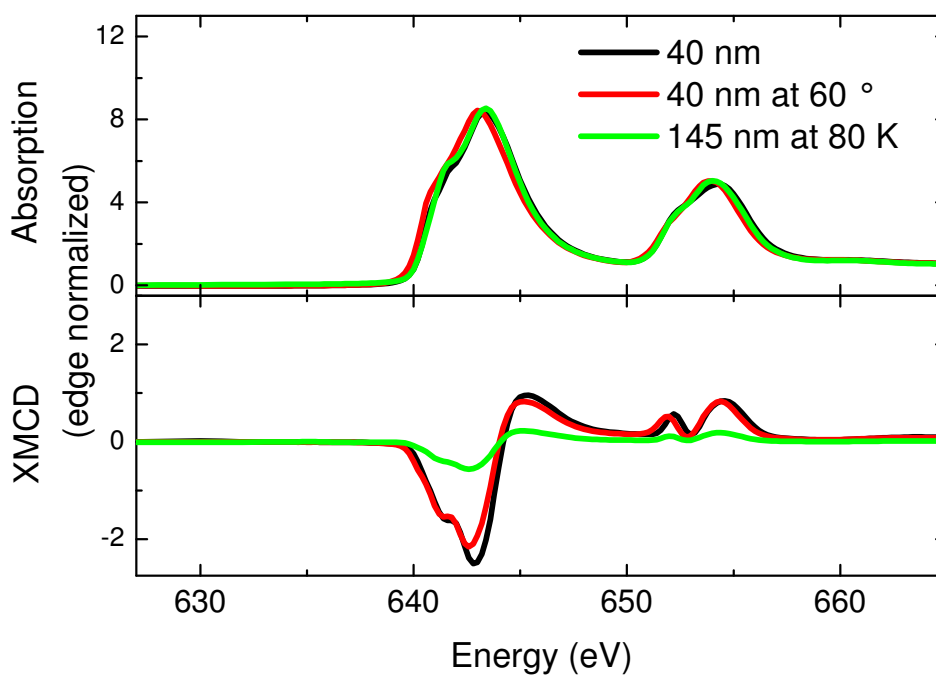


Fig. 4.21: The nonmagnetic XAS spectra and the related XMCD spectra for the films on (111) STO. If not indicated, the spectra have been measured in normal incidence condition.

Transport measurements of the LCMO films on (111) STO are shown in Fig. 4.22 and Fig. 4.23. An insulator to metal transition occurs during cooling for the films when film thickness is equal or larger than 145 nm. The transition temperature, T_{MI} , is positively correlated with the film thickness and it approaches to room temperature with the application of high magnetic fields (cf. Fig. 4.25).

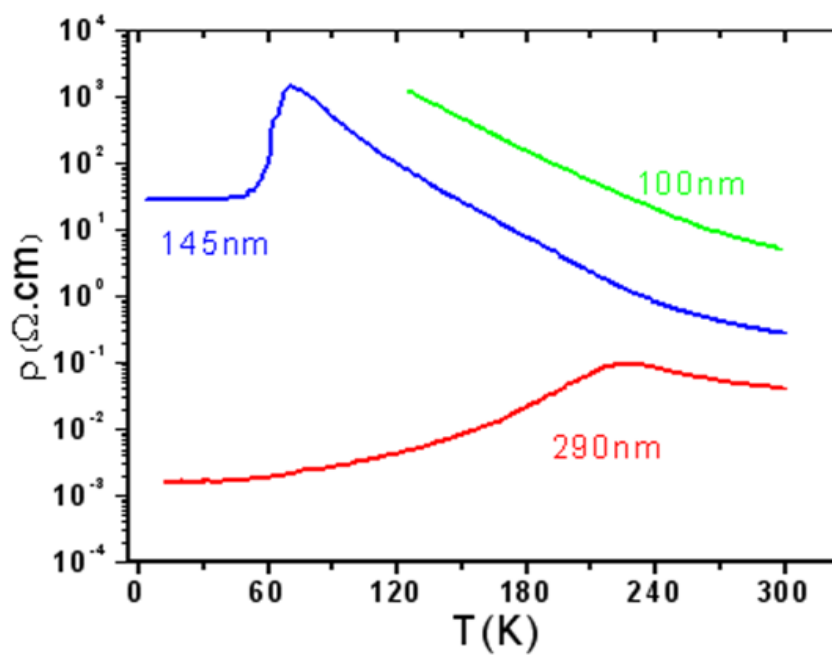


Fig. 4.22: Resistivity versus temperature plots of the LCMO films on (111) STO.

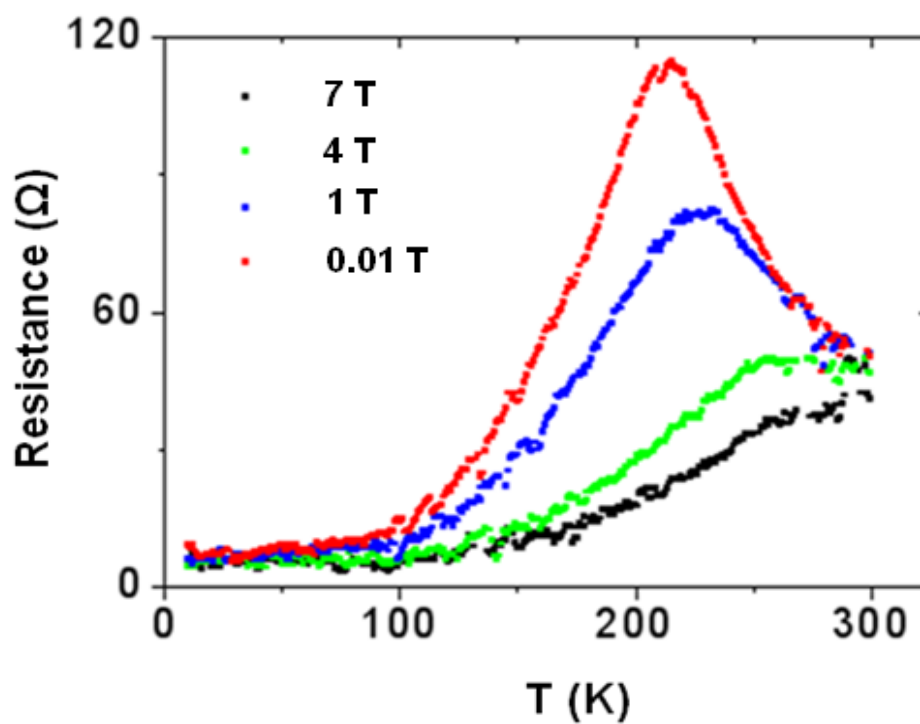


Fig. 4.23: Magnetoresistance behaviour of the LCMO films on (111) STO.

The Raman spectra of the LCMO film on (111) STO taken at different temperatures are displayed in Fig. 4.24. The R–O mode, approximately at 80 cm^{-1} , and the ω_2 , stemming from the tilting of the octahedral, are more apparent compared to the modes in the Raman spectra of LCMO films on (001) STO (cf. Fig. 4.12). These two modes become sharper and gain intensity with decreasing temperature. On the other hand, the bending modes, in the region between 400 and 500 cm^{-1} , and the JT stretching modes, roughly at 490 cm^{-1} and 605 cm^{-1} , are considerably weaker than the same modes measured for the films on (001) STO.

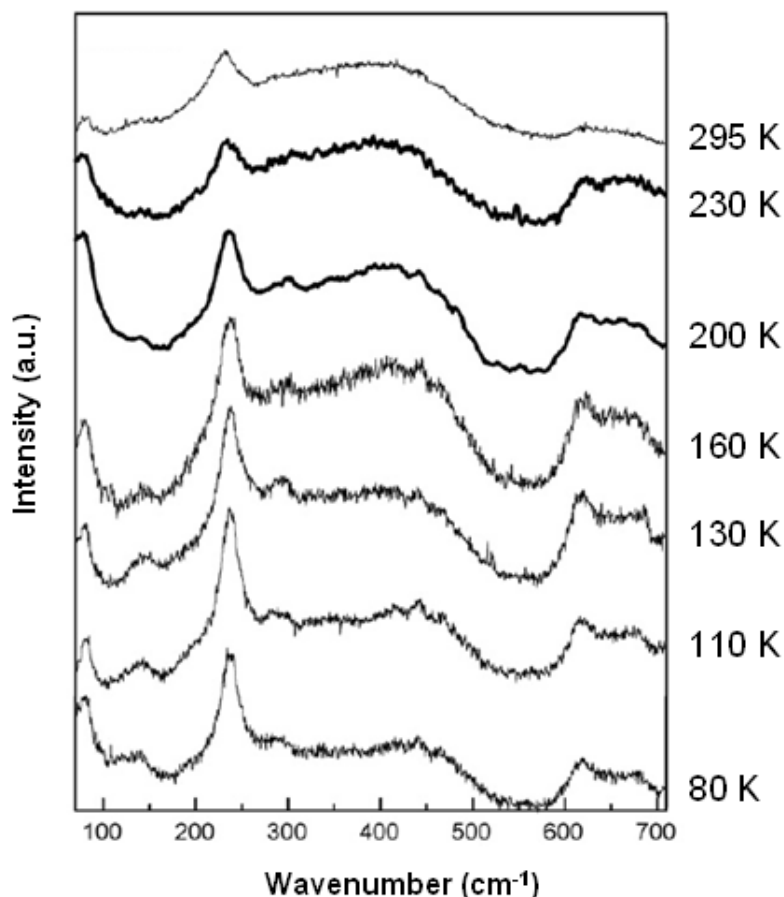


Fig. 4.24: Raman spectra of the LCMO film on (111) STO measured below room temperature. Note that the data are corrected by the thermal factor.

Measurements at different scattering polarizations are also performed at 78 K to make the symmetry assignments to all observed bands (see Fig. 4.25). The scattering configuration of each spectrum is indicated; the first symbols stand for the direction of the polarization of the incident light and the second symbols denote the polarization of the

scattered light. It should be noted that a metal-like (rhombohedral-like) spectrum [130] with sharp peaks is obtained for the cross polarization. This is consistent with resistivity measurements, which confirmed the metallic behaviour of these films, and the hypothesis that structural changes, due to strain, can cause the enhancement of double exchange mechanism and decrease of the Jahn–Teller distortion.

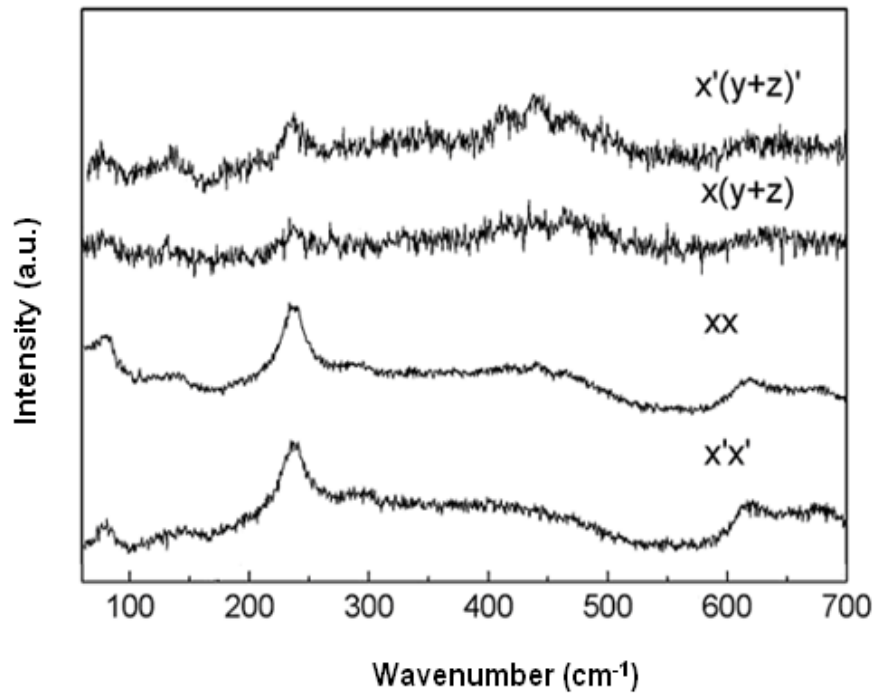


Fig. 4.25: Polarized Raman spectra measured on films on (111) STO at 78 K.

4.2.3 The LCMO films on (001) SLAO substrate

Fig. 4.26 presents the AFM images of the 40 and 290 nm thick LCMO films deposited on (001) SLAO substrates. The roughness increases with film thickness and its value varies between 1.2 and 4.6 nm for 40 and 290 nm thick films, respectively. Mean grain size area values are 2716 nm² for 40 nm films; 6735 nm² for 290 nm films. The less grain size area of films on SLAO according to films on STO can be related with the compressive mismatch strain which can prevent the increase of grain size.

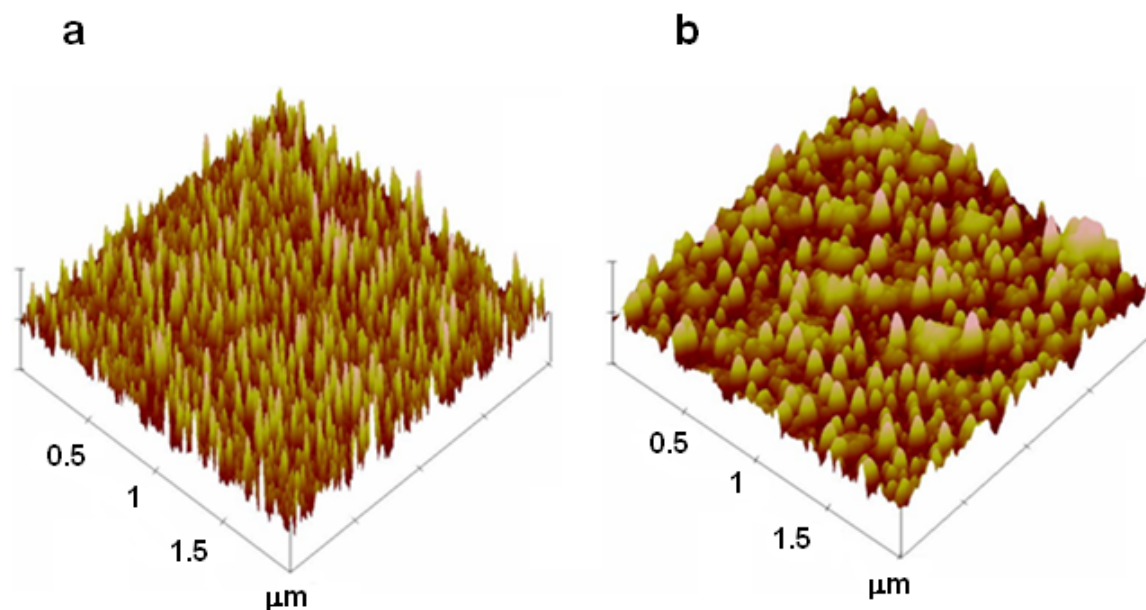


Fig. 4.26: AFM images of the (a) 40 nm and (b) 290 nm thick films on (001) SLAO.

The phase purity and the orthorhombic crystal structure are confirmed by 2θ - ω scans. It is seen in Fig. 4.27 that only $0k0$ and $00l$ reflections of the film and the substrate are visible in the diffractogram. It should be noted that LCMO reflections have rather peculiar shapes (i.e. highly asymmetric or having two maxima; cf. Fig. 4.28) which may be caused by additional reflections (e.g. $h0h$ reflection), defects and/or a stress gradients through the film thickness. The former seems to be not the case because additional peaks pertaining to this new orientation are lacking in the pole figures. The epitaxial relation between the films and the substrate and the pole figures are identical to the results obtained for the LCMO films on (001) STO (see Fig. 4.6). Therefore, a pronounced stress gradient through the thickness (possibly due to a stress relaxation effect close to the surface region) and/or a depth dependent defect (e.g. O vacancies) concentration are probably responsible from the unusual shape of the $0k0$ LCMO reflections. The lattice parameters of the films with varying thicknesses are summarized in Table 3.3. The b lattice parameter seems to contract with increasing film thickness whereas c lattice parameter has the opposite trend. Rocking curve measurements shown in Fig. 4.29 show the thinner LCMO films on (001) SLAO have a better crystallinity and FWHM increases with film thickness.

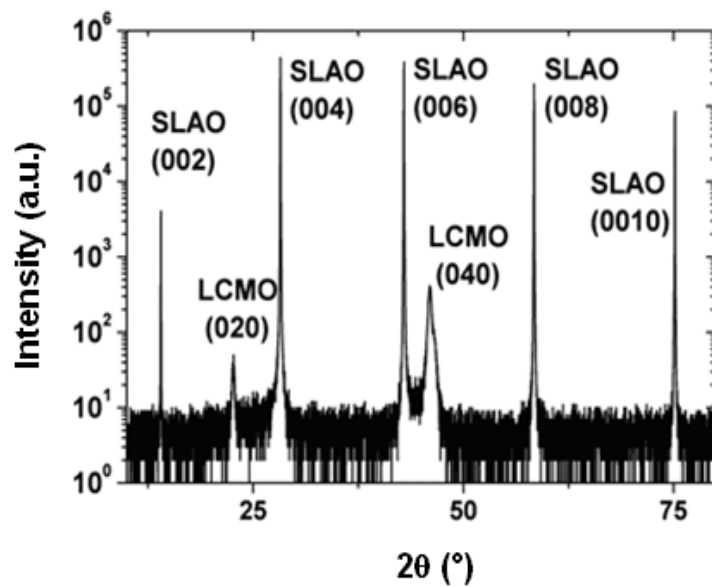


Fig. 4.27: Representative 2θ - ω scan of the LCMO films on (001) SLAO.

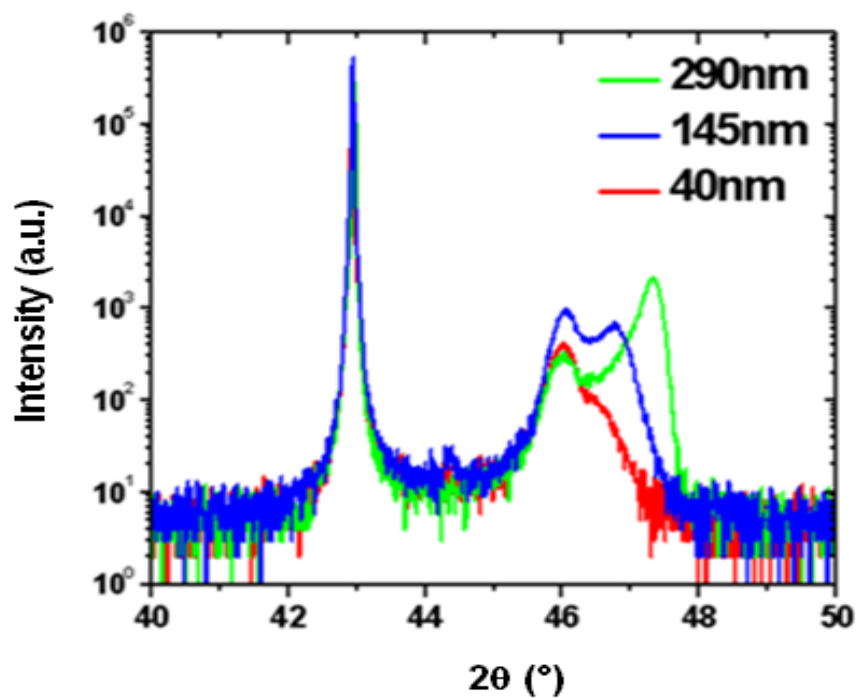


Fig. 4.28: The enlarged view of 2θ - ω scans of the LCMO films deposited on (001) SLAO around 006 substrate reflection.

Table 4.3: Lattice parameters of the LCMO films having various thicknesses and deposited on (001) SLAO.

Film Thickness (nm)	Lattice Parameter a (Å)	Lattice Parameter b (Å)	Lattice Parameter c (Å)
40	5.4454	7.9108	5.1806
80	5.3397	7.7984	4.9477
145	5.4408	7.7187	5.4069
290	5.4352	7.6791	5.4456

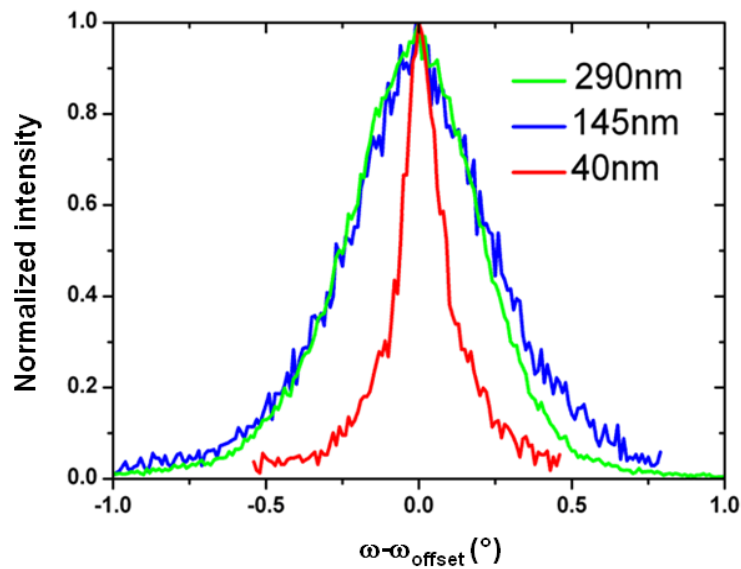


Fig. 4.29: The rocking curves measured around the 040 reflection of LCMO; the films are deposited on (001) SLAO.

The change of magnetization with temperature is shown in Fig. 4.30 for both ZFC and FC. Compared to the LCMO films on (001) STO films on SLAO substrates have

distinctly larger magnetization values. Both the magnetization per Mn ion and T_C are larger for thicker films as also valid for the LCMO films on (111) STO.

The resistivity as a function of temperature is presented in Fig. 4.31 for 40, 145 and 290 nm thick films. Resistivity increases with decreasing temperature for thinner films. Starting from the 145 nm thick film, an insulator to metal transition is observed during cooling; the transition temperature shifts from 80 to 230 K when the thickness is increased from 145 to 290 nm. As it is similar for the films on (111) STO, T_{MI} approaches to room temperature with the application of 7 T magnetic field (cf. Fig. 4.32).

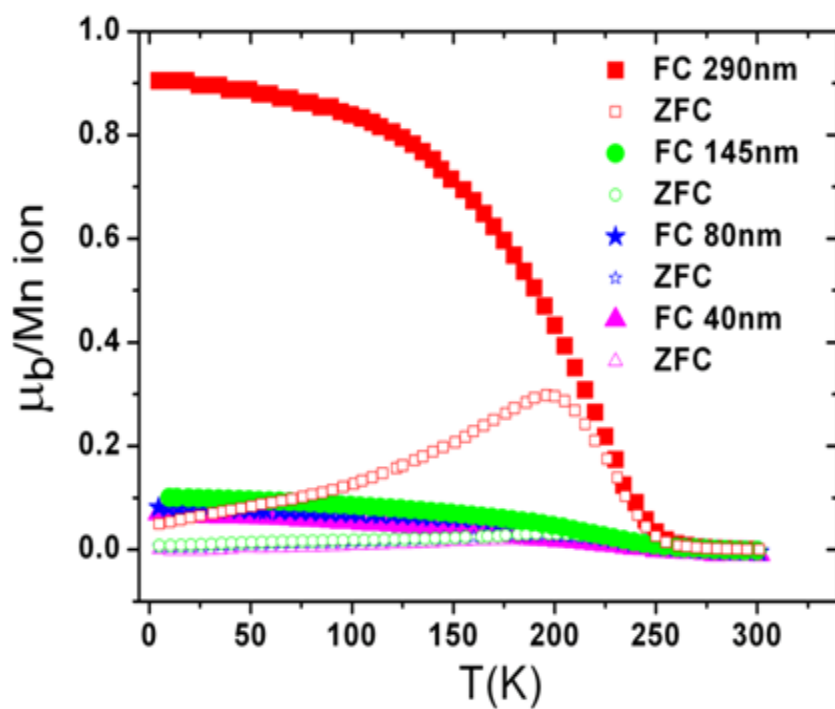


Fig. 4.30: Magnetization versus temperature graphs of LCMO films on (001) SLAO. Open symbols denote ZFC and closed symbols represent FC.

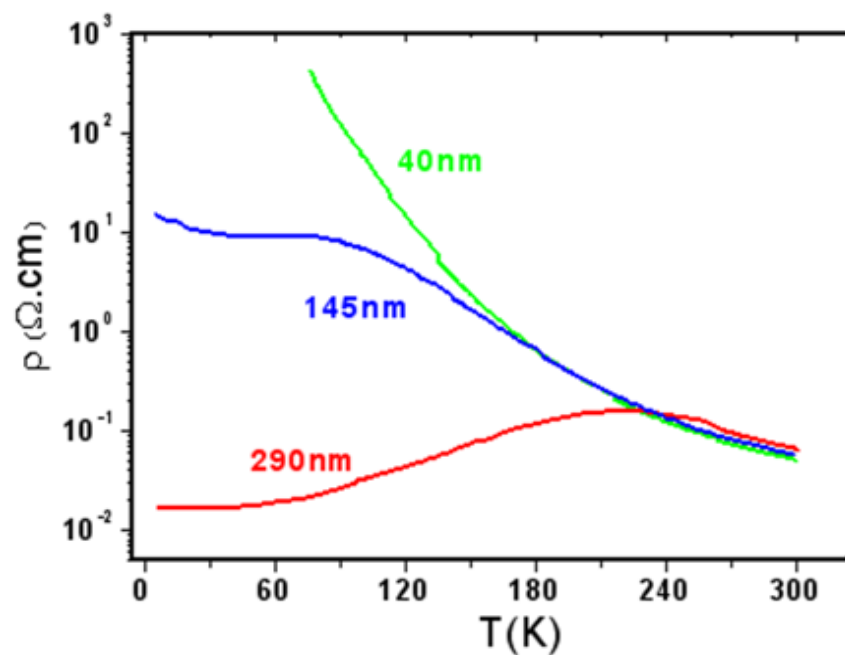


Fig. 4.31: Resistivity versus temperature plots of the LCMO films on (001) SLAO.

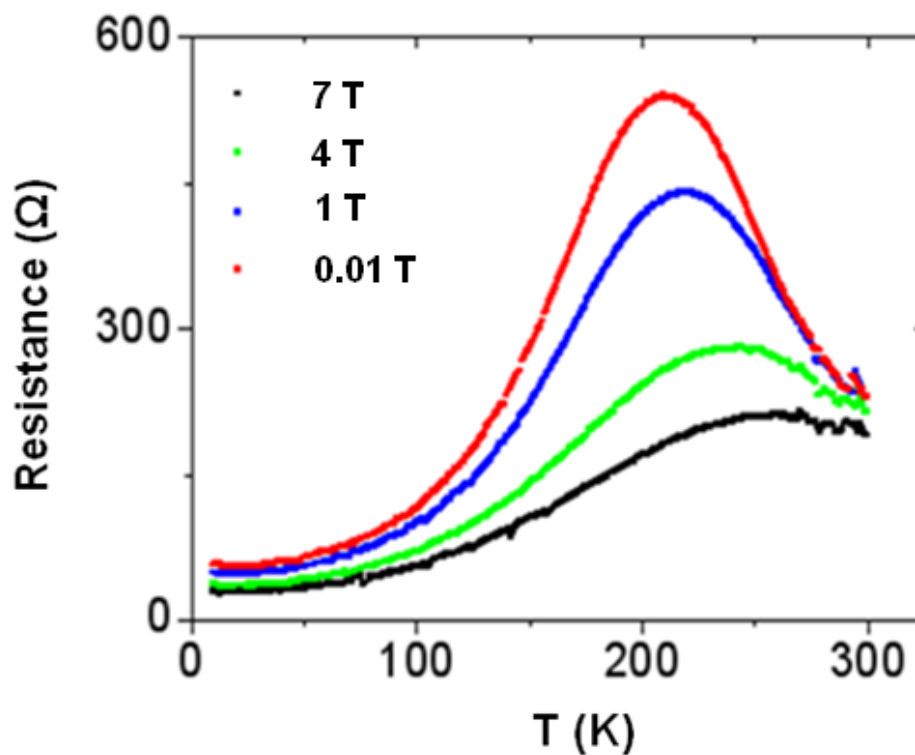


Fig. 4.32: Magnetoresistance behaviour of the LCMO films on (001) SLAO.

Fig. 4.33 shows the Raman spectra of the LCMO film deposited on (001) SLAO substrate measured at different temperatures. The R–O mode, approximately at 80 cm^{-1} , the ω_2 , stemming from the tilting of the octahedral, and $\sim 420\text{ cm}^{-1}$ bands, implying that the FM phase are constantly apparent. The bending mode around 480 cm^{-1} are visible whereas the JT stretching modes, roughly at 490 cm^{-1} and 605 cm^{-1} , are absent at all temperatures.

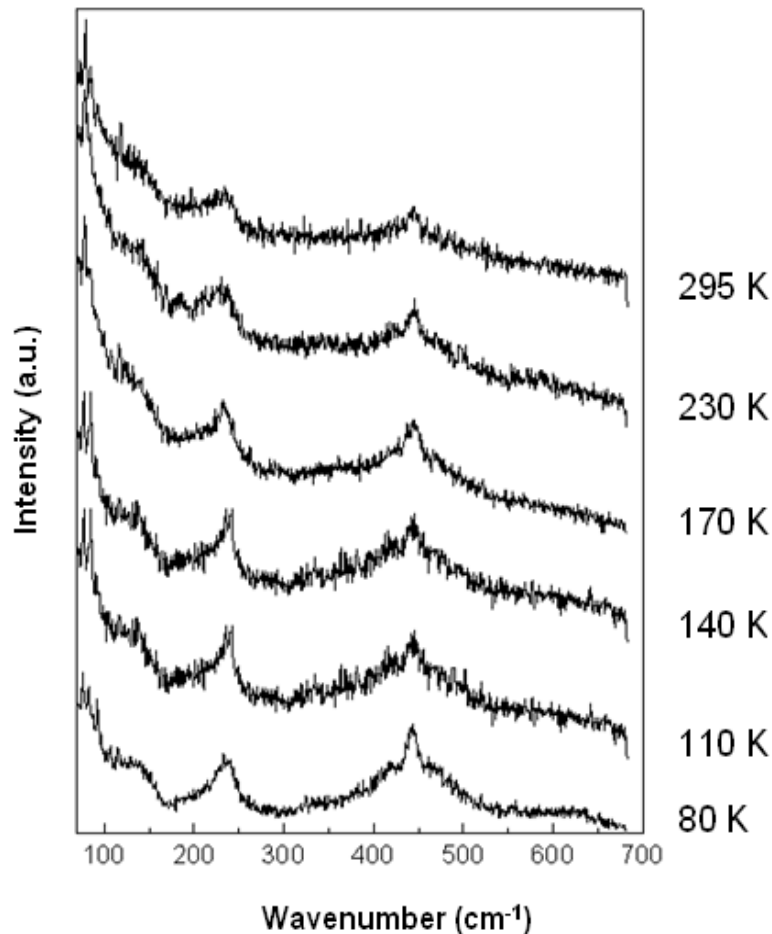


Fig. 4.33: Raman spectra of the LCMO film on (001) SLAO measured below room temperature. Note that the data are corrected by the thermal factor.

4.2.4 The LCMO films on (001) SLGO substrate

The AFM images pertaining to 40 and 290 nm thick LCMO films on (001) SLGO are shown in Fig. 4.34. The roughness values (over $4\ \mu\text{m}^2$ area) of the films are 3.1 and 6.2 nm, respectively. It should be noted that the films on (001) SLGO substrates have the roughest

surfaces among various substrates employed in this study. The differences in the roughness values between films having the same orientation but deposited on (001) SLGO, SLAO and STO substrates may be due to dissimilar atomic mobilities on these surfaces and their interface energies.

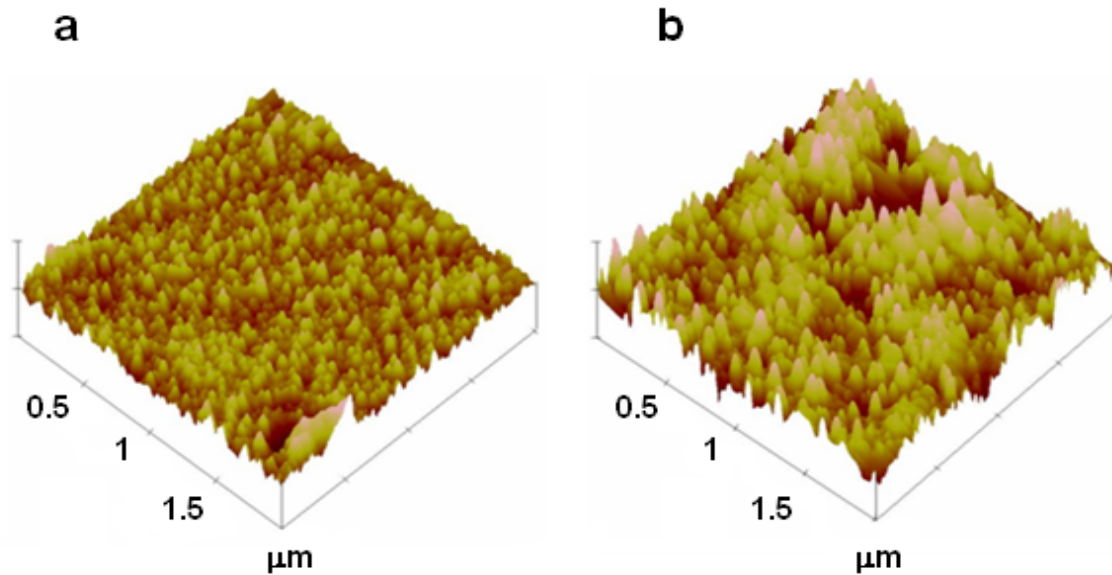


Fig. 4.34: AFM images of the (a) 40 nm and (b) 290 nm thick films on (001) SLGO.

The Fig. 4.35 shows a representative 2θ - ω scan of the LCMO films on SLGO (001) substrate. The films are single phase and have orthorhombic crystal structure. The epitaxial orientation of the films is the same as the films on (001) STO shown in Fig. 4.6. The lattice parameters of the 40, 80, 145 and 290 nm thick films, gathered in Table 4.4, are more or less similar. Contrary to the films on (001) SLAO substrate, rocking curves of the LCMO films on (001) SLGO get sharper when the film thickness increases (cf. Fig. 4.36).

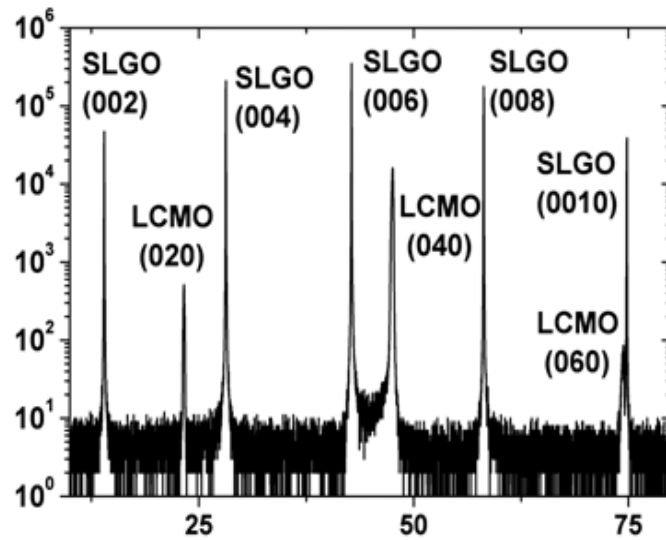


Fig. 4.35: Representative 2θ - ω scan of the LCMO films on (001) SLGO.

Table 4.4: Lattice parameters of the LCMO films having various thicknesses and deposited on (001) SLGO.

Film Thickness (nm)	Lattice Parameter a (Å)	Lattice Parameter b (Å)	Lattice Parameter c (Å)
40	5.4218	7.6371	5.4656
80	5.4259	7.6123	5.5179
145	5.4234	7.6538	5.4451
290	5.4209	7.6515	5.4420

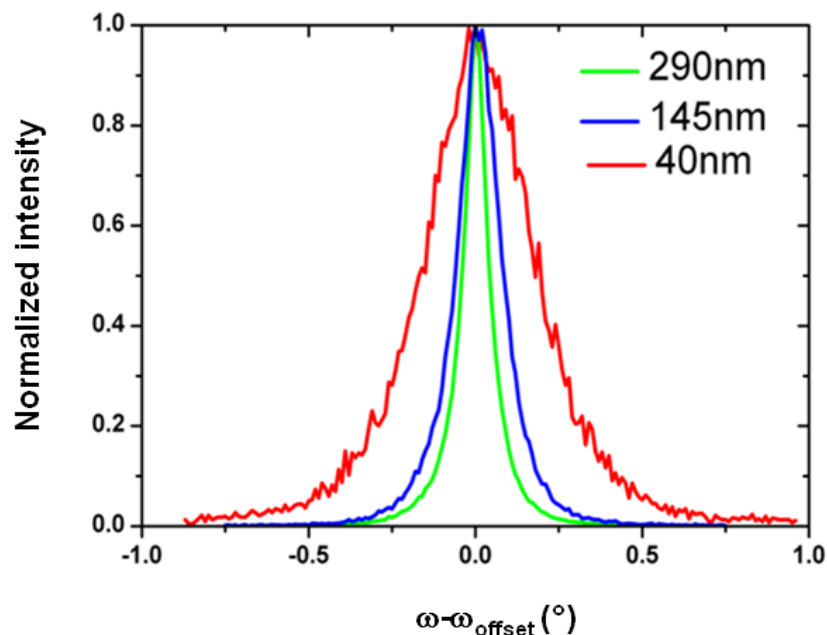


Fig. 4.36: The rocking curves measured around the 040 reflection of LCMO; the films are deposited on (001) SLGO.

The variation of magnetization with temperature in LCMO films deposited on (001) SLGO is presented in Fig. 4.37. All films have high saturation magnetization values (i.e. the highest values among the LCMO films on all substrates used in the present study) and the Curie temperatures vary between 250 and 300 K.

The dependence of resistivity on temperature (see Fig. 4.38) is also in line with the magnetization measurements mentioned above. A broad insulator to metal transition is observed at low temperatures for all thicknesses. In addition, the resistance decreases when a magnetic field is applied, similar to the behaviour observed for LCMO films on (111) STO, (001) STO and (001) SLAO, and, T_{MI} shifts to higher temperatures (cf. Fig. 4.39).

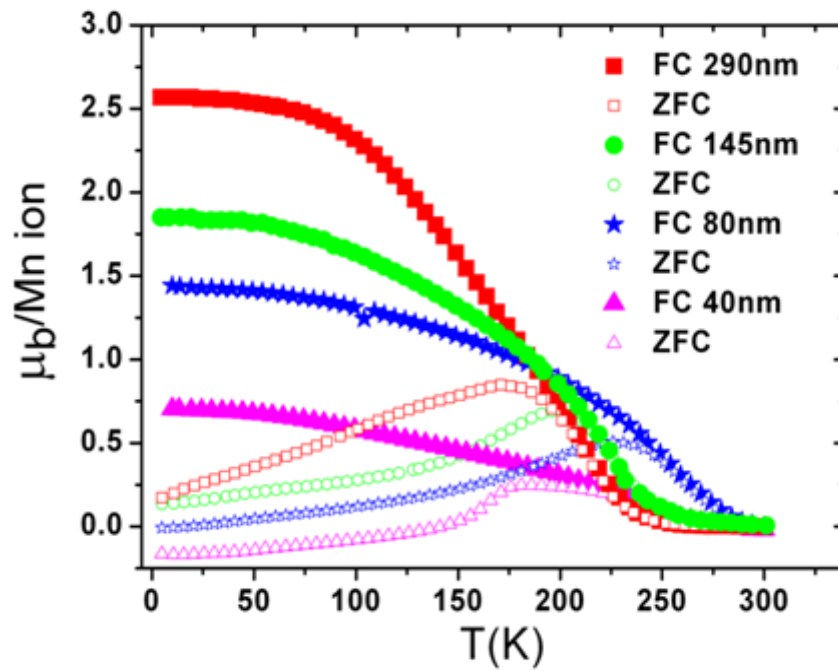


Fig. 4.37: Magnetization versus temperature graphs of LCMO films on (001) SLGO. Open symbols denote ZFC and closed symbols represent FC.

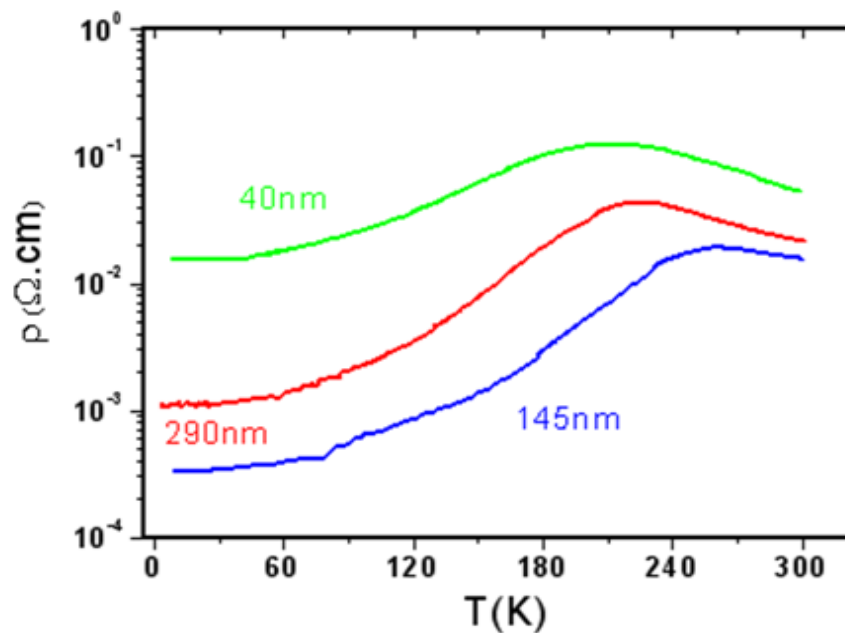


Fig. 4.38: Resistivity versus temperature plots of the LCMO films on (001) SLGO.

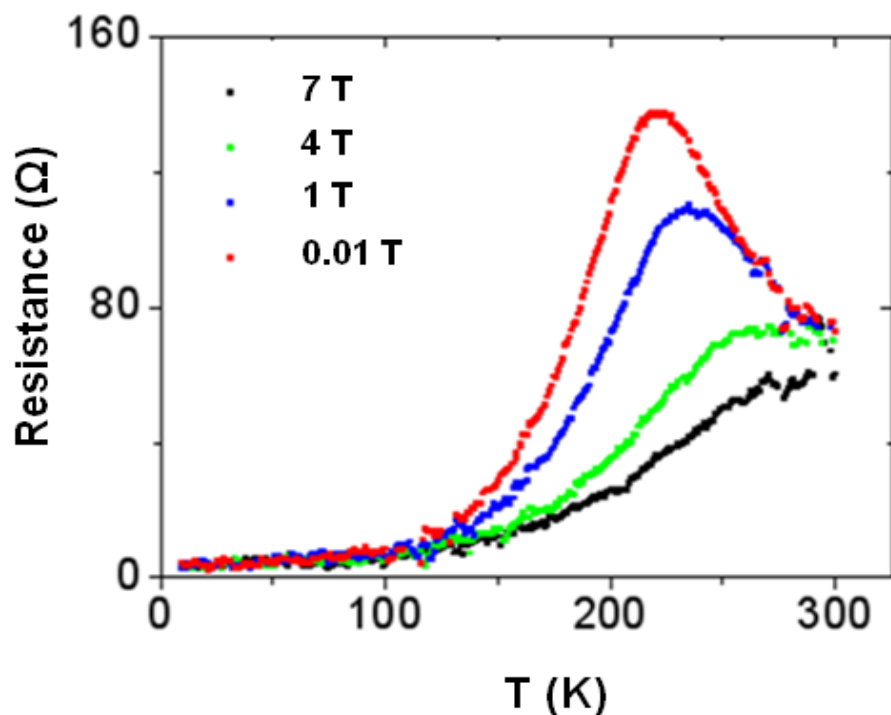


Fig. 4.39: Magnetoresistance behaviour of the LCMO films on (001) SLGO.

Fig. 4.40 shows the Raman spectra of the LCMO film deposited on (001) SLGO substrate taken at various temperatures. The modes at 80 and 230 cm^{-1} (R-O and ω_2) are quite apparent; the ω_2 mode shifts slightly to higher wavenumbers at lower temperatures. The three bending modes between 400 and 500 cm^{-1} are clearly seen even at room temperature and they gain intensity during cooling. The JT stretching modes are only distinguishable at 110 and 80 K.

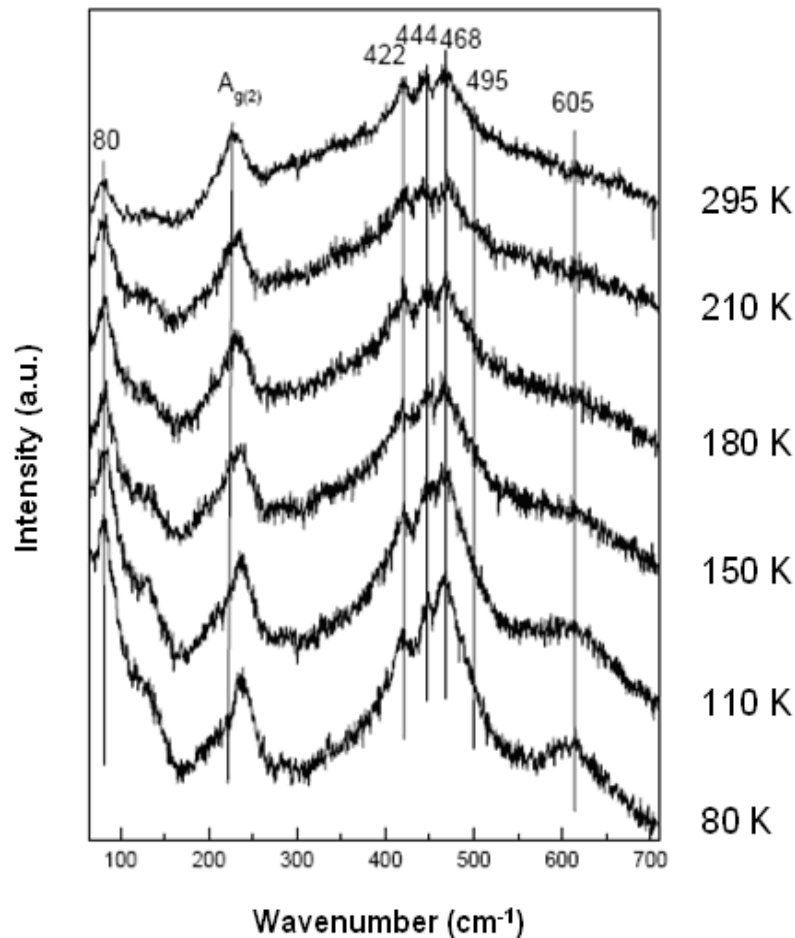


Fig. 4.40: Raman spectra of the LCMO film on (001) SLGO measured below room temperature. Note that the data are corrected by the thermal factor.

4.3 The oxygen stoichiometry of LCMO films and its effect on structural and magnetic properties

The average Mn valency and its depth dependence in the LCMO films on (001) STO and SLAO (imposing tensile and compressive epitaxial strain, respectively) are estimated from the Mn 3s exchange splitting by surface-sensitive and element-specific AR-XPS measurements (see Fig. 4.41 and Section 3.4). The film thickness is selected as 5 nm to receive signal from the whole film thickness.

The exchange splitting as a function of incidence angle is shown in Fig. 4.42 with a graph, taken from Ref. 135, illustrating the linear relationship between the exchange splitting

and the Mn valency. It is seen that the average Mn valency is smaller than the expected value 3.5 for both films. This can be due to a certain amount of O vacancies available in the as-deposited LCMO films. In addition, there is pronounced depth dependence of Mn valency for the film on (001) SLAO substrate; the valency of Mn is smaller in the surface region than the value measured for the region close to film-substrate interface. Finally, it should be noted that the average Mn valency is greater for the LCMO films on (001) SLAO substrate.

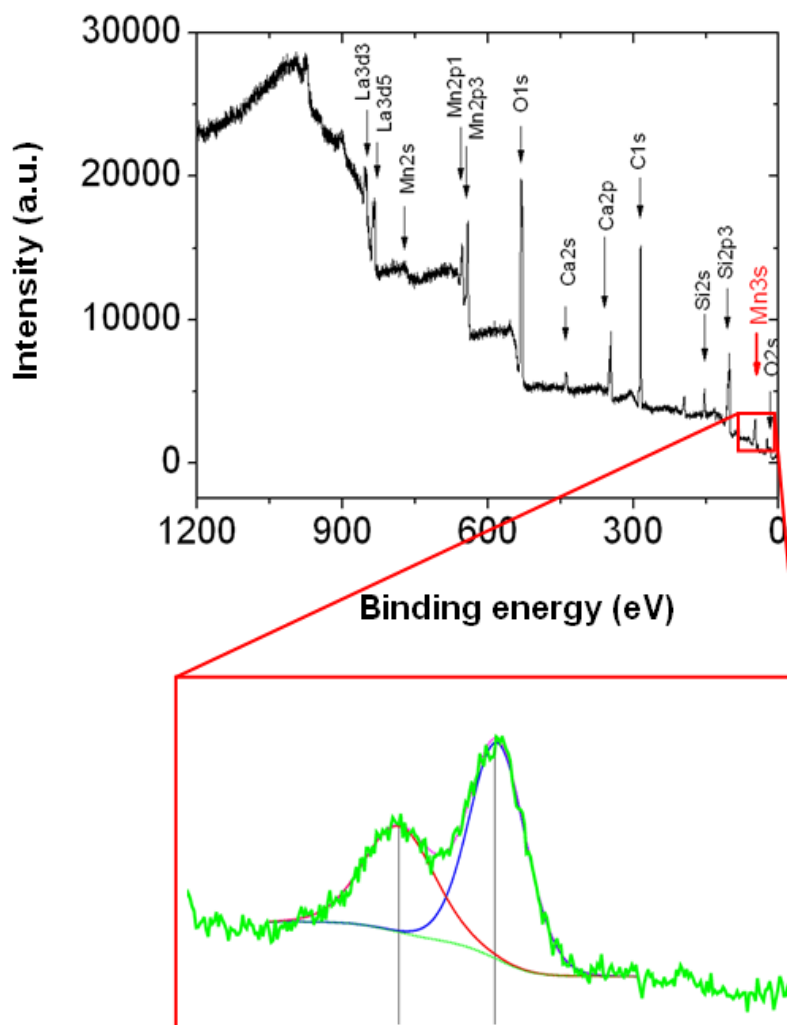


Fig. 4.41: XPS spectrum of an LCMO film and the enlarged view of the Mn 3s region.

The LCMO films deposited on (001) STO are post annealed in the vacuum and O_2 environments in order to understand the effect of oxygen stoichiometry on structural and magnetic properties.

XRD patterns of the as-deposited, vacuum annealed (at 773 K for 1 h) and, afterwards, O₂ annealed (at 1223 K for 1 h) 80 nm thick LCMO film on (001) STO are shown in Fig. 4.43. It follows that the 040 reflection of the film shifts to lower 2θ values, representing an increase in the out-of-plane lattice parameter, during vacuum annealing. The expansion of the out-of-plane lattice parameter is presumably caused by the increase in the concentration of O vacancies since two Mn⁴⁺ ions should be converted to Mn³⁺, which has a larger ionic size than the former, to satisfy the charge neutrality in the lattice. On the other hand, the 040 reflection of LCMO returns close to its initial position in the as-deposited condition after the O₂ annealing.

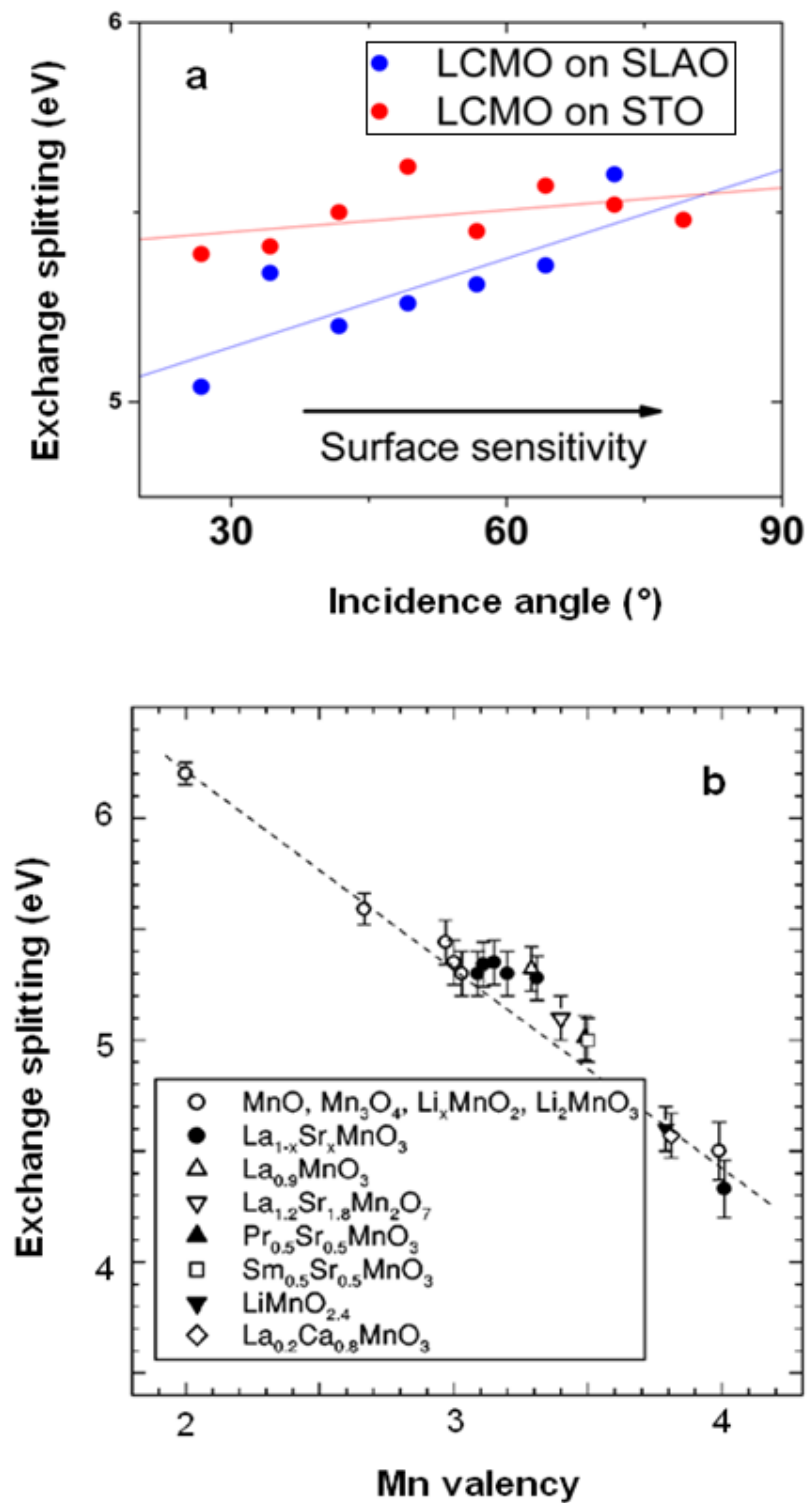


Fig. 4.42: (a) Plot of the Mn 3s exchange splitting energy versus the incidence angle and (b) the linear relationship between exchange splitting and Mn valency [135].

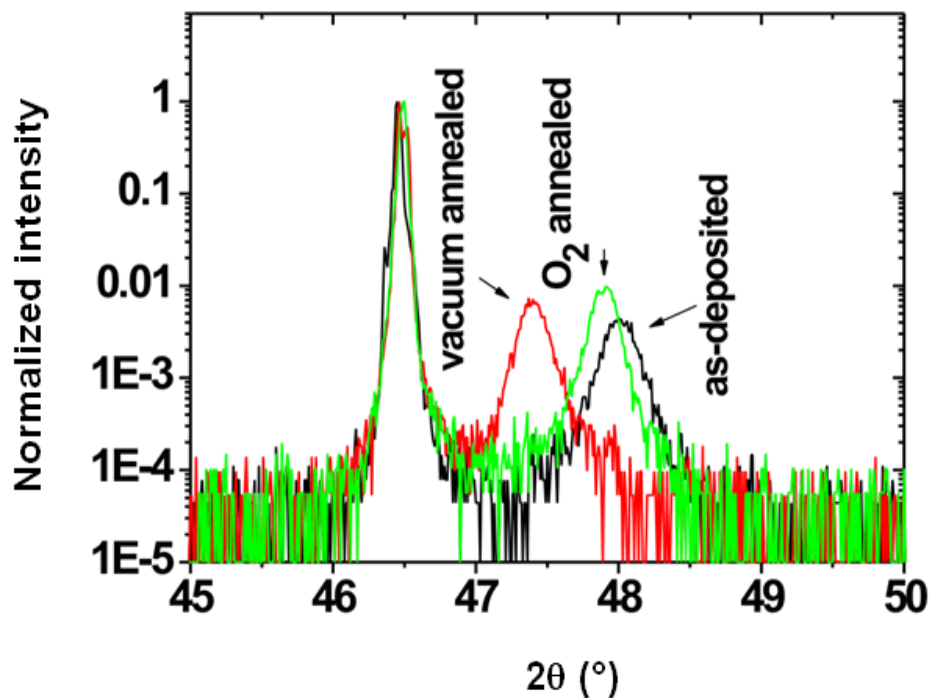


Fig. 4.43: The 040 reflection of the LCMO film deposited on (001) STO in as-deposited condition, after vacuum annealing at 773 K for 1 h and after O₂ annealing at 1223 K for 1 h.

The magnetization measurements of the 80 nm thick LCMO film on (001) STO in the as-deposited state and after heat treatments are presented in Fig. 4.44. It is clear that the magnetic moment of the film is significantly reduced by vacuum annealing whereas it can even exceed the value measured for the as-deposited film after a second heat treatment in O₂ environment. In addition, T_C decreases to approximately 140 K from 250 K (for the as-deposited state) after vacuum annealing, and then it almost recovers 240 K with O₂ annealing. It should also be here noted that O₂ annealing at 773 K for 1 h is not sufficient to recover the magnetic moment and, also, to shift the 040 reflection of LCMO peak back to its original position. This observation can be related to the slower kinetics of O-inward diffusion to the LCMO lattice than the outward diffusion from the film, in line with the data reported in Ref. [71].

In addition, Fig. 4.44 provides information about the relative importance of two parameters, namely, O stoichiometry and epitaxial strain. It follows that the largest magnetic moment that can be achieved by O₂ annealing at temperatures as high as 1223 K is far surpassed by the as-deposited film on SLAO substrate.

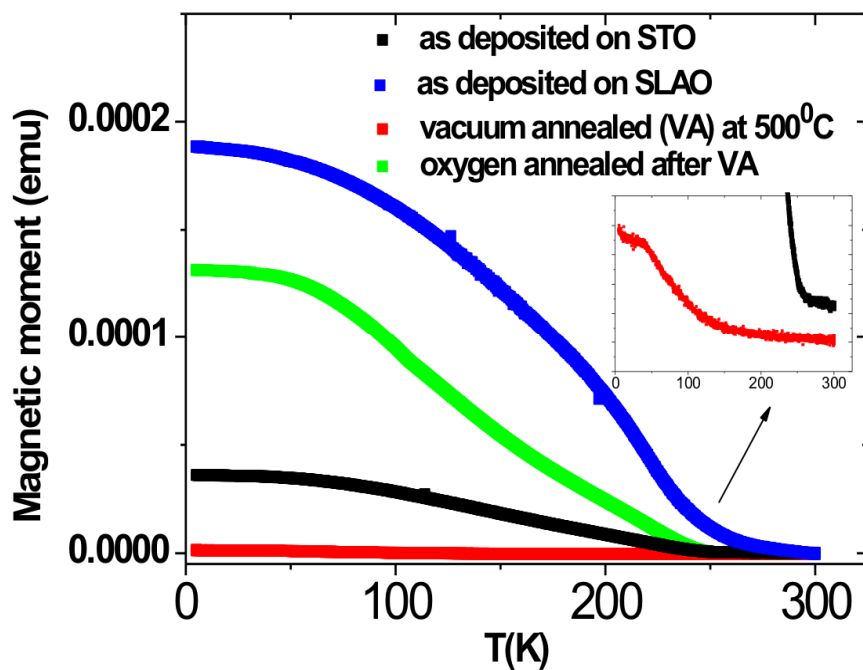


Fig. 4.44: The magnetic moment as a function of temperature for the LCMO film deposited on (001) STO in the as-deposited condition, after vacuum annealing at 773 K for 1 h and after O₂ annealing at 1223 K for 1 h. The data measured for the as-deposited LCMO film on (001) SLAO substrate are also included.

Chapter 5

Discussion

5.1 The effect of strain on the properties of LCMO films

The results presented in Chapter 4 indicate that it is possible to tune the properties of LCMO thin films between two states namely a FM metal and a CO-AFM insulator by only using different substrates and varying the film thickness. In the following subsections (i.e. Sections 5.1.1 and 5.1.2) results regarding this observation are elaborated and some possible explanations are proposed.

5.1.1 The LCMO films on (001) and (111) STO substrates

As mentioned in Sections 4.2.1 and 4.2.2 the LCMO films deposited on (111) STO show strong ferromagnetic behaviour (cf. Figs. 4.19 and 4.20) whereas the films deposited on (001) STO have very low magnetization values (cf. Figs. 4.8 and 4.9) although the film thicknesses and compositions are same in both cases. The transport measurements also support the trend in magnetic properties. The films on (001) STO are insulators between 5 and 300 K for all thicknesses (cf. Fig. 4.10). On the other hand, metallic behaviour is seen below a certain temperature for the films on (111) STO if the film thickness is larger than 145 nm (see Fig. 4.22).

The possible reasons behind this interesting result may be due to the differences in (i) the sign and/or the magnitude of the epitaxial strains, (ii) the epitaxial orientations, related to a possible anisotropy in the magnetic and electronic properties of LCMO, and (iii) the microstructures of the films on (001) and (111) STO substrates. It is known that both substrates apply approximately 2 % tensile in-plane strain (see Table 2.1) and the intrinsic magnetoanisotropy of LCMO with a slightly distorted cubic structure is negligible [134]. Therefore, (i) and (ii) can be ruled out. It is noted that a distortion of the lattice (a and c lattice parameters increase while b decreases) occurs below T_N , for the case of bulk LCMO. A similar distortion is also produced due to the epitaxial strain imposed by (001) STO. However, such a distortion is suppressed by the constraint on all lattice parameters for the case of (111) STO although the epitaxial strain has tensile character. Hence, not the type (whether it is tensile or compressive) of the epitaxial strain but its orientation with respect to film unit cell may lead to the observed difference between the electronic and magnetic properties of LCMO films deposited on (001) and (111) STO.

Concerning (iii), Tables 4.1 and 4.2 indicate that the measured lattice parameters are rather dissimilar. In order to elucidate the structural variations, apical and equatorial Mn-O distances, $d_{\text{Mn-O}}$, in MnO_6 octahedra are estimated from the lattice parameters measured by XRD and the crystal structure and atomic positions of LCMO obtained from the literature [113] using the software EnCIFer [136]. It should be noted here that the fractional coordinates of the atoms in the film do not have to be the same as the fractional coordinates of the atoms in the bulk material. This assumption was made since a direct determination via diffraction profile refinement is difficult in the case of epitaxial manganite thin film due to its two-dimensional structure, strong preferred orientation and disturbance by the substrate reflections. It follows from Fig. 5.1 that the apical Mn-O distance is considerably shorter than the equatorial ones and this difference remains more or less unchanged for all films on the (001) STO substrate. However, two equatorial Mn-O distances increase and match with the apical Mn-O distance when the films on (111) STO substrate get thicker (cf. Fig. 5.2). It is clear that the ratio $d_{\text{Mn-O}}(\text{apical})/d_{\text{Mn-O}}(\text{equatorial})$, related to the distortion of MnO_6 octahedra, approaches 1 for thicker films on (111) STO. This leads to weakening of electron-phonon interaction and enhancement of metallic behavior. On the other hand, a large octahedral distortion is always present for the films on (001) STO regardless of the film thickness.

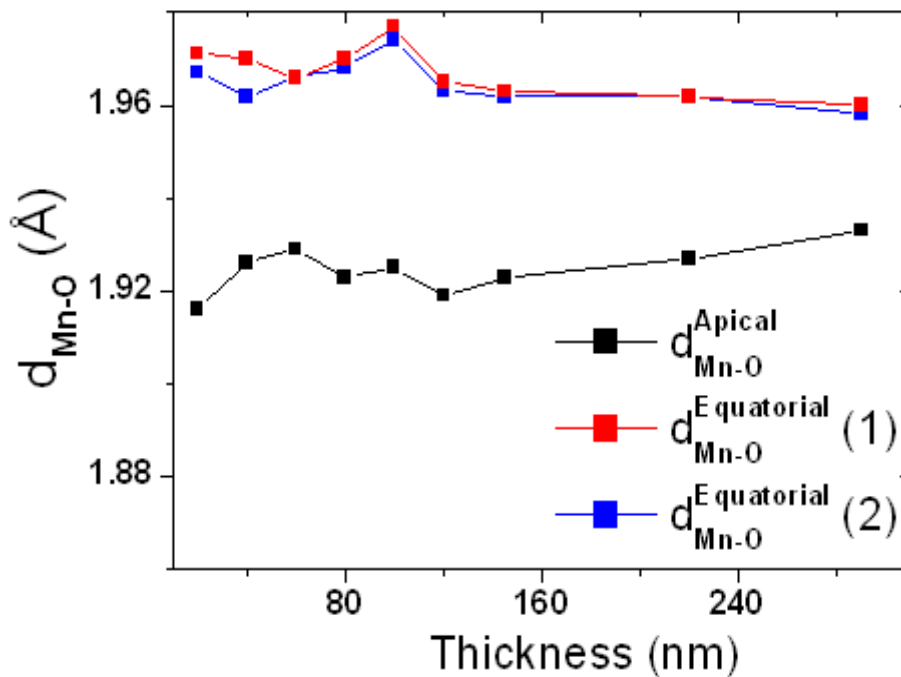


Fig. 5.1: The apical and equatorial Mn-O distances of the LCMO films deposited on (001) STO.

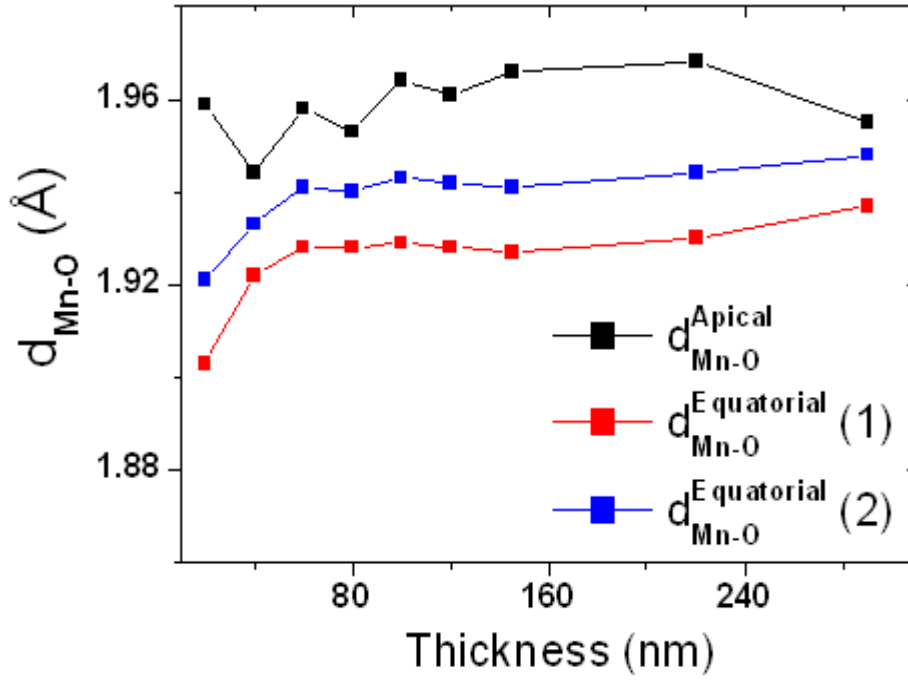


Fig. 5.2: The apical and equatorial Mn-O distances of the LCMO films deposited on (111) STO.

The Raman spectroscopy results presented in Figs. 4.12 and 4.24 indicate that JT modes are more prominent for the LCMO films deposited on (001) STO substrate.

The resistivity data are analysed in more detail according to the variable range hopping (VRH) model in order to get complementary information for the charge transport in systems where the carriers are localized. This model proposed by Mott and Davis [137] involves hopping by the polarons (electrons associated lattice deformation) to states of nearly equal energy. Such states are placed at random distances in the lattice due to the randomness in the potential. This model satisfactorily describes the polaronic transport, arising from strong electron-lattice interaction due to JT distortion, in manganites above T_C where the LCMO is in paramagnetic-insulating state [138, 139]. The change of resistivity as a function of temperature is expressed by equation (1) [137, 140] where ρ_0 is preexponential factor and T_0 is the characteristics VRH temperature. The parameter T_0 can be regarded as a measure of strength of Jahn-Teller distortion [141]. If T_0 increases, the localization length ($1/\alpha$) and average hopping distance are reduced, and resistivity increases.

$$\rho(T) = \rho_0 \exp(T_0/T)^{1/4} \quad (1)$$

Figs. 5.3 and 5.4 present the representative $\ln\rho$ versus $T^{-0.25}$ plots for the LCMO films deposited on (001) STO and (111) STO, respectively. It is found that T_0 values of the films on (001) STO are large for all thicknesses (around 10^8) whereas T_0 values of the films on (111) STO are significantly smaller and inversely proportional to the film thickness. For instance, T_0 values of the 80, 220 and 290 nm thick LCMO films on (111) STO are $1.4 \cdot 10^8$, $3.1 \cdot 10^7$ and $8.6 \cdot 10^6$ K, respectively. The T_0 values obtained from the detailed analysis of the resistivity data also support the estimated apical and equatorial Mn-O distances and Raman spectroscopy results; JT distortion is more prominent for the films on (001) STO than the ones deposited on (111) STO. It should be noted that the decrease of the octahedral distortion for the case of (111) STO can be related to the peculiar mosaic structure seen for the thicker films on (111) STO. The formation of this structure may act as a mechanism for relaxation of the distortion in the LCMO lattice.

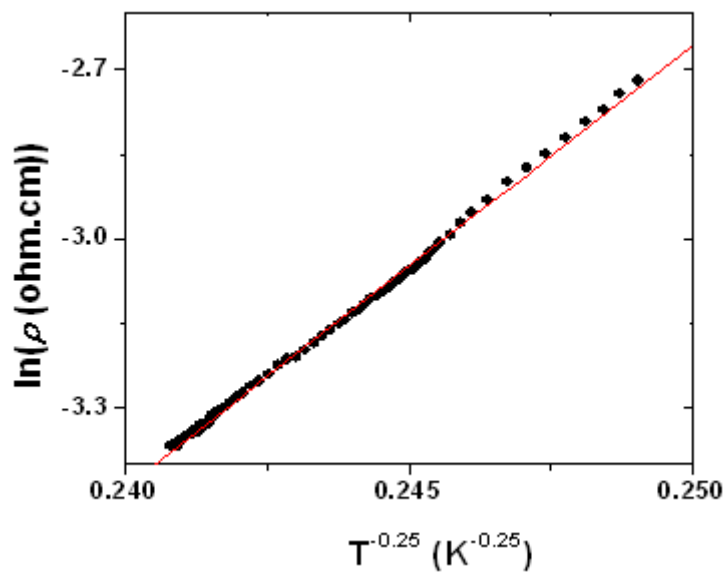


Fig. 5.3: $\ln\rho$ versus $T^{-0.25}$ plot for the 290 nm thick LCMO film deposited on (001) STO.

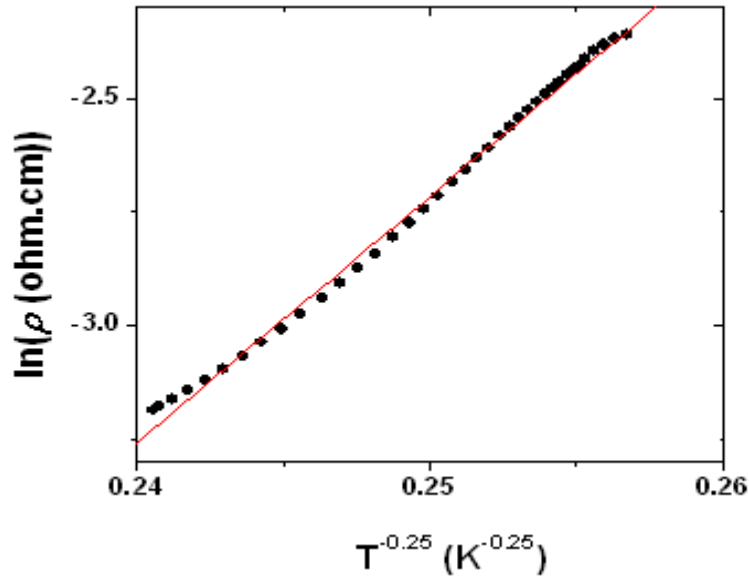


Fig. 5.4: $\ln\rho$ versus $T^{-0.25}$ plot for the 290 nm thick LCMO film deposited on (111) STO.

5.1.2 The LCMO films on (001) STO and (001) SLAO substrates

The second key observation is related to the comparison between the results presented in Sections 4.2.1 and 4.2.3. While the LCMO films on (001) STO substrate, imposing a tensile epitaxial strain, are insulators between 5 and 300 K, the films on (001) SLAO, applying a compressive epitaxial strain, show an insulator to metal transition during cooling if the film thickness is larger than 145 nm. It is noted that the compositions, the film thicknesses and the orientations of the LCMO unit cell with respect to the substrate surfaces are same in both cases.

One of the possible explanations may be the following: The compressive epitaxial strain imposed by the (001) SLAO causes a contraction of the a and c lattice parameters and a corresponding expansion of the b lattice parameter. Such a variation in the unit cell parameters is exactly reverse to the one produced by the electronic phase transition from FM metal to AFM-CO insulator below T_N . Therefore, the constraint imposed on the LCMO lattice by the (001) SLAO may act as an additional driving force for the growth of FM metallic phase whereas the formation and/or growth of the AFM-CO phase may be obstructed. However, the tensile epitaxial strain imposed by the (001) STO leads to a counter effect which favors the growth of insulating phase against the metallic one. Schematic representation of the above mentioned scenario can be seen in Fig. 5.5. The metallic phase, shown by blue color,

shrinks during cooling for the film on (001) STO. However, the amount of metallic phase increases at the expense of the insulating one, presented by yellow color, upon cooling for the film on (001) SLAO. A connection between the metallic regions occurs (i.e. percolation) at a certain temperature, denoted by T_{MI} , and the specimen as a whole acts like a metal.

A second reason may be the small octahedral distortion in the thicker LCMO films when they are deposited on (001) SLAO substrates. Fig. 5.6 presents the apical and equatorial Mn-O distances estimated from the lattice parameters of the films on (001) SLAO. It is clear that the apical Mn-O distance is distinctly larger than the equatorial ones when the film thickness is below 145 nm; resistivity increases with decreasing temperature in the entire temperature range for these films. However, the apical and equatorial Mn-O distances for the thicker films are quite similar and an insulator to metal transition is observed for these films upon cooling (cf. Fig. 4.31).

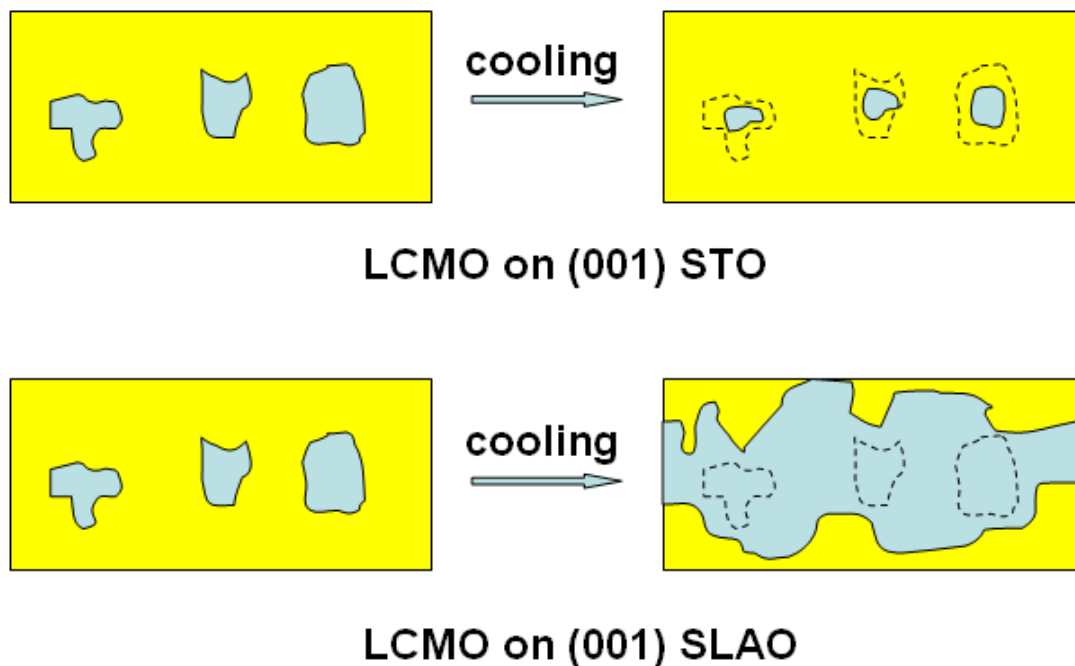


Fig. 5.5: Schematic representation of the different electronic phases in the LCMO films on (001) STO and (001) SLAO. The blue and yellow colors denote the metallic and insulating phases, respectively.

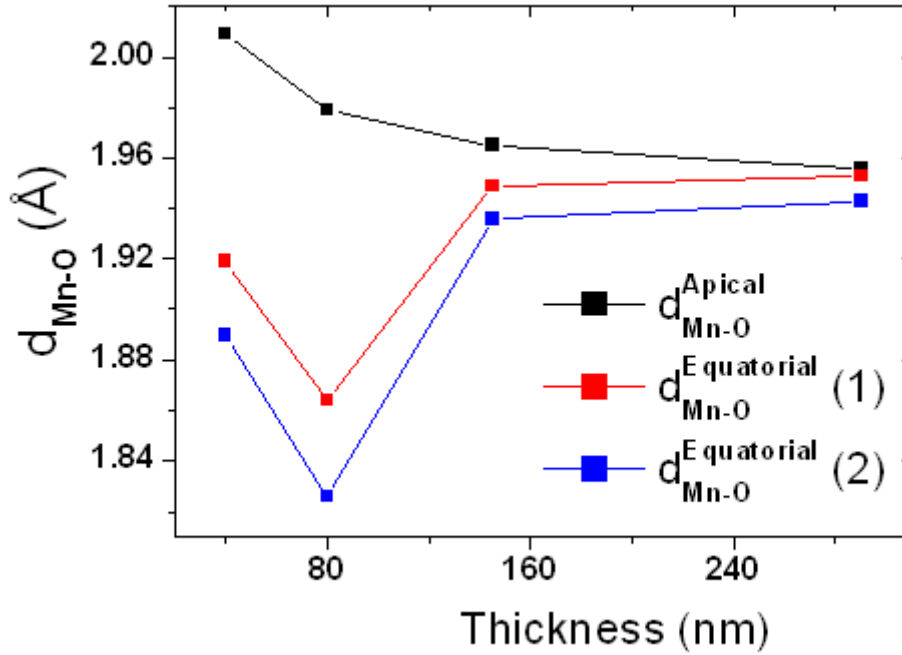


Fig. 5.6: The apical and equatorial Mn-O distances of the LCMO films deposited on (001) SLAO.

The comparison of the Raman spectra of the films on (001) STO and (001) SLAO substrates (see Fig. 5.7) supports the larger distortion of LCMO unit cell on (001) STO. The JT stretching modes, roughly at 480 cm^{-1} and 610 cm^{-1} , are much more apparent for the films on (001) STO than for the films on (001) SLAO down to 80 K.

Furthermore, the T_0 value (i.e. positively correlated with the strength of JT distortion) obtained by analyzing the resistivity data according VRH model is $1.1 \cdot 10^7$ K for the 290 nm LCMO film on (001) SLAO substrate (see Fig. 5.8). This value is approximately an order of magnitude smaller than the T_0 determined for the film on (001) STO. This observed difference in the T_0 values for the films on two different substrates is in line with the Mn-O distances and Raman spectra, predicting a smaller octahedral distortion for the LCMO films on (001) SLAO.

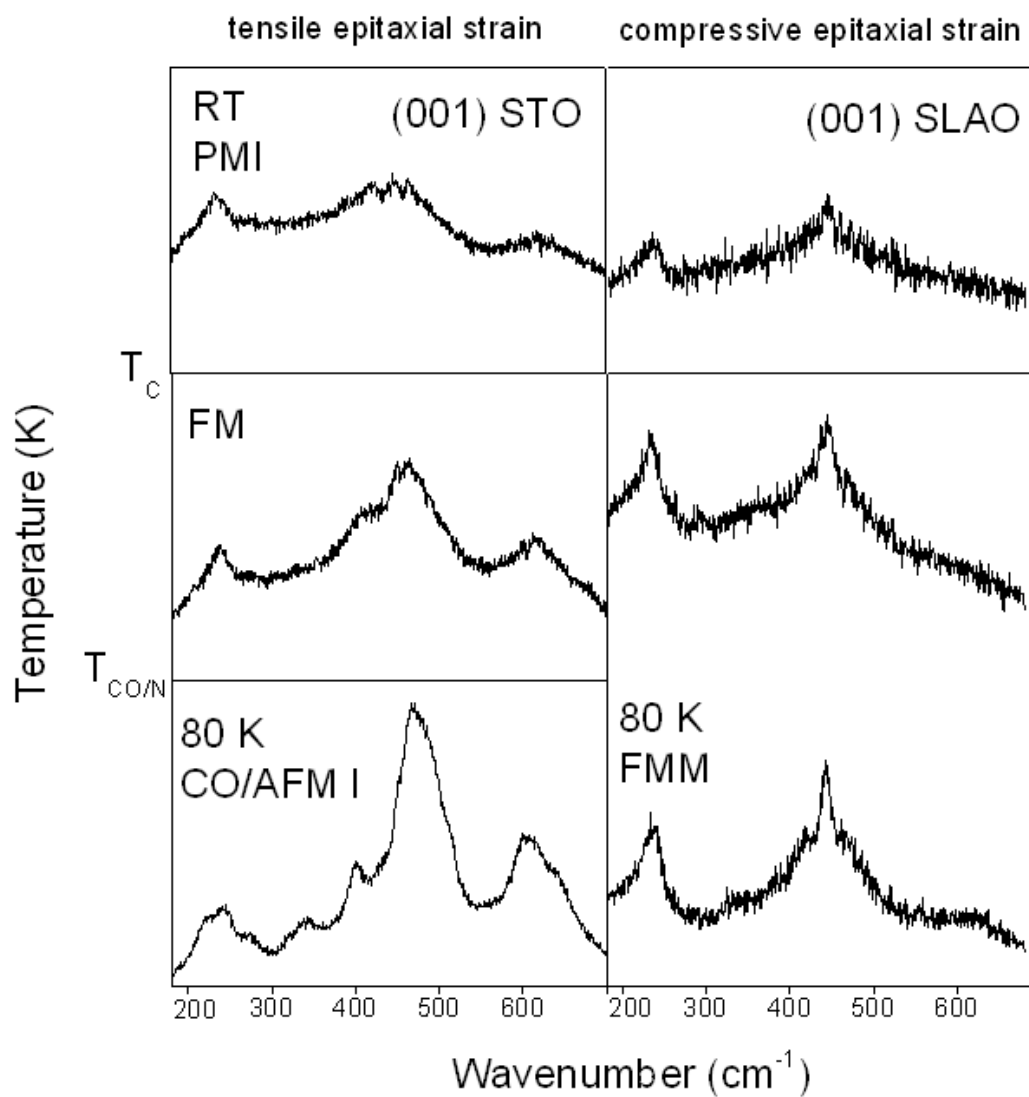


Fig. 5.7: The Raman spectra of the 290 nm thick LCMO films deposited on (001) STO and (001) SLAO substrates at certain temperatures.

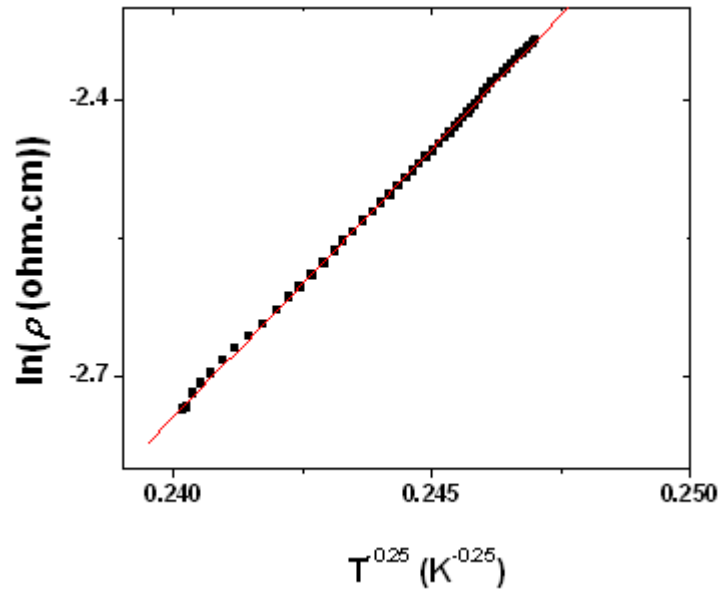


Fig. 5.8: $\ln\rho$ versus $T^{-0.25}$ plot for the 290 nm thick LCMO film deposited on (001) SLAO.

5.2 The effect of oxygen stoichiometry on the properties of LCMO films

The results presented in Section 4.3 clearly show that the O stoichiometry is of cardinal importance with respect to structural and magnetic properties of LCMO thin films. The O vacancies proposed to be present in the as-deposited state (indicated by the experimentally measured average Mn valencies of 5 nm thick films on both (001) STO and (001) SLAO; see Section 4.3) may presumably due to a surface reconstruction process. The extent of such an effect is determined by the balance between several parameters (e.g. surface energy, strain energy and defect concentration) determining the internal energy of the lattice.

It is known that two Mn^{4+} ions should be converted to Mn^{3+} , which has a larger ionic size than the former, to satisfy the charge neutrality in the lattice during creation of an O vacancy. It is conceivable that tensile epitaxial strain favors the formation of O vacancies since the tensile epitaxial strain imposed by the substrate is compensated by the compressive strain due to formation of O vacancies [142-144]. However, the situation is reverse for the compressive epitaxial strain which hinders the formation of O vacancies. It is pointed out in Section 4.3 that the valence of Mn is larger (there are less O vacancies in the lattice) for the LCMO film on (001) SLAO, which is in line with the argument stated above.

In Section 4.3 it is also reported that an increase in the magnetic moment and T_C is observed after annealing in O_2 environment while vacuum annealing works in the opposite direction. A remarkable decrease in the amount of Mn^{4+} ions compared to the amount of larger Mn^{3+} ions may increase the Jahn-Teller distortion, which weakens the double-exchange mechanism via electron-phonon interaction. This may lead to a reduction in magnetic moment and conductivity [32, 38].

Finally, Fig. 4.44 shows that the largest magnetic moment that can be achieved by O_2 annealing at temperatures as high as 1223 K is far exceeded by the as-deposited film on (001) SLAO substrate. The compressive epitaxial strain imposed by (001) SLAO can have two consequences: (i) The formation of the CO-AFM phase is hindered by the distortion caused by the in-plane contraction in the LCMO film. (ii) The compressive epitaxial strain can stabilize more O anions in the lattice, which in turn can increase the relative amount of Mn^{4+} cations and decrease the JT distortion.

Chapter 6

Conclusions

Single phase, epitaxial LCMO thin films are successfully deposited on (001) STO, (111) STO, (001) SLAO and (001) SLGO planar substrates by PLD method.

Although chemical composition, deposition conditions and thicknesses of the LCMO films are kept constant, it is possible to stabilize a wide range of phases from an AFM-CO insulator to a FM metal by employing the substrate material as a knob to tune the film properties. The magnetization values can be varied more than an order of magnitude.

The resistivity increases with decreasing temperature within the entire temperature range for the films on (001) STO and the magnetization values are rather low. The insulating behaviour is suppressed and an insulator to metal transition occurs by the application of 7 T magnetic field. An insulator to metal transition is observed upon cooling for the LCMO films on (111) STO and (001) SLAO when the film thickness reaches 145 nm. All films on (001) SLGO show insulator -to- metal transitions close to room temperature.

The metallic behaviour can be improved by using (111) STO and (001) SLAO substrates hindering the distortion accompanying to the FM to AFM phase transition in the bulk LCMO.

Not only the sign of the epitaxial strain (e.g. tensile or compressive) but also its orientation with respect to LCMO unit cell is crucial to clarify the effect of strain on electrical and magnetic properties.

It is shown via XRD, Raman spectroscopy and detailed investigation of the variation of resistivity as a function of temperature according to VRH model that all films exhibiting insulating behaviour have large octahedral distortion whereas the films with low JT distortion show metallic behaviour at low temperatures and have high magnetization values.

The decrease of the octahedral distortion may occur via some microstructural modifications such as formation of a mosaic structure close to the surface region or development of a strain gradient through the film thickness.

The oxygen stoichiometry has a strong effect on the structural, magnetic and electronic properties of LCMO thin films. It is found out that the films contain a certain amount of O vacancies even in the as-deposited state. The LCMO film on (001) STO, imposing tensile epitaxial strain have more O vacancies than the film on (001) SLAO, having smaller in-plane lattice parameter than the film.

Post-annealing treatment in vacuum, increasing the amount of O vacancies, causes a reduction in the magnetic moment of the film presumably due to decrease of the amount of Mn^{4+} cations in the lattice. On the other hand, the original values are recovered after a subsequent O_2 annealing.

The enhancement of the magnetic moment employing SLAO substrate is found to be distinctly larger than the maximum value reached by O_2 annealing at temperature as high as 1223 K for 1 hour, highlighting the importance of strain parameter for manganites.

A clear correlation between epitaxial strain, lattice distortion, oxygen stoichiometry and the electrical and magnetic properties of the LCMO films is observed for the experimental results presented in this study. However, the relevance of other mechanisms such as charge, orbital and spin ordering can not be excluded. It is possible that these processes are not independent from the distortion but somehow coupled together. Consequently, both the processes hindering the conductivity may be triggered by a distortion of the structure and distortion may be increased or decreased dependent on the result of the competition between the different mechanisms.

From the technological point of view, this study demonstrates that it is possible to tune the electronic and magnetic properties by the substrate material, thickness and O stoichiometry in order to be able to use the same material for different purposes in microelectronic applications.

Chapter 7

Summary

The doped rare earth manganites have attracted considerable attention in both bulk and thin film form due to their potential use in recording media technology and their interesting behaviour known as colossal magnetoresistance which is the drastic change in electrical resistivity by the application of a magnetic field. In addition, manganites exhibiting high electronic and ionic conductivity have the potential for new application fields such as electrode materials in solid oxide fuel cells.

Manganites of the type $\text{La}_{1-x}\text{Ca}_x\text{MnO}_3$ have a rich phase diagram due to a delicate balance between several mechanisms such as charge, orbital and spin ordering superimposed to lattice effect. The observed electronic phases and, in turn, the properties are very sensitive to external perturbations such as high magnetic fields and epitaxial strain. The aim of this work is to prepare epitaxially grown single phase thin films and to show the possibility of tuning the dominant electronic phase between an antiferromagnetic insulator and a ferromagnetic metal via the epitaxial strain imposed by the substrate and demonstrating the significance of oxygen stoichiometry (i.e. varied by vacuum or O_2 annealings) in terms of the eventual electronic and magnetic state. The composition at the boundary between the charge ordered antiferromagnetic and the ferromagnetic phases in the phase diagram of bulk material (i.e. $\text{La}_{0.5}\text{Ca}_{0.5}\text{MnO}_3$ -LCMO-) has been selected for the experiments.

The films of various thicknesses are deposited systematically by the pulsed laser deposition technique (PLD) which is one of the most convenient methods to produce epitaxial multi-component oxide thin films with very low defect density. This method yields one-to-one composition transfer from target to the surface of the substrate. An excimer laser with KrF gas mixture emitting ultra-violet radiation having a wavelength of 248 nm is employed in the PLD system during the deposition of the films. Laser fluence and pulse frequency are fixed to 1.6 J/cm^2 and 5 Hz, respectively. The films are deposited at 1073 K with an oxygen pressure of 0.4 mbar. Following the deposition, films are annealed at 1173 K for 30 minutes in ambient oxygen pressure.

The detailed characterization of the structural, electrical and magnetic properties of the films is carried out by X-ray diffraction (XRD), atomic force microscopy (AFM), transmission electron microscopy (TEM), X-ray photoelectron spectroscopy (XPS), Raman spectroscopy, resistivity and magnetization measurements.

7.1 The effect of epitaxial strain

The substrate material is a crucial parameter determining the microstructure and, in turn, the eventual physical and chemical properties of thin films. In order to deposit epitaxial thin films with low defect concentration, the in-plane lattice mismatch between the film and the substrate should be small and their coefficients of thermal expansion should be similar. Moreover, the substrate material should be stable both chemically and mechanically between the deposition temperature and the ambient temperature. Apart from these basic requirements, a substrate can be employed as a functional tool to modify the properties of the thin film via the epitaxial strain. In the present study, planar (001), (111) SrTiO₃ (STO), (001) SrLaGaO₄ (SLGO) and (001) SrLaAlO₄ (SLAO) substrates are used to investigate the influence of epitaxial strain on electrical and magnetic behavior of the LCMO thin films. The former three substrates impose tensile epitaxial strain whereas the in-plane lattice parameter of the SLAO is smaller than the one pertaining to the LCMO film and, therefore, it applies a compressive epitaxial strain. The use of different thicknesses provides the opportunity to study the influence of partial relaxation of the strain.

X-ray 2θ - ω scans show that all samples are single phase and have orthorhombic crystal structure. According to {121} pole figures, the films deposited on (001) STO, SLAO, SLGO display a four-fold symmetry whereas three-fold symmetry is observed for the films deposited on (111) STO substrates (cf. Chapter 4).

Fig. 7.1 shows that the resistivity increases with decreasing temperature within the temperature range between 300 and 4 K for the films on (001) STO. In addition, the magnetization values of these films are rather low (cf. Chapter 4). It is seen in Figs. 7.2 and 7.3 that a metallic behaviour is achieved by using (001) SLAO and (111) STO substrates. A possible explanation may be the following: The compressive epitaxial strain imposed by the (001) SLAO causes a contraction of the a and c (i.e. in-plane) lattice parameters and a corresponding expansion of the b (i.e. out-of-plane) lattice parameter. Such a variation in the unit cell parameters is exactly reverse of the one produced by the electronic phase transition from ferromagnetic metallic phase to charge ordered antiferromagnetic state. Therefore, the constraint imposed on the LCMO lattice by the (001) SLAO substrate may act as an additional driving force for the growth of ferromagnetic metallic phase whereas the formation and/or growth of the charge ordered antiferromagnetic phase may be obstructed. The (111) STO causes also a similar effect since three edges of the LCMO unit cell are directly clamped by the substrate due to the orientation of the tensile epitaxial strain with respect to the LCMO unit cell, which also can prevent the formation of the antiferromagnetic insulating phase (cf.

Chapters 4 and 5). However, the tensile epitaxial strain imposed by the (001) STO leads to an opposite effect which favors the growth of insulating phase against the metallic one. Schematic representation of the above mentioned scenario is shown in Fig. 7.4. The metallic phase, shown by blue color, shrinks during cooling for the film on (001) STO. However, the amount of metallic phase increases at the expense of the insulating one, presented by yellow color, upon cooling for the films on (001) SLAO and (111) STO. A connection between the metallic regions occurs (i.e. percolation) at a certain temperature, denoted by T_{MI} , and the specimen as a whole acts like a metal.

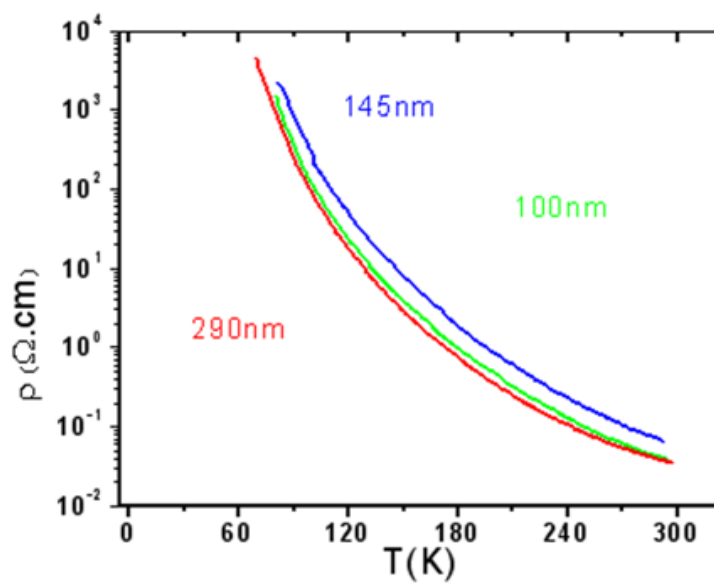


Fig. 7.1: Resistivity versus temperature plots of the LCMO films on (001) STO.

The LCMO films on (111) STO and (001) SLAO substrates have quite low room temperature octahedral distortions, evidenced by XRD, Raman spectroscopy and resistivity measurements (see Chapter 4). The reduced distortion leads to a weaker electron-phonon interaction, therefore, a higher conductivity and, in turn, higher magnetic moments according to the double-exchange mechanism.

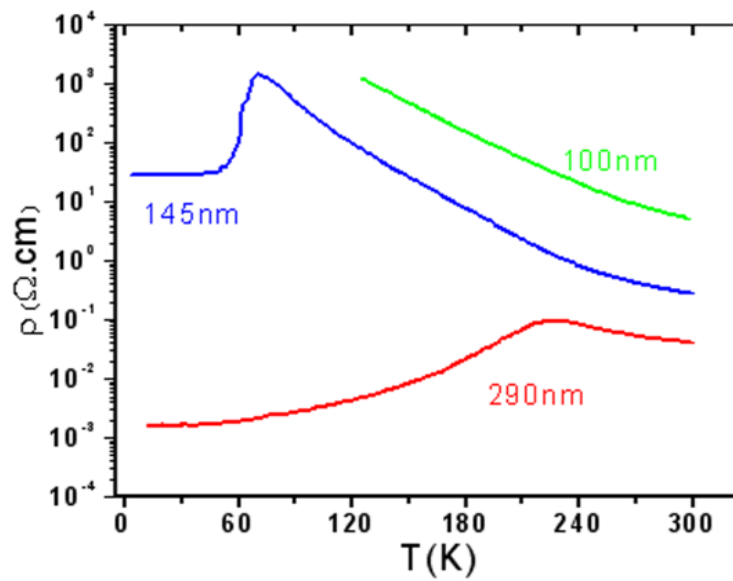


Fig. 7.2: Resistivity versus temperature plots of the LCMO films on (111) STO.

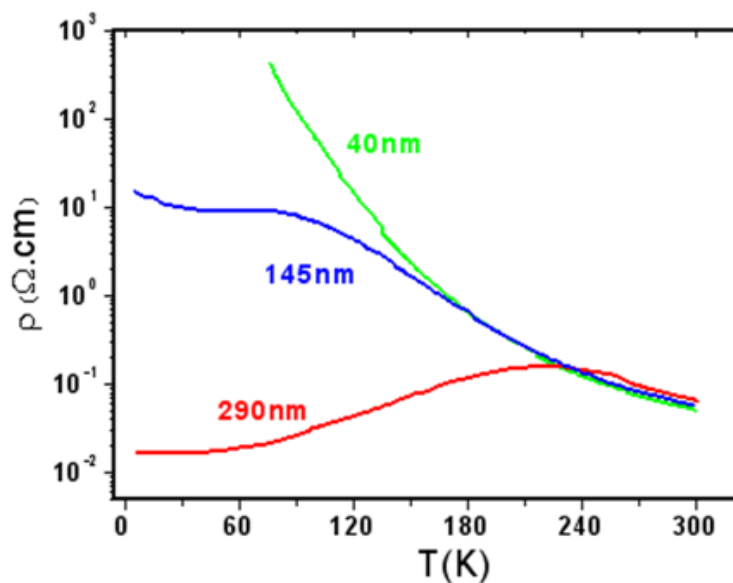


Fig. 7.3: Resistivity versus temperature plots of the LCMO films on (001) SLAO.

These results underline the fact that it is possible to stabilize a wide range of phases via the substrate material used as a knob to tune the film properties. The electrical and magnetic properties depend strongly on the film thickness since the epitaxial strain applied by

the substrate relaxes for the relatively thick LCMO films. Besides, the comparison of Figs. 7.1. and 7.2 suggests that not only the sign of the epitaxial strain (e.g. tensile or compressive) but also its orientation with respect to LCMO unit cell is critical for the ultimate electrical and magnetic properties (both STO (001) and STO (111) substrates induce tensile in-plane epitaxial strain; cf. Chapters 2 and 4).

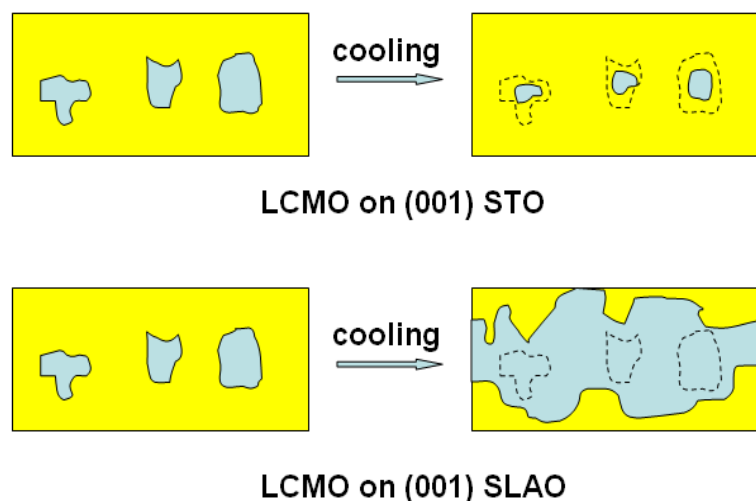


Fig. 7.4: Schematic representation of the different electronic phases in the LCMO films on (001) STO and (001) SLAO. The blue and yellow colors denote the metallic and insulating phases, respectively.

7.2 The effect of oxygen stoichiometry

In order to understand the effect of oxygen stoichiometry on the structural, electronic and magnetic properties of LCMO films, they are post annealed in vacuum and under constant oxygen flow.

XRD patterns of the as-deposited, vacuum-annealed (at 773 K) and, afterwards, O_2 -annealed (at 1223 K) LCMO films (thickness of the film is 80 nm) on (001) STO are seen in Fig. 7.5. It follows that the 040 reflection of the film shifts to lower 2θ values, representing an increase in the out-of-plane lattice parameter, during vacuum annealing. The expansion of the out-of-plane lattice parameter is presumably caused by the increase in the concentration of O vacancies since two Mn^{4+} ions should be converted to Mn^{3+} , which has a larger ionic size than the former, to satisfy charge neutrality in the lattice. On the other hand, the 040 reflection of

LCMO returns close to its initial position in the as-deposited condition after the consecutive O₂ annealing.

The variation of magnetization with temperature for the as-deposited, vacuum-annealed and O₂-annealed LCMO films on (001) STO is presented in Fig. 7.6. In addition, the magnetization data for the as-deposited LCMO film on (001) SLAO substrate are also included to demonstrate the relative importance of O stoichiometry and epitaxial strain. It is clear that vacuum annealing causes a reduction of the magnetic moment as well as the Curie temperature whereas O₂ annealing has an opposite consequence. The magnetization value measured after the O₂ annealing is distinctly larger than the one measured for the as-deposited specimen, suggesting that the LCMO films contain a certain amount of O vacancies even in the as-deposited state. Moreover, it is noted that the largest magnetic moment that can be achieved by O₂ annealing at temperatures as high as 1223 K is far surpassed by the as-deposited film on SLAO substrate. The compressive epitaxial strain imposed by SLAO can have two consequences. First, the formation of the charge ordered antiferromagnetic phase can be hindered by the distortion caused by the in-plane contraction in the LCMO film. Second, the compressive epitaxial strain can stabilize more O anions in the lattice, which in turn can increase the relative amount of Mn⁴⁺ ions. This view is also supported by the results obtained by surface-sensitive and element-specific AR-XPS measurements presented and discussed in Chapters 4 and 5, respectively.

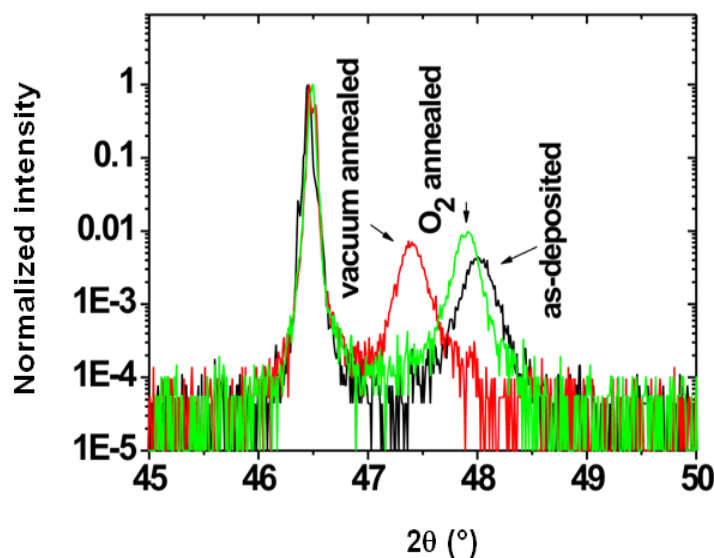


Fig. 7.5: The 040 reflection of the LCMO film deposited on (001) STO in as-deposited condition, after vacuum annealing at 773 K for 1 h and after O₂ annealing at 1223 K for 1 h.

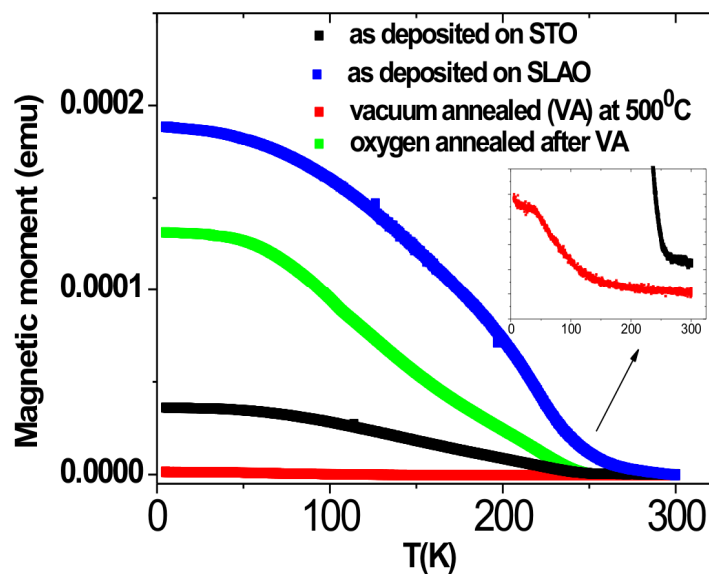


Fig. 7.6: The magnetic moment as a function of temperature for the LCMO film deposited on (001) STO in the as-deposited condition, after vacuum annealing at 773 K for 1 h and after O₂ annealing at 1223 K for 1 h. The data measured for the as-deposited LCMO film on (001) SLAO substrate are also included.

It can be concluded that there is a clear correlation between epitaxial strain, lattice distortion, oxygen stoichiometry and the electronic and magnetic properties of the LCMO films. In addition, this study suggests that the strain state of the film and its O stoichiometry may be interrelated. However, it is noted that the other mechanisms proposed to govern the electronic and magnetic properties of manganites such as charge, orbital and spin ordering can not be excluded for a complete interpretation of the film properties. These processes are regarded not to be independent of the effects related to strain state and O stoichiometry but somehow coupled together.

From the application point of view, the present study shows that it is possible to alter the electronic and magnetic properties by using different substrate materials and varying the thickness and the O stoichiometry of the LCMO films to provide materials for several purposes in microelectronic devices.

Chapter 8

Zusammenfassung

In den letzten Jahren erzielten dotierte Manganate, die in der Perowskitstruktur kristallisieren, eine bedeutende Aufmerksamkeit, die auf ihrem Entwicklungspotential als Speichermedien oder in elektronischen Schreib- und Leseköpfen beruhen. Eine der charakteristischen Eigenschaften dieser Materialklasse ist der kolossale Magnetwiderstand, d.h. die drastische Änderung des elektrischen Widerstands bei angelegtem Magnetfeld, der von einigen % bis zu 10^5 reichen kann. Darüberhinaus werden z. Zt. Manganate als Kathodenmaterial in oxidischen Brennstoffzellen sehr intensiv untersucht.

Manganate mit der chemischen Formel $\text{La}_{1-x}\text{Ca}_x\text{MnO}_3$ haben ein komplexes elektronisches Phasendiagramm, Dies beruht auf einem empfindlichen Gleichgewicht unterschiedlicher Ordnungsmechanismen wie z.B. Ladungs-, Spin- und Orbitalordnung. Ihm überlagert sind Gitterwechselwirkungen, die wesentlich von der Verzerrung der die Jahn-Teller Ionen Mn^{3+} umgebenden Sauerstoffoktaeder herrühren. Die untersuchten elektronischen Phasen und ihre zugehörigen Eigenschaften reagieren sehr empfindlich auf äussere Störungen z.B. erzeugt durch magnetische Felder oder epitaktische Verspannungen. Ziel dieser Arbeit ist es, phasenreine, epitaktisch gewachsene dünne Manganatschichten herzustellen, ihre physikalischen Eigenschaften zu untersuchen und die Möglichkeiten zu erforschen, die dominante elektronischen Phase (antiferromagnetischer Isolator oder ferromagnetisches Metall) mittels epitaktischer Spannungen gezielt zu manipulieren. Darüberhinaus soll die Rolle des Sauerstoffs und seines Einflusses auf die physikalischen Eigenschaften der Filme aus dem Blickwinkel der Defektchemie betrachtet werden. Als Ausgangsmaterial wird eine Dotierkonzentration an der Phasengrenze zwischen der isolierenden ladungsgeordneten antiferromagnetischen und der metallischen ferromagnetischen Phase der Keramik ($\text{La}_{0,5}\text{Ca}_{0,5}\text{MnO}_3$ - LCMO -) gewählt.

Filme unterschiedlicher Dicke wurden systematisch mittels gepulster Laserablation (PLD) hergestellt. Hierbei handelt es sich um eine der gängigsten Methoden, um komplexe Oxide als Schichten mit geringer Fehlstellendichte epitaktisch zu wachsen. Mit dieser Wachstumsmethode ist es möglich, einen stöchiometrischen Übertrag der Kationenzusammensetzung zwischen dem Ausgangsmaterial und der Oberfläche des Substrates zu erzielen. Der hierfür verwendete Excimer-Laser wird mit einem KrF-Gasgemisch bei einer Wellenlänge von 248 nm betrieben. Die Energiedichte und die

Pulsfrequenz betragen während des Prozess konstant bei 1.6 J/cm^2 bzw. bei 5Hz. Die Filme wurden bei 1073 K und einem Sauerstoffdruck von 0.4 mbar gewachsen, anschließend bei 1173 K für 30 Minuten bei 1 bar Sauerstoff getempert.

Die Filme wurden hinsichtlich ihrer strukturellen, elektrischen und magnetischen Eigenschaften durch Röntgendiffraktometrie (XRD), Rasterkraft- (AFM) und Transmissionselektronenmikroskopie (TEM), Photoelektronenspektroskopie (XPS), Raman-Spektroskopie, Widerstands- und Magnetisierungsmessungen untersucht.

8.1 Der Einfluss der epitaktischen Verspannungen

Die Kristallstruktur und Gitterkonstante des Substratmaterials sind wesentliche Parameter, die sowohl die Mikrostruktur als auch die daraus resultierenden physikalischen und chemischen Eigenschaften des Films bestimmen. Um epitaktische gewachsene Filme mit einer geringen Anzahl an Defekten in der Gitterstruktur herzustellen, ist es von notwendig die Differenz zwischen den Gitterkonstanten in den Ebenen von Substrat und Film so gering wie möglich zu halten wobei auch die thermische Ausdehnungskoeffizienten möglichst gleich sein sollten. Darüber hinaus ist wesentlich, dass das Substratmaterial unter Wachstums- und Raumtemperatur chemisch und mechanisch stabil bleibt. Neben diesen Grundvoraussetzungen kann das Substrat als ein funktionelles Werkzeug für die Modifikation der Filmeigenschaften durch Gitterverspannungen eingesetzt werden. In dieser Arbeit wurden SrTiO_3 (STO) mit (001)- und (111)-Orientierung sowie auf SrLaGaO_4 (SLGO) und SrLaAlO_4 (SLAO) mit (001)-Orientierung als Substrate verwendet, um den Einfluss der epitaktischen Verspannungen auf das elektrische und magnetische Verhalten der LCMO-Filme zu untersuchen. Die ersten drei genannten Substrate implizieren eine Zugspannung wohingegen der Gitterparameter von SLAO kleiner ist als der von LCMO und deshalb eine Druckspannung aufbaut. Der Einsatz verschiedener Schichtdicken eröffnet die Möglichkeit, den Einfluss der teilweisen Relaxation der Verspannungen näher zu untersuchen.

Die Röntgenuntersuchungen zeigen, dass alle Proben einphasig sind und eine orthorhombische Kristallstruktur haben. Bezüglich der {121}-Polfiguren zeigen die Filme gewachsen auf STO (001), SLAO und SLGO eine 4-zählige Symmetrie, wohingegen die Filme gewachsen auf STO (111) eine 3 zählige Symmetrie zeigen (siehe Kapitel 4).

Abbildungen 8.1 zeigt, dass der Widerstand im Temperaturbereich zwischen 300 und 4 K bei fallender Temperatur bei den Filmen auf STO (001) ansteigt. Dazu kommt, dass die Werte für die Magnetisierung sehr gering sind (siehe dazu Kapitel 4). Die Abbildungen 8.2 und 8.3, zeigen, dass bei Verwendung von SLAO (001) und STO (111) als Substrat sich ein

metallisches Verhalten einstellt. Eine mögliche Erklärung könnte wie folgt aussehen: Die epitaktische Druckspannung, die durch die Verwendung durch SLAO (001) induziert wird, verursacht eine Verkleinerung der Gitterparameter in der a - und c -Achse (bspw. in der Ebene) und eine damit zusammenhängende Vergrößerung der Parameter in b -Richtung (aus der Ebene). Eine solche Änderung in den Gitterparametern der Einheitszelle steht exakt im Gegensatz zu der, die sich durch Phasenumwandlung von der ferromagnetischen zur ladungsgeordneten anti-ferromagnetischen Phase einstellt. Die Verspannung, die durch das SLAO (001) Substrat auf das LCMO-Kristallgitter wirkt, könnte auch als zusätzliche Antriebskraft für das Entstehen der ferromagnetischen Phase wirken und so das Entstehen der ladungsgeordneten antiferromagnetischen Phase verhindern. STO (111) generiert den gleichen Effekt, da hier drei Ecken der LCMO-Einheitszelle an das Substrat gebunden sind. Diese wiederum erzeugen eine Zugspannung im Bezug zur LCMO-Einheitszelle, welche ebenso eine Entstehung der antiferromagnetisch isolierenden Phase verhindert (siehe Kapitel 4 und 5). Allerdings führt die durch STO (001) induzierte Zugspannung zu einem gegenteiligen Effekt, der das Wachstum der isolierenden gegenüber der metallischen Phase bevorzugt. Eine schematische Darstellung soll dies in Abbildung 8.4 verdeutlichen. Der Volumanteil der metallischen Phase (blau dargestellt) in einem auf STO (001) gewachsenen Film nimmt beim Abkühlen ab, wohingegen der Volumanteil der metallischen Phase in einem auf SLAO (001) und STO (111) gewachsenen Film, sich auf Kosten der isolierenden Phase (gelb dargestellt) vergrößert. Eine Verbindung zwischen den metallischen Regionen entsteht bei einer bestimmten Temperatur, bezeichnet als T_{MI} , womit sich die Probe im Gesamten wie ein Metall verhält.

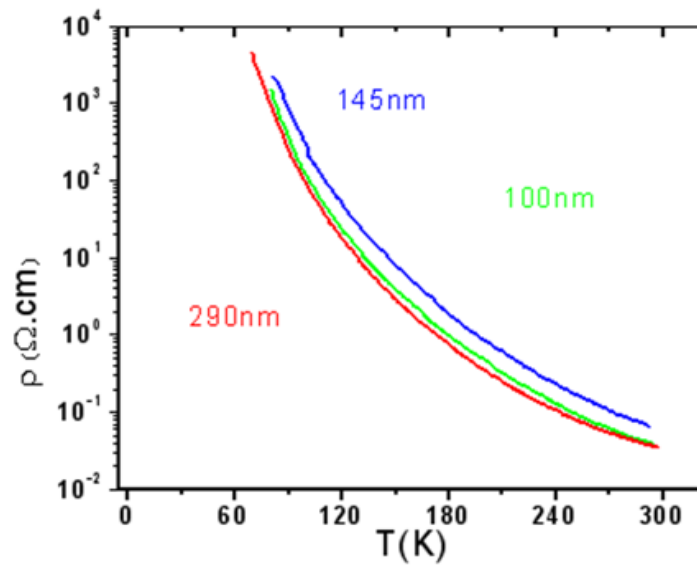


Abb. 8.1: Spezifischer Widerstand als Funktion der Temperatur bei LCMO-Filmen gewachsen auf STO (001).

Die auf STO (111) und SLAO (001) gewachsenen Filme haben eine geringe Anzahl an Kristallbaufehlern bei Raumtemperatur. Dies spiegelt sich in den Röntgen-, Raman-, Widerstandsmessungen wider (siehe Kapitel 4). Durch verringerte Störungen ergeben sich reduzierte Streuprozesse der Leitungselektronen, weshalb eine höhere Leitfähigkeit und damit verknüpft auch ein höheres magnetisches Moment auf Grund des Doppel-Austausch-Mechanismus einstellt.

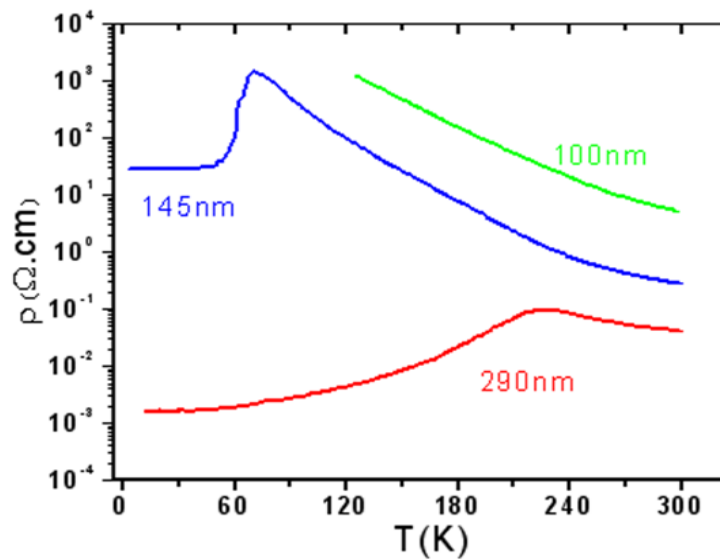


Abb. 8.2: Spezifischer Widerstand als Funktion der Temperatur bei LCMO-Filmen gewachsen auf STO (111)

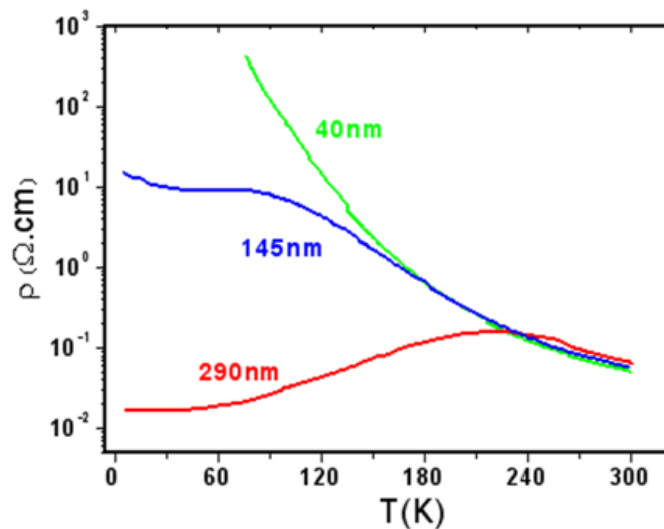


Abb. 8.3: Spezifischer Widerstand als Funktion der Temperatur bei LCMO-Filmen gewachsen auf SLAO (001).

Diese Ergebnisse unterstreichen die Tatsache, dass es möglich ist, in einer weiten Bandbreite Phasen zu stabilisieren, indem man das Substrat als Stellschraube zur Optimierung der Schichteigenschaften verwendet. Die elektrischen und magnetischen Eigenschaften hängen stark von der Schichtdicke ab, da die epitaktischen Verspannungen, hervorgerufen

durch Gitterfehlpassungen an das Substrat, bei den relativ dicken Filmen abnehmen. Vergleicht man Abbildung 8.1 und 8.2 so zeigt es sich, dass nicht nur die epitaktischen Spannungen, sondern auch die Orientierung zur LCMO-Einheitszelle kritisch für die elektrischen und magnetischen Eigenschaften sind (beide Substrate, STO (001) und STO (111), induzieren epitaktische Spannung in der Ebene; siehe Kapitel 2 und 4).

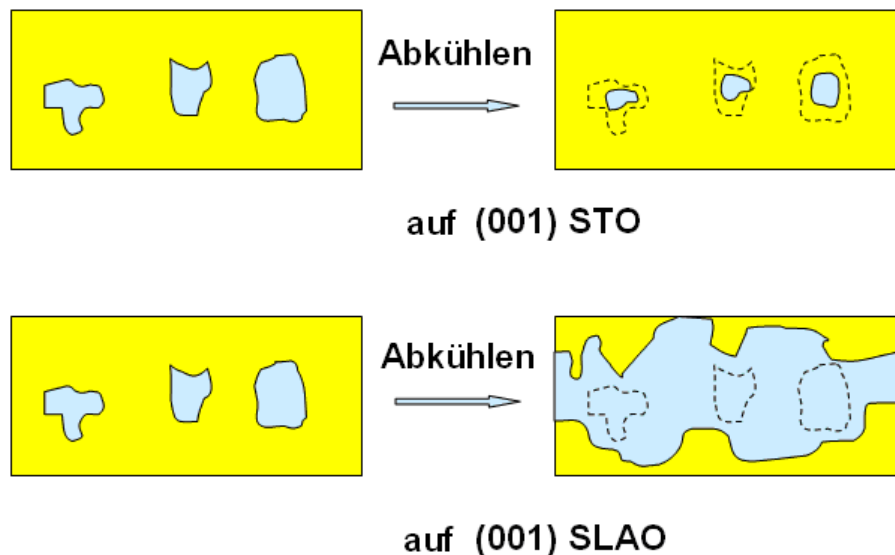


Fig. 8.4: Schematische Darstellung der verschiedenen elektronischen Phasen in den LCMO-Filmen auf STO (001) und SLAO (001). Die blaue und gelbe Farbe kennzeichnen die metallischen respektive die isolierenden Phasen.

8.2 Der Einfluss der Sauerstoffstöchiometrie

Um den Einfluss der Sauerstoffstöchiometrie auf die strukturellen, elektronischen und magnetischen Eigenschaften der LCMO-Filme zu verstehen, wurden diese nach dem Wachstum in Vakuum beziehungsweise bei wohldefiniertem Druck im konstanten O_2 -Fluss getempert.

Röntgendaten von unbehandelten, in Vakuum geheizten und nachträglich mit Sauerstoff behandelten Filme werden in Abbildung 8.5 dargestellt. Es zeigt sich, dass die 040-Reflexe des Films zu kleineren 2θ -Werten hin verschoben sind, was die Vergrößerung der senkrecht zur Filmebene stehenden Gitterparameter während des Vakuumheizens, widerspiegelt. Die Vergrößerung die Gitterparameter könnte möglicherweise durch eine erhöhte Sauerstoffleerstellenkonzentration erreicht werden, die zur Erhaltung der

Ladungsneutralität mit der Umwandlung zweier Mn^{4+} zu Mn^{3+} einhergeht. Die unterschiedlichen Ionenradien von Mn^{4+} und Mn^{3+} spielen hierbei eine wichtige Rolle. Die Position der 040-Reflexe kehrt nahezu auf ihren Ausgangspunkt der unbehandelten Probe zurück, wenn man die Probe anschließend mit O_2 -Fluss geheizt wurde.

In Abbildung 8.6 werden die Änderungen von Magnetisierung gegen Temperatur zwischen unbehandelten, in Vakuum geheizten und O_2 -getemperte LCMO-Filmen auf STO (001) dargestellt. Zusätzlich sind die Ergebnisse der LCMO-Filme auf SLAO, um die Wichtigkeit der Sauerstoffstöchiometrie und der epitaktische Spannungen zu verdeutlichen. Es ist klar, dass das Heizen der Probe im Vakuum eine Verminderung des magnetischen Moments sowie der Curie-Temperatur zur Folge hat, wobei ein O_2 -Tempern das Gegenteil bewirkt. Der Absolutwert der Magnetisierung gemessen, nach dem O_2 -Tempern, ist um ein bedeutendes Stück größer als bei einer unbehandelten Probe. Hierbei ist zu beachten, dass eine unbehandelte Probe eine gewisse Anzahl an Sauerstoffleerstellen enthält. Darüber hinaus wurde festgestellt, dass das größte magnetische Moment nach dem Temperprozess bei 1223 K in Sauerstoff bei Filmen, gewachsen auf SLAO, beobachtet wurde. Die Druckspannungen, die durch SLAO erzeugt werden haben zwei Konsequenzen. Erstens, die Entstehung der ladungsgeordnet antiferromagnetischen Phase kann durch Störungen verhindert werden, die durch die Kontraktion in den LCMO-Filmen erzeugt werden. Zweitens, die Druckspannungen können mehr Sauerstoff im Gitter stabilisieren, was eine Erhöhung der Mn^{4+} - Ionenkonzentration zur Folge hat. Diese Erkenntnis wird durch die Ergebnisse der oberflächen-sensitive und elementspezifische AR-XPS Messungen bestätigt und näher in Kapitel 4 und 5 erläutert.

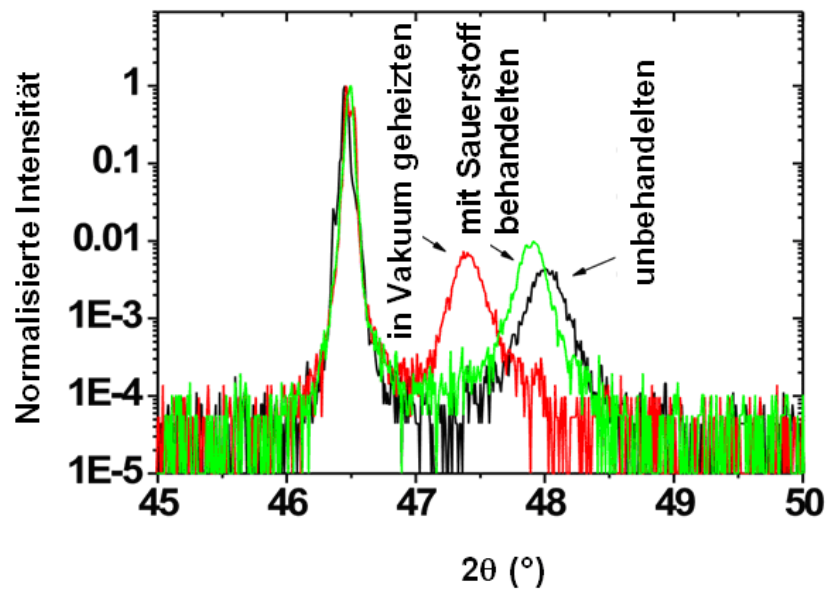


Abb. 8.5: Die 040-Reflexe von 80 nm dicken LCMO-Filmen gewachsen auf STO (001) als un behandelter Film, nach Heizen in Vakuum bei 773 K für 1 Stunde und Heizen in Sauerstoff bei 1223 K für 1 Stunde.

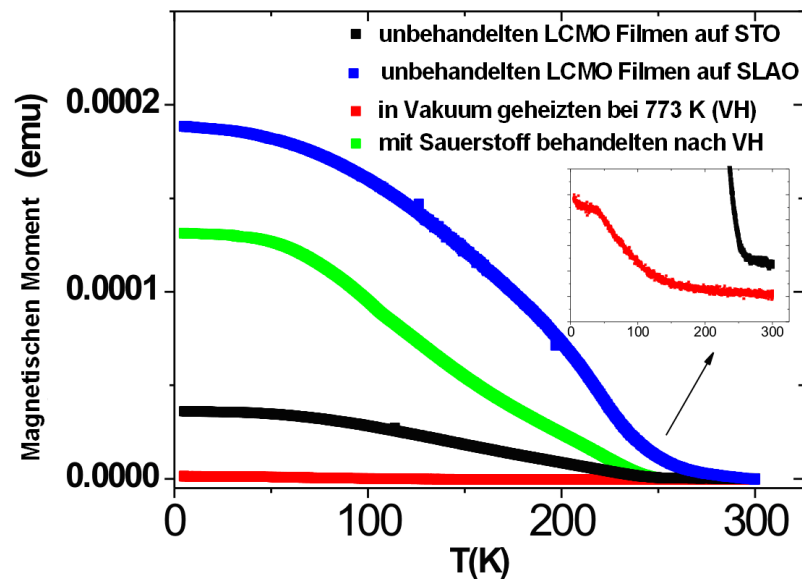


Abb. 8.6: Das magnetische Moment als Funktion der Temperatur bei auf STO (001) gewachsenen LCMO-Filmen, bei un behandelten Filmen, nach Heizen in Vakuum (773 K, 1 Stunde) und nach Heizen in Sauerstoff (1223 K, 1 Stunde). Die Messungen von auf SLAO (001) gewachsenen Filmen werden ebenfalls dargestellt.

Zusammenfassend kann gesagt werden, dass ein klarer Zusammenhang zwischen epitaktischen Spannungen, Gitterdefekten, Sauerstoffstöchiometrie und den elektrischen und magnetischen Eigenschaften der LCMO-Filmen existiert. Zusätzlich gibt diese Arbeit Anzeichen auf ein Zusammenspiel zwischen den Spannungen im Film und seiner Sauerstoffstöchiometrie. Die elektrischen und magnetischen Eigenschaften der Manganate werden wesentlich Ladungs-, Orbital- und Spinordnung bestimmt, die durch die hier untersuchten Mechanismen mittelbar oder unmittelbar beeinflusst werden.

Aus Sicht der Anwendungen, zeigt diese Arbeit, dass es möglich ist, die elektronischen und magnetischen Eigenschaften durch den Einsatz verschiedener Substratmaterialien, die Veränderung der Schichtdicke und die Sauerstoffstöchiometrie der LCMO-Filme zu variieren um Materialien für verschiedene mikroelektronische Anwendungen bereit zu stellen.

References

- [1] M. Schuisky, J. W. Elam and S. M. George, Appl. Phys. Lett. **81**, 180 (2002).
- [2] E. Llobet, X. Vilanova, J. Brezmes, R. Alcubilla, J. Calderer, J. E. Sueiras and X. Correig, Meas. Sci. Technol. **8**, 1133 (1997).
- [3] R. von Helmolt, J. Wecker, B. Holzapfel, L. Schultz and K. Samwer, Phys. Rev. Lett. **71**, 2331 (1993).
- [4] S. Jin, T. H. Tiefel, M. McCormack, R. A. Fastnacht, R. Ramesh and L. H. Chen, Science **264**, 413 (1994).
- [5] E. Dagotto, New J. Phys. **7**, 67 (2005).
- [6] S. S. P. Parkin, Annu. Rev. Mater. Sci. **25**, 357 (1995).
- [7] A. Gupta and J. Z. Sun, J. Magn. Magn. Mater. **200**, 24 (1999).
- [8] J. M. D. Coey, M. Viret and S. von Molnár, Adv. Phys. **48**, 167 (1999).
- [9] M.-H. Jo, N. D. Mathur, J. E. Evetts and M. G. Blamire, Appl. Phys. Lett. **77**, 3803 (2000).
- [10] N. Q. Minh, J. Am. Ceram. Soc. **76**, 563 (1993).
- [11] S. C. Singhal, Solid State Ionics **135**, 305 (2000).
- [12] J. Fleig, Annu. Rev. Mater. Res. **33**, 361(2003).
- [13] V. Brichzin, J. Fleig, H.-U. Habermeier, G. Cristiani and J. Maier, Solid State Ionics **152**, 499 (2002).
- [14] J. Fleig, F. S. Baumann, V. Brichzin, H.-R.Kim, J. Jamnik, G. Cristiani, H.-U. Habermeier and J. Maier, Fuel Cells **06**, 284 (2006).
- [15] J. B. Goodenough, Rep. Prog. Phys. **67**, 1915 (2004).
- [16] Y. Tokura, *Fundamental features of colossal magnetoresistive manganeseoxides* (Gordon & Breach, London, 1999).
- [17] J. A. M. van Roosmalen and E. H. P. Cordfunke, J. Solid State Chem., **93**, 212 (1991)
- [18] J. A. M. van Roosmalen, E. H. P. Cordfunke, R. B. Helmholtz and H. W. Zandbergen, J. Solid State Chem. **110**, 100 (1994).
- [19] L. Malavasi, J. Mater. Chem. **18**, 3295 (2008).
- [20] L. Malavasi, C. Ritter, M. C. Mozzati, C. Tealdi, M. S. Islam, C. B. Azzoni and G. Flor, J. Solid State Chem. **178**, 2042 (2005).
- [21] L. Malavasi, C. Ritter, M. C. Mozzati, C. Tealdi, C. B. Azzoni, G. Chiodelli and G. Flor, Solid State Comm. **123**, 321 (2002).
- [22] I. Walha, W. Boujelben, M. Koubaa, A. Chelkh-Rouhou and A. M. Haghiri-Gosnet,

- Phys. Stat. Sol. **201**, 1416 (2004).
- [23] F. A. Kröger and H. J. Vink, *Solid State Physics Advances in Research and Applications* (Academic, New York, 1957).
- [24] V. Goldschmidt, *Geochemistry* (Oxford University Press, London, 1958).
- [25] A. P. Ramirez, J. Phys.:Condens. Matter **9**, 8171 (1997).
- [26] C. N. R. Rao, A. K. Cheetham, R. Mahesh, Chem. Matter **8**, 2421 (1996).
- [27] M. B. Salamon and M. Jaime, Rev. Mod. Phys. **73**, 583 (2001).
- [28] S. W. Cheong and H. Y. Hwang, *Ferromagnetism vs charge orbital ordering in mixed valent manganites in colossal magnetoresistance oxides* (Gordon and Breach, London 1999).
- [29] T. Hotta, S. Yunoki, M. Mayr and E. Dagotto Phys. Rev. **60**, R15009 (1999).
- [30] G. H. Jonker and J. H. van Santen, Physica **16**, 337 (1950).
- [31] J. H. van Santen and G. H. Jonker, Physica **16**, 599 (1950).
- [32] C. Zener, Phys. Rev. **82**, 403 (1951).
- [33] P. W. Anderson and H. Hasegawa Phys. Rev. **100**, 675 (1955).
- [34] J. B. Goodenough, Phys. Rev. **100**, 564 (1955).
- [35] M. Atanasov and S. Angelov, Chem. Phys. **150**, 383 (1991).
- [36] Y. Tokura and Y. Tomioka, J. Magn. Magn. Mater. **200**, 1 (1999).
- [37] H. A. Jahn and E. Teller, Proc. R. Soc. London Ser. A **161**, 220 (1937).
- [38] C. N. R. Rao and B. Raveau, *Colossal Magnetoresistance, Charge Ordering and Related Properties of Manganese Oxides* (World Scientific, Singapore, 1998).
- [39] M. Uehara, S. Mori, C. H. Chen and S.-W. Cheong, Nature **399**, 560 (1999).
- [40] Ch. Renner, G. Aeppli, B.-G. Kim, Yeong-Ah Soh and S.-W. Cheong, Nature **416**, 518 (2002).
- [41] J. C. Loudon, N. D. Mathur and P. A. Midgley, Nature **420**, 797 (2002).
- [42] B. Martinez, V. Laukhin, J. Fontcuberta, L. Pinsard and A. Revcolevschi Phys. Rev. B **66**, 054436 (2002).
- [43] P. Postorino, A. Congeduti, P. Dore, A. Sacchetti, F. Gorelli, L. Ulivi, A. Kumar and D. D. Sarma Phys. Rev. Lett. **91**, 175501 (1991).
- [44] F. S. Razavi, G. V. Sudhakar Rao, H. Jalili and H.-U. Habermeier, Appl. Phys. Lett. **88**, 174103 (2006).
- [45] T. Roch, S. Yaghoubzadeh, F. S. Razavi, B. Leibold, R. Praus and H.-U Habermeier, Appl. Phys. A **67**, 723 (1998).
- [46] V. Kiryukhin, D. Casa, J. P. Hill, B. Keimer, A. Vigliante, Y. Tomioka and Y. Tokura

- Nature **386**, 813 (1997).
- [47] D. Casa, B. Keimer, M. Zimmermann, J. P. Hill, H.-U. Habermeier and F. S. Razavi, Phys. Rev. B **64**, 100404(R) (2001).
- [48] P. X. Zhang, J. B. Wang, G. Y. Zhang, H.-U. Habermeier and W. K. Lee, Physica C **364**, 656 (2001).
- [49] M. Fiebig, K. Miyano, Y. Tomioka and Y. Tokura, Science **280**, 1925 (1998).
- [50] A. Asamitsu, Y. Tomioka, H. Kuwahara and Y. Tokura, Nature **388**, 50 (1997).
- [51] Y. Tokura, Y. Tomioka, H. Kuwahara, A. Asamitsu, Y. Moritomo and M. Kasai, J. Appl. Phys. **79**, 5288 (1996).
- [52] H. Yamamoto, T. Murakami, J. Sakai and S. Imai, Solid State Comm. **142**, 28 (2007).
- [53] Y. Tokura, Y. Tomioka, H. Kuwahara, A. Asamitsu, Y. Moritomo and M. Kasai, Physica C **263**, 544 (1996).
- [54] J. Zhang, H. Tanaka, T. Kanki, J. H. Choi and T. Kawai, Phys. Rev. B **64**, 184404 (2001).
- [55] H.-U Habermeier, Physica B **321**, 9 (2002).
- [56] H.-U Habermeier, F. S. Razavi, R. Praus and G. M. Gross, Physica C **341**, 777 (2000).
- [57] H. S. Wang, E. Wertz, Y. F. Hu, Q. Li and D. G. Schlom, J. Appl. Phys. **87**, 7409 (2000).
- [58] L. Ranno, A. Llobet, M. B. Hunt and J. Pierre, Appl. Surf. Sci. **138-139**, 228 (1999).
- [59] N. C. Yeh, R. P. Vasquez, D. A. Beam, C. C. Fu, J. Huynh and G. Beach, J. Phys.: Condens. Matter **9**, 3713 (1997).
- [60] V. Trtik, F. Sanchez, M. Varela, M. Bibes, B. Martinez and J. Fontcuberta, J. Magn. Magn. Mater. **203**, 256 (1999).
- [61] O. Yu Gorbenko, I. E. Graboy, A. R. Kaul and H. W. Zandbergen, J. Magn. Magn. Mater. **211**, 97 (2000).
- [62] M. Ziese, H. C. Semmelhack, K. H. Han, S. P. Sena and H. J. Blythe, J. Appl. Phys. **91**, 9930 (2002).
- [63] T. Walter, K. Dörr, K. H. Müller, D. Eckert, K. Nenkov, M. Hecker, M. Lehmann and L. Schultz, J. Magn. Magn. Mater. **222**, 175 (2000).
- [64] J. Z. Sun, D. W. Abraham, R. A. Rao and C. B. Eom, Appl. Phys. Lett. **74**, 3017 (1999).
- [65] M. Sahana, T. Walter, K. Dörr, K.-H. Müller, D. Eckert and K. Brand, J. Appl. Phys. **89**, 6834 (2001).
- [66] R. B. Praus, B. Leibold, G. M. Gross and H.-U. Habermeier, Appl. Sur. Sci. **138-139**,

- 40 (1999).
- [67] M. Bibes, Ll. Balcells, S. Valencia, J. Fontcuberta, M. Wojcik, E. Jedryka and S. Nadolski, *Phys. Rev. Lett.* **87**, 067210 (2001).
- [68] J. Aarts, S. Freisem, R. Hendrikx and H. W. Zandbergen, *Appl. Phys. Lett.* **72**, 2975 (1998).
- [69] J. R. Sun, C. F. Yeung, K. Zhao, L. Z. Zhou, C. H. Leung, H. K. Wong and B. G. Shen, *Appl. Phys. Lett.* **76**, 1164 (2000).
- [70] E. Beyreuther, S. Grafström, L. M. Eng, C. Thiele and K. Dörr, *Phys. Rev. B* **73**, 155425 (2006).
- [71] B. Vengalis, V. Lissauskas, V. Pyragas, K. Sliuziene, A. Oginskis, A. Cesnys, J. Santiso and A. Figueras, *J. Phys. IV* **11**, 209 (2001).
- [72] L. Malavasi, I. Alessandri, M. C. Mozzati, P. Ghigna, G. Chiodelli, C. B. Azzoni and G. Flor, *Phys. Chem. Chem. Phys.* **5**, 2274 (2003).
- [73] H. Vincent, M. Audier, S. Pignard, G. Dezanneau and J. P. Senateur, *J. Magn. Magn. Magn.* **226-230**, 788 (2001).
- [74] Srinivas V. Pietambaram, D. Kumar, Rajiv K. Singh and C. B. Lee, *MRS Sympo. Proceed.* **617**, J 3.14.1 (2000).
- [75] S. W. Jin, X. Y. Zhou, W. B. Wu, C. F. Zhu, H. M. Weng, H. Y. Wang, X. F. Zhang, B. Ye and R. D. Han, *J. Phys. D: Appl. Phys.* **37**, 1841 (2004).
- [76] J. R. Sun, H. W. Yeung, H. K. Wong, T. Zhu and B. G. Shen, *Eur. Phys. J. B* **35**, 481 (2003).
- [77] A. Tebano, G. Balestrino, N. G. Boggio, C. Aruta, B. Davidson and P. G. Medaglia *Eur. Phys. J. B* **51**, 337 (2006).
- [78] M. Sirenaa, N. Haberkorna, M. Granadaa, L. B. Sterena and J. Guimpel, *J. Magn. Magn. Mat.* **1171-1173**, 272276 (2004).
- [79] M. Pattabiraman, P. Murugaraj, G. Rangarajan, V. Prasad, S. V. Subramanyam, V. S. Sastry, S.-M. Koo and K. V. Rao, *Pramana-J. Phys.* **55**, 455 (2000).
- [80] C.-J. Liu, M.-S. Huang and C.-S. Sheu, *Chin. J. Phys.* **38**, 360 (2000).
- [81] N. Malde, P. S. I. P. N. De Silva, A. K. M. Akther Hossain, L. F. Cohen, K. A. Thomas, J. L. MacManus-Driscoll, N. D. Mathur and M. G. Blamire, *Solid State Comm.* **105**, 643 (1998).
- [82] W. Prellier, M. Rajeswari, T. Venkatesan and R. L. Greene, *Appl. Phys. Lett.* **75**, 1446 (1999).
- [83] J. F. Ready, *Appl. Phys. Lett.* **3**, 11 (1963).

-
- [84] R. M. White, *J. Appl. Phys.* **43**, 3559 (1963).
- [85] H. M. Smith and A. F. Turner, *Appl. Opt.* **4**, 147 (1965).
- [86] D. Dijkkamp, T. Venkatesan, X. D. Wu, S. A. Shaheen, N. Jisrawi, Y. H. Minlee, W. L. McLean and M. Croft, *Appl. Phys. Lett.* **51**, 619 (1987).
- [87] S. M. Metev and V. P. Veiko, *Laser Assisted Microtechnology* (Springer, Berlin, Heidelberg, 1994).
- [88] J. F. M Cillessen, *Pulsed Laser Deposition of Oxide Film* (Philips electronics N.V., 1996).
- [89] D. B. Chrisey and G. K. Hubler, *Pulsed Laser Deposition of Thin Film* (John Wiley and Sons, Newyork, 1994).
- [90] G. J. H. M. Rijnders, G. Koster, D. H. A. Blank and H. Rogalla, *Mater. Sci. and Eng. B* **56**, 223 (1998).
- [91] M. Ohring, *The Materials Science of Thin Films* (Academic Press, New Jersey, 2002).
- [92] J. A. Venables, G. D. T. Spiller and M. Hanbucken, *Rep. Prog. Phys.* **47**, 399 (1984).
- [93] E. Bauer and H. Poppa, *Thin Solid Films* **12**, 167 (1972).
- [94] M. Berkowski, *J. Alloys and Comp.* **251**, 1 (1997).
- [95] J. Hulton and R. J. Nelmes, *J. Phys. C: Solid State Phys.* **14**, 1713 (1981).
- [96] R. D. Shannon, R. A. Oswald, J. B. Parise, B. H. T. Chai, P. Byszewski, A. Pajaczkowska and R. Sobolewski, *J. Solid State Chem.* **98**, 90 (1992).
- [97] J. F. Britten, H. A. Dabkowska, A. B. Dabkowski, J. E. Greedan, J. L. Campbell and W. J. Teesdale, *Acta Crystallogr. C* **51**, 1975 (1995).
- [98] H. Bubert and H. Jenett, *Surface and Thin Film Analysis* (Wiley-VCH, Weinheim, 2002).
- [99] U. Wedzel, J. Ligot, P. Lamparter, A. C. Vermeulen and E. J. Mittemeijer, *J. Appl. Cryst.* **38**, 1 (2005).
- [100] B. D. Cullity and S. R. Stock, *Elements of X-ray Diffraction* (Prentice Hall, New Jersey, 2001).
- [101] A. Strecker, U. Baeder, M. Kelsch, U. Salzberger, M. Sycha, M. Gao, G. Richter and K. V. Benthem, *Z. Metallkd.* **94**, 3 (2003).
- [102] M. S. Vinodh and L. P. H. Jeurgens, *Surf. Interf. Anal.* **36**, 1629 (2004).
- [103] A. Antonakos, E. Liarokapis, G. H. Aydogdu and H.-U. Habermeier, *Mater. Sci. and Eng. B* **144**, 83 (2007).
- [104] A. Antonakos, D. Lampakis, E. Liarokapis, M. Filippi, W. Prellier, G. H. Aydogdu and H.-U. Habermeier, *J. Phys.: Condens. Matter* **20**, 485202 (2008).

-
- [105] A. Antonakos, M. Filippi, G. H. Aydogdu, W. Prellier, H.-U. Habermeier and E. Liarokapis, *Phys. Stat. Sol. B* **246**, 635 (2009).
- [106] P. Carra, B. T. Thole, M. A. Itarelli and X. Wang, *Phys. Rev. Lett.* **70**, 694 (1993).
- [107] B. T. Thole, P. Carra, F. Sette and G. van der Laan, *Phys. Rev. Lett.* **68**, 1943 (1992).
- [108] M. Sikora, Cz. Kapusta, D. Zając, W. Tokarz, C. J. Oates, M. Borowiec, D. Rybicki, E. Goering, P. Fischer, G. Schütz, J. M. DeTeresa and M. R. Ibarra, *J. Magn. Magn. Mater.* **272-276**, 2148 (2004).
- [109] F. Weigand, S. Gold, A. Schmid, J. Geissier and E. Goering, *Appl. Phys. Lett.* **81**, 2035 (2002).
- [110] E. Goering, *XMCD Spectroscopy and Reflectometry*, Lectures for Magnetism in Nanostructures and Novel Materials IMPRS, Stuttgart (2008).
- [111] J. W. Olesik, *Anal. Chem.* **63**, 12 (1991)
- [112] W. I. F. David, K. Shankland, J. van de Streek, E. Pidcock, W. D. S. Motherwell and J. C. Cole, *J. Appl. Cryst.* **39**, 910 (2006).
- [113] P. M. Woodward, T. Vogt, D. E. Cox, A. Arulraj, C. N. R. Rao, P. Karen and A. K. Cheetham, *Chem. Mater.* **10**, 3652 (1998).
- [114] J. C. Ludon, N. D. Mathur and P. A. Midgley, *Nature* **420**, 797 (2002).
- [115] M. Ziese, H. C. Semmelhack and K. H. Han, *Physical Rev. B* **68**, 134444 (2003).
- [116] Y. P. Lee, S. Y. Park, Y. H. Hyun, J. B. Kim, V. G. Prokhorov, V. A. Komashko and V. L. Svetchnikov, *Phys. Rev. B* **73**, 224413 (2006).
- [117] P. A. Joy, P. S. Anil Kumar and S. K. Date, *J. Phys. Condens. Matter* **10**, 11049 (1998).
- [118] C. S. Xiong, Y. H. Xiong, W. Yi, G. N. Meng, Z. C. Xia, X. G. Li and S. L. Yuan, *J. Phys.: Condens. Matter* **14**, 4309 (2002).
- [119] R. Gupta, A. K. Sood, R. Mahesh and C. N. R. Rao, *Phys. Rev. B* **54**, 14899 (1996).
- [120] H. L. Liu, S. Yoon, S. L. Cooper, S.-W. Cheong, P. D. Han and D. A. Payne, *Phys. Rev. B* **58**, 10115 (1998).
- [121] S. Yoon, H. L. Liu, G. Schollerer, S. L. Cooper, P. D. Han, D. A. Payne, S.-W. Cheong and Z. Fisk, *Phys. Rev. B* **58**, 2795 (1998).
- [122] L. Martin-Carron, A. de Andres, M. J. Martinez-Lope, M. T. Casais and J. A. Alonso, *Phys. Rev. B* **66**, 174303 (2002).
- [123] M. V. Abrashev, J. Bäckström, L. Börjesson, M. Pissas, N. Kolev and M. N. Iliev, *Phys. Rev. B* **64**, 144429 (2001).
- [124] A. Tatsi, E. L. Papadopoulou, D. Lampakis, W. Prellier and B. Mercey, *Phys. Rev. B*

- 68**, 024432 (2003).
- [125] M. N. Iliev and M. V. Abrashev, *J. Raman Spectrosc.* **32**, 805 (2001).
- [126] Y. M. Xiong, T. Chen, G. Y. Wang, X. H. Chen, X. Chen and C. L. Chen, *Phys. Rev. B* **70**, 94407 (2004).
- [127] P. G. Radaelli, D. E. Cox, M. Marezio and S. W. Cheong, *Phys. Rev. B* **55**, 3015 (1997).
- [128] Q. Huang, J. W. Lynn, R. W. Erwin, A. Santoro, D. C. Dender, V. N. Smolyaninova, K. Ghosh and R. L. Greene, *Phys. Rev. B* **61**, 8895 (2000).
- [129] A. Biswas, M. Rajeswari, R. C. Srivastava, T. Venkatesan, R. L. Greene, Q. Lu, A. L. de Lozanne and A. J. Millis, *Phys. Rev. B* **63**, 184424 (2001).
- [130] M. N. Iliev, M. V. Abrashev, H.-G. Lee, V. N. Popov, Y. Y. Sun, C. Thomsen, R. L. Meng and C. W. Chu, *Phys. Rev. B* **57**, 2872 (1998).
- [131] G. H. Aydogdu, Y. Kuru and H.-U. Habermeier, *Mater. Sci. and Eng. B* **144**, 123 (2007).
- [132] G. H. Aydogdu, Y. Kuru and H.-U. Habermeier, *J. Cryst. Growth* **310**, 4521 (2008).
- [133] O. I. Lebedev, G. Van Tendeloo, S. Amelinckx, B. Leibold and H.-U. Habermeier, *Phys. Rev. B* **58**, 8065 (1998).
- [134] J. O' Donnell, M. S. Rzechowski, J. N. Eckstein and I. Bozovic, *App. Phys. Lett.* **72**, 1175 (1998).
- [135] V. R Galakhov, M. Demeter, S. Bartkowski, M. Neumann, N. A Ovechkina, E. Z. Kurmaev, N. I. Lobachevskaya, Ya. M. Mukovskii, J. Mitchell and D. L. Ederer, *Phys. Rev. B* **65**, 113102 (2002).
- [136] www.ccdc.cam.ac.uk/free_services/encifer/
- [137] N. F. Mott and E. A. Davis, *Electronic Processes in Noncrystalline Materials* (Clarendon, Oxford, 1979).
- [138] A. J. Millis, R. Mueller and B. I. Shraiman, *Phys. Rev. B* **54**, 5405 (1996).
- [139] C. Meneghini, C. Castellano, S. Mobilio, A. Kumar, S. Ray and D. D. Sarma, *J. Phys.: Condens. Matter* **14**, 1967 (2002).
- [140] B. I. Shklovskii and A. L. Efros, *Electronic Properties of Doped Semiconductors* (Springer-Verlag, Berlin, 1984).
- [141] P. K. Siwach, H. K. Singh and O. N. Srivastava, *J. Phys.: Condens. Matter* **18**, 9783 (2006).
- [142] I. Lubomirsky, *Phys. Chem. Chem. Phys.* **9**, 3701 (2007).
- [143] M. Greenberg, E. Wachtel, I. Lubomirsky, J. Fleig and J. Maier, *Adv. Funct. Mater.*

16, 48 (2006).

[144] I. Lubomirsky, *Solid State Ionics* **177**, 1639 (2206)

Acknowledgements

This work was performed in Max Planck Institute for Solid State Research and supported financially by Max Planck Society and NMP4-CT-2005-517039 controlling mesoscopic phase separation (COMEPHS) project.

Firstly, I am indebted to my supervisor, Dr. Hanns-Ulrich Habermeier for accepting me as a Ph. D. student to his department. The regular scientific discussions with him, his ideas, guidance and encouragement significantly contributed to the successful completion of this study.

I would like to thank Prof. Dr. Joachim Maier for acting as the first referee of the thesis, Prof. Dr. Joachim Bill for acting as the second referee of the thesis and Prof. Dr. Helmut Bertagnolli for being the head of my examination committee.

I am grateful to Anastasios Antonakos and Prof. Dr. Efthymios Liarokapis for Raman spectroscopy measurements and their interpretation, Thomas Tietze and PD Dr. Eberhard Goering for various XMCD measurements, Dr. Ir. Lars P.H. Jeurgens for angle-resolved XPS measurements, PD Dr. Peter A. van Aken and Dr. Jaysen Nelayah for TEM measurements.

My special thanks to Benjamin Stuhlhofer for assistance during preparing the German version of the summary and to all colleagues in Technology service group for their assistance during my research.

I am forever grateful to my parents Ekrem-Güner Aydoğdu, Hamide Taşan, Nilgün Aydoğdu-Armağan Barut, my husband Yener Kuru and his parents İsmet-Nimet-Nur Kuru for their support throughout my life as well as all members of Turkish Mafia who made my stay at Stuttgart pleasant and enjoyable.

Curriculum Vitae

Personal

Name	Gülgün Hamide Aydoğdu Kuru
Date and Place of Birth	27.01.1979, Ankara, Turkey
Marital Status	Married
Nationality	Turkish

Schooling

1992 – 1996	Batıkent High School, Ankara, Turkey.
-------------	--

Higher education

1996 – 2001	B. Sc. (Metallurgical and Materials Engineering) Middle East Technical University, Ankara, Turkey.
2002 – 2004	M. Sc. (Metallurgical and Materials Engineering) Middle East Technical University, Ankara, Turkey.

Dissertation

2005 – 2009	Ph.D. at the Max Planck Institute for Solid State Research and University of Stuttgart
-------------	---

List of Publications Relevant to This Study

Effect of vacuum and O₂ annealing treatments on structural and magnetic properties of La_{0.5}Ca_{0.5}MnO₃ thin films

G. H. Aydogdu, Y. Kuru and H.-U. Habermeier, Journal of Superconductivity and Novel Magnetism

Half Ca-doped LaMnO₃ films on (001) SLAO and STO substrate studied by magnetization and transport measurements

G. H. Aydogdu and H.-U. Habermeier, Journal of Magnetism and Magnetic Materials

Tuning the magnetic and electronic properties of manganite thin films by epitaxial strain.

G. H. Aydogdu, Y. Kuru and H.-U. Habermeier, Advances in Nanoscale Magnetism, Springer Proceedings in Physics

Novel electronic and magnetic properties of La_{0.5}Ca_{0.5}MnO₃ films deposited on (111) SrTiO₃ substrates

G. H. Aydogdu, Y. Kuru and H.-U. Habermeier, Journal of Crystal Growth

Tuning of the charge ordered state in the manganite thin films by internal or external strains

A. Antonakos, M. Filippi, G. H. Aydogdu, W. Prellier, H.-U. Habermeier and E. Liarokapis, Physica Status Solidi

Thickness dependence of substrate-induced strain in La_{0.9}Ca_{0.1}MnO₃ thin films

S. Uthayakumar, G. H. Aydogdu and H.-U. Habermeier, Journal of Crystal Growth

Structural and electronic properties of LCMO films deposited on differently oriented STO substrates

G. H. Aydogdu, Y. Kuru and H.-U. Habermeier, Materials Science and Engineering B

Strain effects on La_{0.5}Ca_{0.5}MnO₃ thin films

A. Antonakos, E. Liarokapis, G. H. Aydogdu and H.-U. Habermeier, Materials Science and Engineering B

Phase separation in manganite thin films

A. Antonakos, D. Lampakis, E. Liarokapis, M. Filippi, W. Prellier, G. H. Aydogdu and H.-U. Habermeier, Journal of Physics: Condensed Matter